Metal-Insulator-Metal Diodes For Solar Energy Conversion

By

Blake J. Eliasson

B.S., Electrical Engineering, Montana State University, 1995

M.S., Electrical Engineering, University of Colorado at Boulder, 1997

A thesis submitted to the

Graduate School of the

University of Colorado in partial fulfillment

of the requirement for the degree of

Doctor of Philosophy

Department of Electrical and Computer Engineering

2001

This dissertation for the Doctor of Philosophy degree by

Blake J. Eliasson

has been approved for the

Department of

Electrical and Computer Engineering

by

____
Garret Moddel

____
Bart Van Zeghbroeck

Date________________

The final copy of this thesis has been examined by the signatories, and we find that both the content and the form meet acceptable presentation standards of scholarly work in the above mentioned discipline.

Eliasson, Blake J. (Ph.D., Electrical Engineering)

Metal-Insulator-Metal Diodes For Solar Energy Conversion

Thesis directed by Professor Garret Moddel

Metal-insulator-metal (MIM) diodes are used to rectify high frequency electromagnetic radiation coupled to them via an integrated antenna. The application of MIM diodes to solar energy conversion is investigated.

MIM diodes made from the native oxides of chromium, aluminum and niobium are experimentally fabricated. The processing of the oxide layer plays a critical role in MIM diode performance. The oxidation method, condition, substrate choice, cleanliness, oxidation time, temperature, ion incorporation, plasma processing, measurement techniques, and metals all affect the MIM diode performance. The MIM diodes are characterized under unilluminated conditions and compared to theory.

Classical and semiclassical models are used to predict the structural requirements for optimal solar energy conversion efficiency. A PSpice model is developed to characterize MIM diodes under low frequency illumination. The semiclassical theory of photon assisted tunneling is used to predict device performance at higher frequencies. The applicability and limitations of these models is detailed and conversion efficiencies are theoretically calculated for a variety of illumination conditions.

An improved diode is developed which possesses some of the characteristics required for efficient solar energy conversion. Theoretical calculations and experimental measurements of the device are presented.

Dedicated to the loving memory of my grandparents,

Ed & Mamie Eliasson

ACKNOWLEDGMENTS

There are a multitude of people I wish to acknowledge and thank for helping in various ways to make this thesis possible. I would like to thank my thesis advisor Garret Moddel for inviting me to work in his lab and help throughout the course of the project. Bruce Lanning and Brian Berland from ITN Energy Systems for financially supporting a majority of the project through a subcontract to CU. Bart Van Zeghbroeck for granting me access to his clean room facilities along with valuable discussions and feedback. The members of my thesis committee: Zoya Popovic, Leo Radzihovsky, and Frank Barnes. Skip Wichart for maintaining the lab equipment, modifying it as needed, and processing suggestions. Jeff Elam from Steve George's research group; without his atomic layer depositions the MIIM diodes would not have been possible. Kristi Kamm for her recent processing work. Those with whom I've had useful conversations about MIMs: Eric Grossman, Carl Reintsema, Todd Harvey, and Mike Wengler. Pam Wheeler for her continual assistance in course registration and keeping my academic paperwork in order. Karen MacKenzie and Helen Frey for their purchasing and administrative assistance. I'd like to thank my classmates and friends Richard Waters and Andrew Cahill for a multitude of intriguing discussions. I would like to thank my friends outside of solid-state: Mahesh, Shawn, Tim, Vipul, Patrick, and Vimal each of whom has helped in their own way. Finally, I must thank my parents: Jim and Darlene, and my sister: Trish, for their continual support and encouragement without which this thesis would not exist.

This project was sponsored by DARPA, in conjunction with the U.S. Army Research Office, under contract number DAAG55-98-C-0036. The views and conclusions in this document are those of the author and do not necessarily reflect the position of the government, and no official endorsement should be inferred.

TABLE OF CONTENTS

LIST OF FIGURES

I. INTRODUCTION AND GOALS

i. Background

The search for an environmentally clean and renewable energy source to supplement and one day replace our current sources is under continual investigation. Alternatives, such as: wind, tidal, thermal, biomass, and solar do exist though they are not yet cost-effective enough to serve as a replacement.

A solar cell was first witnessed by Becquerel in 1839 when he observed photovoltaic action from an electrode immersed in an electrolyte solution. However, it was not until 1941 that the first p-n homojunction photovoltaic device was developed and the 1970's before reasonable efficiencies (20 %) were obtained (Bube, 1983).

As of 1999, the highest efficiency for a solar cell was 32.6 % manufactured with GaAs/GaSb under concentration of 1000 suns. For larger area modules with a size greater than 700 cm^2 efficiencies decrease. Single crystalline silicon currently reaches a conversion efficiency of 22.7 % (Emery, 1999). The sun provides approximately 100 mW/cm^2 at the earth's surface and on a single day provides enough energy to accommodate the needs for all the earth's inhabitants for 27 years. However, to make this so-called "pipe-dream" (Simpson, 1997) a reality it is necessary to make solar cells efficient.

The required materials and their associated expense, toxicity and pollution concerns, can limit the feasibility of manufacturing. Even for common materials incorporating the exotic patterning required to obtain high efficiency through light trapping further increase the cost of manufacturing (Zhao, 1999). In order to entice both the environmentally and economically minded markets to use solar cells high efficiency and low-cost solar cells must be developed.

The theoretical upper limit in semiconductor solar cell efficiency is due to the collection mechanism. Incident photons from the sun excite electrons from the valence band of the semiconductor across the band gap into the conduction band. The generated electron-hole pair is separated and creates a potential across an external load. Even when every incident photon with energy greater than the bandgap of the semiconductor produces an excited electron the full energy of the photon may not be utilized. This is because electrons excited far above the band gap of the semiconductor by energetic photons thermally relax to the conduction band edge resulting in an energy loss.

Higher efficiencies may be possible by making a paradigm shift. Instead of using the particle viewpoint of current semiconductor solar cells where a free carrier is generated by the incident photon we could instead exploit the wave nature of the photon and extract the photon energy by rectifying its electric field. We can allow the wave nature of the incident photon to dominate the response if we concentrate the energy of the photon to a device that is much smaller than the photons wavelength and responds quickly enough to keep up with the oscillations of the photon field. This scenario is enacted with an antenna and rectifying element.

An antenna is used to couple electromagnetic energy to a region smaller in dimension than the wavelength of the radiation. By placing a rectifying element at the apex of the antenna the energy of the photon may be rectified. By using a broad band antenna a range of photon energies may be efficiently collected and concentrated across the diode.

If the number of incident photons is low and the incident photon is “rectified” in a sufficiently short time period we can collect each incident photon individually. For this situation we may calculate efficiencies at each wavelength individually. To make this possible the system designer must use care when incorporating these rectifying cells into a large area solar panel. Interconnects between the various rectifying cells must account for the fact that different cells across the panel may each be producing a different voltage and current depending upon the energy of the photon collected. Efficient interconnects between each rectifier cell is a nontrivial implementation issue. The power produced from each rectified photon must be efficiently extracted and used or stored before the next photon arrives for optimal efficiency (unless the two photons are coherent and have the same energy). In this thesis I consider only single rectifying cells coupled to a single frequency of electromagnetic radiation.

Lithographic metal-semiconductor-metal (MSM) Schottky diodes, using the monolithic membrane-diode (MOMED) process in GaAs, have been shown to perform at 2.7 THz (Martin, 2001). N-type GaAs is used in the Schottky diodes with the highest cutoff frequency because of the higher electron mobility in GaAs as compared to Si. (Sze, 1981). Transport through the quasi-neutral region of the Schottky diode and the skin effect add a series spreading resistance which reduces the diodes cut-off frequency (Champlin, 1978). The cutoff frequency is further reduced by the depletion capacitance which increases as the square root of the doping density.

Point contact GaAs Schottky diodes operate at higher frequencies than lithographic counterparts. For mixing and square-law detection beyond approximately 12 THz the GaAs Schottky diodes are outperformed by metal-insulator-metal (MIM) diodes (Hübers, 1994).

From both a material and functional viewpoint, MIM diodes may provide a suitable rectifying element. MIM diodes are rectifying electron devices made out of metals and insulators. The advantage of the MIM diode over semiconductor rectifiers is its extremely fast response time and wide bandwidth. These attributes make possible the promise of higher speed detection and mixing of optical radiation.

MIM diodes have been investigated by researchers since the early sixties (Kale, 1985). Early optical mixing experiments used 10.6 μm radiation to illuminate a tungsten point contact MIM diode and demonstrated the diodes high speed operation (Hocker,1968). In Hocker’s experiments a tungsten wire, that served as an electrode and a dipole antenna, was brought into contact with a counter electrode. Counter electrodes of silver or steel produced a detectable signal while a counter electrode of silicon resulted in no detectable signal.

Experiments using MIM diodes in the visible frequency regime (632.8 nm) were also carried out (Faris, 1973). MIM diodes have been used to directly mix laser radiation and standardize the length of the meter (Baird, 1983; Jennings, D.A., 1986). MIM diodes that exhibit a highly nonlinear current vs voltage curves, such as those formed using superconductors rather than normal metals, are the standard for high performance millimeter and submillimeter heterodyning (Rieke, 1996).

The point contact MIM diodes suffer from poor mechanical stability, but offer higher performance than the lithographic counterparts due to their smaller junction size. In more recent times research on MIM diodes has been underway to improve the lithographic MIM diodes in detection and mixing of microwave radiation (Femeaux, 1998).

MIM diodes for solar energy conversion, as opposed to mixing and detection, has been explored to a lesser extent. NASA supported research investigating the use of MIM diodes in solar energy conversion and found that the primary limitation was the mode conversion from the surface plasmons induced on the antenna to the MIM diode junction (Anderson, 1983). However, Gustafson has shown that coupling to the junction is limited by fabrication and that theoretically 100 % coupling efficiency can be obtained. Gustafson found the primary limitation of MIM diodes was the appreciable current flow under reverse bias in the diode itself (Gustafson, 1982).

This thesis represents a portion of an effort dedicated to the application of MIM diodes to direct conversion of the solar spectrum. My efforts presented in this thesis are focused on the MIM diode alone. Two goals of this thesis are to first prescribe what structure, including junction area, barrier thickness and barrier heights, are required in an MIM diode for solar energy conversion. Second, to estimate the conversion efficiency of MIM diodes to determine if they are a viable alternative to conventional semiconductor based solar cells.

To accomplish this goal I present both theoretical characteristics and experimental fabrication results of large area planar MIM diodes. I present calculations of the dark current vs voltage curves of MIM diodes that do not use the approximations typically found in the literature. I develop a classical circuit model of MIM diodes using PSpice. I apply photon assisted tunneling theory to MIM diodes to calculate the characteristics of MIM diodes under illumination and the solar energy conversion efficiency of MIM diodes. I detail the characteristics required of MIM diodes for efficient solar energy conversion. Finally, I present a novel metal-insulator diode structure that increases the asymmetry over conventional MIM diodes.

I did not integrate MIM diodes with antennas or experimentally test the large area MIM diodes under illumination. I do not model antennas but assume the solar energy is coupled to the MIM diode with 100 % efficiency.

ii. MIM Diode Operation

In MIM diodes tunneling is the predominant transport mechanism. The operation of the MIM diode is as follows. Metals, with two different work functions in this case, are joined together with an insulator sandwiched between. The insulator has predominantly been the native oxide of one of the metals produced by sputter oxidation, gas phase oxidation, anodic oxidation, vapor deposition, thermal oxidation, gas phase oxidation, or simply exposing the surface to air. In addition to these techniques we have at our disposal atomic layer deposition.

The shape of the energy band diagram is determined by four quantities: the work function of metal one ϕ_1, the work function of metal two ϕ_2, the electron affinity of the insulator χ_{oxide}, and the bandgap of the insulator E_g. The latter quantity, E_g, is generally large enough that the valence band of the insulator is off the scale of the diagram. The ideal band diagram for a MIM structure in equilibrium is shown in Figure (1-1).

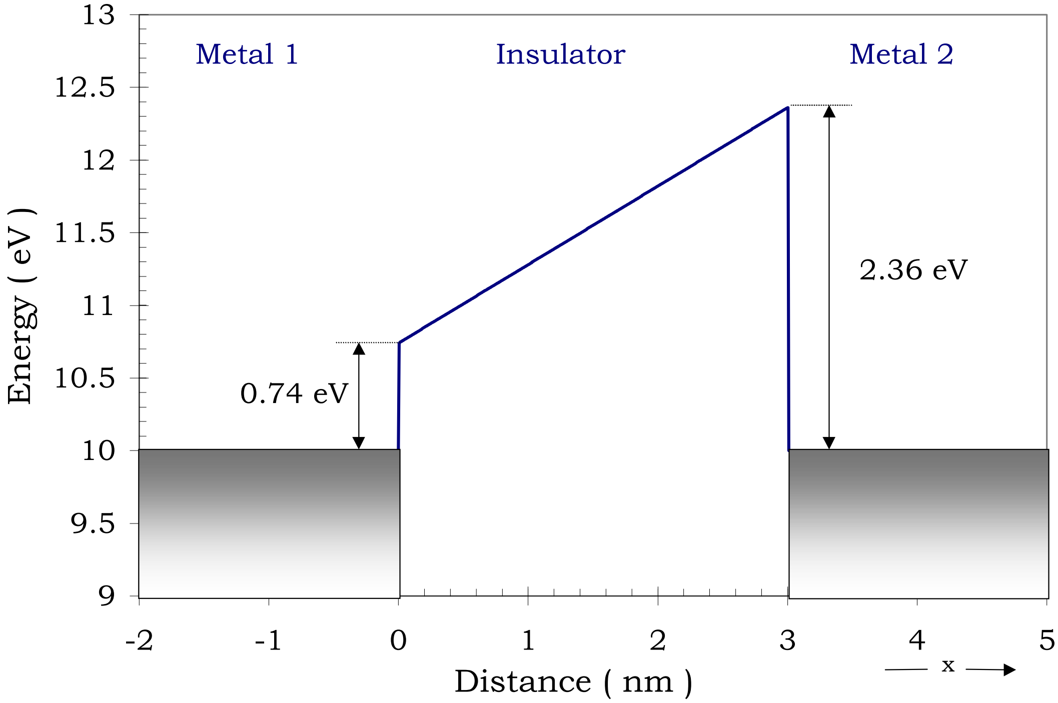

***Fig. 1-1**. An ideal MIM band-diagram. Two different metals are used resulting in a built in electric field across the insulator. The Fermi level of both metals is assumed to be 10 eV.*

Consider current transport in the absence of illumination (i.e., the static current vs voltage curve). Applying a negative DC voltage across the structure alters the band diagram as shown in Figure (1-2).

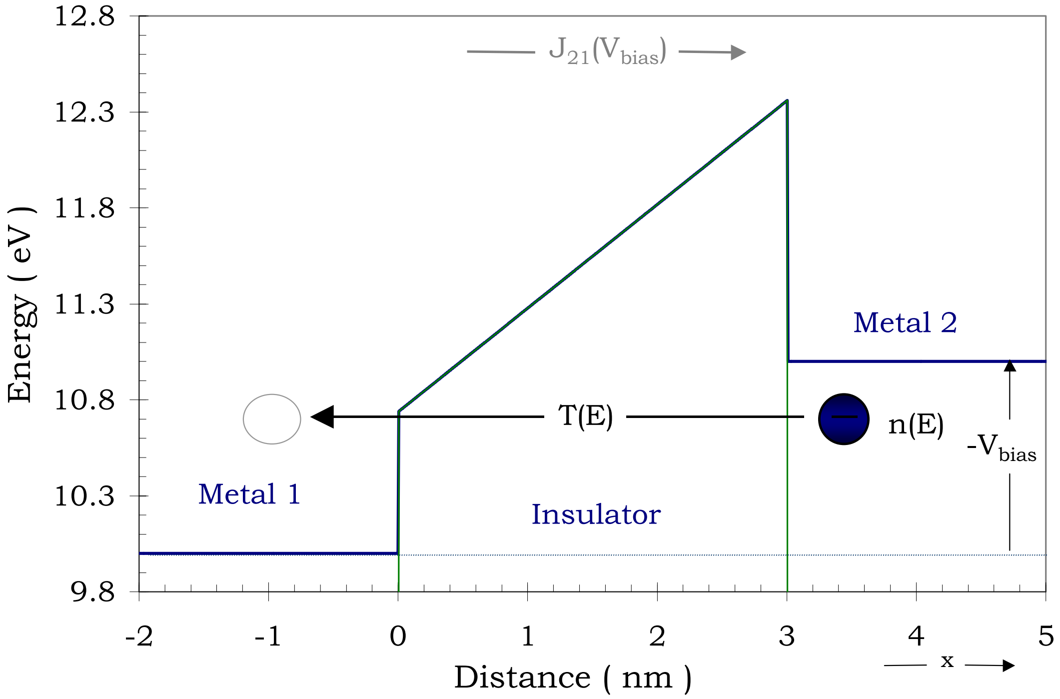

Fig. 1-2. *The ideal MIM band diagram with a negative bias voltage applied to metal 2. The concentration of electrons in metal 2 n(E) have a probability T(E) of tunneling into metal 1.*

With the applied voltage shown in Figure (1-2), electrons in metal two may tunnel into the empty states in metal one. The important quantity to determine is the probability that an electron, of a given energy, in metal two tunnels through the barrier into the empty states of metal one.

Given a sufficiently thin oxide layer (< 10 nm) quantum mechanical tunneling of the electrons through the classically forbidden insulator region is possible. The tunneling probability is a function of the applied voltage. The applied voltage is slightly larger than the barrier height on the left hand metal (ϕ_1-χ_{oxide}). As we increase this voltage further the width of the oxide region near the Fermi level decreases. The decrease in tunneling distance results in an increase in tunneling current. We may also apply a positive voltage to the contact and expect the same phenomena to take place, this time with carriers tunneling from metal one to metal two. As before, we expect an increase in carrier current when the tunneling distance begins to decrease, i.e. voltages above (ϕ_2-χ_{oxide}). It is the difference in work functions of the two metals that leads to an asymmetric I(V) curve. I will present the precise shape of the I(V) curve and full theory in Section III.

iii. Illumination of MIM Diodes

There are different models applicable to illuminated MIM diodes. The appropriate model depends upon the specific shape of the MIM diode J(V) curve and the frequency and intensity of the illumination. Figure (1-3) depicts the different models and the regions where they are most applicable.

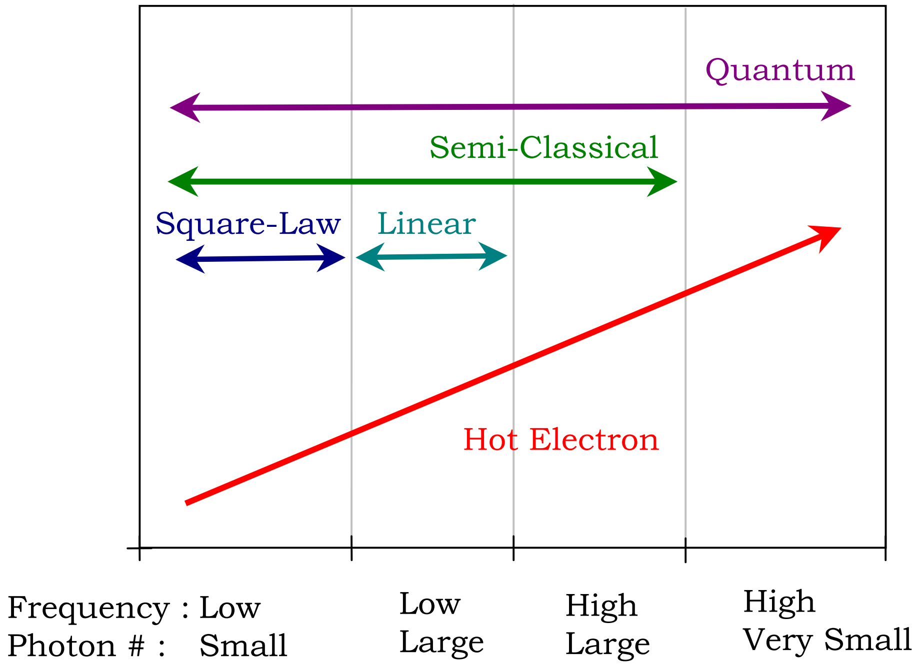

Fig. 1-3. *The various illuminated MIM diode models and their projected range of applicability. Hot-electrons, which may occur without an antenna, are increasingly important at high frequency.*

The specific definition of high and low frequency and high and low photon number depends upon the I(V) curve for the unilluminated MIM diode. I will define high and low frequency more clearly in Section V.

If an antenna is used to couple the incident radiation across the oxide of the device the electric field will induce a voltage across the oxide of the MIM diode. For low frequencies the device operates as a classical rectifier. The classical regime is divided into two regions: linear and square-law rectification. When the magnitude of the oscillating voltage is small, corresponding to a low number of photons, square-law rectification applies. The MIM diode is not functioning as a switch but rather produces a rectified voltage due to the nonlinearity in the I(V) curve. As the size of the oscillating voltage increases linear rectification applies. As we will find in Section IV, for a MIM diode functioning as a rectifier the maximum operating frequency is limited by the RC time constants.

As the frequencies increase the size of the electromagnetic quanta become sizeable in comparison to the voltage width of the nonlinearity in the unilluminated MIM diode J(V) curve and classical rectification theory is no longer appropriate. The semiclassical theory of photon assisted tunneling, which does not quantize the electromagnetic radiation, accounts for the quantum size of the electromagnetic field. This theory limits to the classical theory at low frequencies. If the number of photons incident decreases or coupling between the radiation and the MIM diode is strong a full quantum calculation is required. In the full quantum calculation the electric field of the incident radiation is quantized (quantum electrodynamics).

If an antenna is not used to illuminate the MIM diode, tunneling carriers may be created by hot-electrons. Each incident photon couples its energy to a single electron that is excited to a higher energy level. If the excited electron is near the barrier region and possess the proper momentum it may tunnel through the junction, producing a current. If the electron relaxes, rather than tunneling through the barrier, the absorbed quanta will be re-emitted. For low frequencies the probability for the electron to tunnel through the barrier is low and consequently the device does not exhibit an optical response. As the photon energies increase, so to does the tunneling probability. Consequently in Figure (1-3) I have depicted the hot-electron model to be present in all regimes, but with decreasing importance at lower frequencies. I will present the theory for MIM diodes using hot-electron emission in Section VI.

iv. Thesis Organization

I will begin in Section II by presenting the MIM diodes fabricated through the course of this thesis work. All of the MIM diodes I fabricated are planer devices fabricated either with a shadow mask or photolithography. The measured dark current vs voltage curves will be presented. In Section III I will present the theory of the MIM diode's unilluminated I(V) characteristics. Calculations I made on the specific role of the material selection on the MIM diode operation will presented. Comparison between the theory and experiment will be presented. In Section IV, I present the theory of MIM diodes coupled to antenna's which are illuminated with low frequency electromagnetic radiation. A PSpice model I developed to simulate this situation is presented. In Section V I present the quantum theory of photon assisted tunneling applied to solar energy conversion with MIM diodes to extract conversion efficiencies. In Section VI I present the hot-electron theory applied to MIM diodes used for solar energy conversion. In Section VII I present resonant tunneling concepts which I used to enhance the asymmetry found in the current vs voltage characteristics of MIM diodes. I conclude in Section VIII with the ramifications of this work and suggestions for future work.

II. EXPERIMENTAL MIM DIODES

In structure MIM diodes are elementary electron devices. Despite this conceptual simplicity fabricating functional and reliable MIM diodes is challenging. Even with today's advanced lithographic technology the majority of MIM diodes used in practice are of the point contact variety. In this section I present several of the MIM diodes that I have fabricated through the course of this thesis work. I detail the fabrication techniques, measurement apparatus, and the measurement results.

i. MIM Diode Fabrication

To fabricate an MIM diode we must consider the substrate, the metals, the oxide and the patterning technique. I begin this section by exploring each of these components. I discuss the various methods and materials I tried using and why. A table of the MIM diodes fabricated is included in Appendix III.

Substrate

I used a variety of substrates to fabricate MIM diodes upon. The first MIM diodes I fabricated were on microscope slides simply because the slides were inexpensive and readily available. Additionally, microscope slides would allow for optical illumination of the MIM diode through the substrate.

Cleanliness of the substrate is crucial. The oxide of a MIM diode is typically less than 5 nm thick and easily shorted or damaged by particulate contamination. I cleaned the microscope slides by rinsing them on a spinner at 500 rpm. The specific chemical sequence used was trichloroethylene, acetone, 2-proponal and finally a spin dry at 6000 rpm. The chemicals were CMOS grade manufactured by JT Baker (JT Baker, 2001) and dispensed through a squeeze bottle onto the slide for a minimum of 30 seconds each.

I thermally evaporated metal from a tungsten boat onto the microscope slide and inspected the surface quality under an optical microscope using 5 to 80X magnification in both reflection and dark-field viewing modes. The evaporated metal layers on the microscope slide were found to be rough and contained visible particles. The problem was linked to the inadequate cleaning process. I attempted to reduce the particle problem by introducing a physical scrub of the microscope slide using Micro soap in de-ionized water (DI water) prior to the chemical rinse (International, 2001). The physical scrub was done by hand in an overflow rinse tank using gloves. The physical scrub visibly reduced the number of particles on the substrate though not to a satisfactory level. Consequently, an alternative substrate was sought.

I tried using round fused silica flats to fabricate MIM diodes on. The fused silica flats were expected to have a smoother surface. The ability to illuminate the MIM diode through the substrate would not be lost. I used the same physical scrub and degrease procedure used on the microscope slides. The number of visible particles was reduced further but not to a satisfactory level.

I decided to use silicon as the substrate for MIM diodes. Silicon is a flat readily available substrate that can be subjected to many proven cleaning solutions. Silicon's only disadvantage is that it would not allow for illumination of the MIM diode through the substrate in the visible spectrum.

I used silicon wafers with various crystalline orientation and doping levels. I grew a wet thermal oxide on the wafers that was at least 1 μm thick. The oxidation conditions were 1000 °C for 4 hours. The oxide was necessary to electrically isolate the MIM diode from the silicon substrate.

The wafer, typically three inches in diameter, was subsequently scribed into one inch squares and cleaned. Everyone questioned about the best method to clean silicon seemed to have their own favorite recipe or procedure. I investigated and attempted several of these cleaning procedures; some were successful, some were not. The cleaning procedure that I eventually found to be the most successful was the RCA clean (Iscoff, 1993). The RCA clean consists of the following steps:

Oil removal

1) SPM solution (1:1 solution of hydrogen peroxide and sulfuric acid)
2) 12 minute soak in SPM
3) 12 minute DI water rinse

Organic contaminant and metal removal

1) SC1 solution (5:1:1 solution of DI water, ammonium hydroxide, and hydrogen peroxide)
2) 12 minute soak in SPM at 80 ˚C
3) 12 minute DI water rinse

Oxide removal

1) Dip in 6:1 BOE for 45 seconds
2) Rinse in DI water for 25 seconds

Atomic or ionic component removal

1) SC2 solution (6:1:1 solution of DI water, hydrochloric acid, and hydrogen peroxide)
2) 12 minute soak in SC2 at 80 ˚C
3) 12 minute DI water rinse
4) Blow dry with nitrogen

Any unnecessary step introduced into a cleaning sequence is considered to be a “dirty” step. As a result, I eventually omitted the buffered oxide etch (BOE) step from my cleaning sequence. Omitting the BOE is acceptable because I intend to use the oxide of the silicon for electrical isolation between the MIM diode and the silicon substrate. In practice I did not find omitting the BOE step to degrade the cleanliness of the oxidized silicon substrate.

The SC1 and SC2 solutions should be prepared fresh before each clean and kept well separated from each other to prevent the formation of crystallites (Campbell, 1996). The DI water in the two tank overflow system was maintained with a resistivity of 18.4 MΩ-cm. The first 2 minutes of the DI water rinse occurred in the designated “dirty” tank and the remaining 10 minutes took place in the “clean” tank.

The wafers were held in a PFA basket manufactured by Entegris (Entegris, 2001) throughout the cleaning process until the final nitrogen dry step. After the final DI water rinse the wafers were removed using clean metal tweezers and carefully blown dry. The tweezers were always placed down wind of the nitrogen flow across the sample with the lower edge of the sample on a cleanroom wipe to absorb the water that was blown off the edge of the substrate. This substrate and cleaning procedure proved to provide a clean particle-free substrate.

Metals

MIM diodes were fabricated by depositing a base metal layer, oxidizing the base metal and applying a top contact. The metal deposition for all the MIM diodes I fabricated was accomplished by evaporation. There are three prerequisites for the base metal: adhesion to the substrate, a smooth uniform surface, and a suitable native oxide. I fabricated MIM diodes with base metals made of titanium, aluminum, chromium, nickel, and niobium. The titanium, aluminum and nickel were 99.99 % or greater purity purchased from Cerac, Inc (Cerac, 2001). The Cr metal was purchased from R.D. Mathis (R.D. Mathis, 2001). The niobium depostion was carried out by ITN Energy Systems using e-beam evaporation.

Obtaining good adhesion of the metal to the substrate turned out to be a monumental problem in MIM diode fabrication. The lab evaporator, which used a mechanical roughing pump and an oil diffusion pump (with a liquid nitrogen cold trap) required a watchful eye. The foreline pressure was kept below < 20 mT when opening the valve to the diffusion pump and during the evaporation to prevent oil backstreaming into the bell jar. Oil backstreaming into the bell jar would adversely affect metal adhesion and purity.

In theory higher evaporation rates produce a higher purity film due to a lower incorporation of contaminants. However, I found that to produce a smooth metal surface the evaporation rate had to be kept low, in the range of 0.2 to 0.3 nm/s. For aluminum, a covered boat was required to prevent splattering of the Al. Chromium was evaporated from a chromium-coated tungsten rods, while the other metals were evaporated from tungsten boats.

In MIM diodes the base metal forms a native oxide. This native oxide layer can make contacting the base metal difficult. As a result, contact pads were eventually incorporated into the MIM design. Initially silver was used to form the contact pads until I found that the oxygen plasma steps, incorporated into the photolithography procedure, oxidized the silver. Additionally, the silver would naturally oxidize over time. Gold proved to be a superior contacting material as it endured the processing steps the MIM diodes were subjected to and did not oxidize over time.

Almost two years into the project I found that the metals suddenly no longer adhered to the oxidized silicon substrate. The adhesion was evaluated using the "tape-test." The tape-test is a rudimentary experiment where a piece of tape is applied to the evaporated metal layer and then removed. The metal is pulled off the substrate with the tape unless there is good adhesion of the metal to the substrate.

Changes in metal adhesion immediately supports the possibility of oil backflowing into the bell jar; oil was found on the surface of the bell jar. The evaporator system was completely dismantled, sandblasted and cleaned with aluminum wool and 2-propanol. Subsequently the system was "baked out" using quartz filaments and heating empty boats. The metal adhesion, though improved, was not satisfactory and a solution to the direct adhesion of silver, gold and aluminum to silicon dioxide was not found.

As a result, I introduced metal bonding layers to improve adhesion between the contact pads and the substrate. Initially titanium was used as a bond layer.

However, I later discovered that titanium would break up and scatter across the substrate when subjected to the oxygen plasma and lithography development.

Chromium proved to be the best bonding metal as it readily adheres to silicon dioxide and is not damaged by oxygen plasma processing. The thickness of the chromium adhesion layer was typically 100 nm. This is much thicker than required for a bond layer. The 100 nm thick chromium served a dual purpose as a bond layer and electrical contact pad. Gold alone is soft and easily scraped away by tungsten probes during contact. Chromium alone oxidizes and provides an unreliable contact. By placing gold on top of chromium, the gold prevents the chromium from oxidizing and the chromium eliminates poor contacting if the tungsten probe scrapes through the gold.

Although the adhesion of the gold to the SiO_2 substrate was ensured by using a Cr bond layer I was restricted to low temperature processing. The combination of gold and Cr, when subjected to an elevated temperature (274 ^{o}C and greater) would result in rough mounds forming on the surface as shown in Figure (2-1). This occurred to lesser degrees as the temperature was decreased.

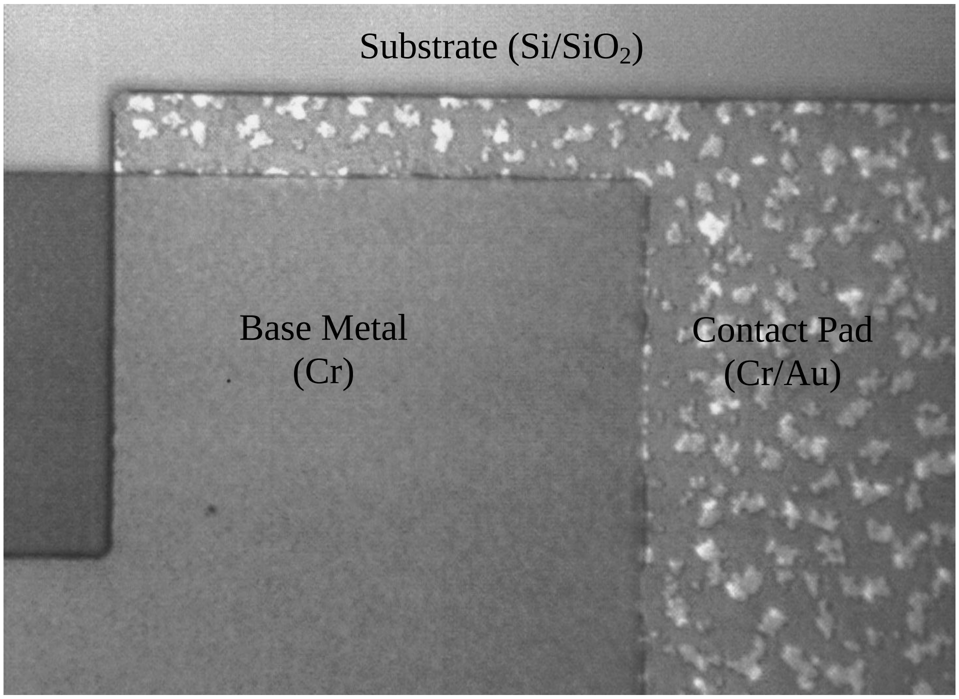

Fig. 2-1. *Microscope image of a portion of the contact pad and base metal on MIM163 (80X). The sample was heated to 274 °C to oxidize the base metal. The rough mounds are isolated to the Au/Cr portion of the pad.*

Despite the damage induced by high temperature oxidation and annealing, the 100 nm Cr bond layer with a 100 nm of Au provided the most reliable contact. The reason to subject contact pads to these temperatures is to increase the oxide thickness on the base metal and remove any excess surface oxygen. Gewinner showed that Cr_2O_3 produced at room temperature resulted in an excess of oxygen at the surface that could be removed by a 500 ˚C anneal (Gewinner, 1978). It is unknown what, if any, effect this surface layer of oxygen has in MIM diodes.

Oxides

The oxide of the MIM diodes were formed by five different techniques: anodic oxidation, evaporation, thermal, room temperature, and atomic layer deposition (ALD). The quality of the oxide is crucial to MIM diode performance.

Initial oxides were formed by anodic oxidation of titanium in an attempt to repeat devices formed by Garret Moddel in 1982. Anodic oxidation is a self-limiting chemical process where the sample to be oxidized serves as an anode and is submersed in an electrolyte separated from a non-oxidizing cathode. A potential is applied between the anode and cathode. The current is limited and eventually drops to zero as the oxide reaches a thickness that is limited by the magnitude of the applied voltage (Deeley, 1938). Titanium forms an anodic oxide of 1.5 nm/V (Maissel, 1970).

In anodic oxidation, the chemistry of the oxidation solution is of extreme importance in order to form a quality oxide and prevent the anode metal from going into solution rather than oxidizing. If the pH of the electrolyte is incorrect the oxide may redesolve after formation. Without a proven recipe to go by, I attempted an electrolyte of 100 ml acetic acid and 900 ml of tap water.

The anode was formed by titanium evaporated on a glass slide that was approximately 1” × 1” in size and a tungsten rod served as the cathode. The voltage source was raised slowly to maintain a current less than 200 μA until 4 volts was reached and the current decreased to less than 3 μA. Although I was able to form an oxide, the oxides were found to be visibly non-uniform. Limiting the current to less than 60 uA increased the uniformity of the titanium oxide. Uniformity of the titanium oxide was further increased by forming a 2 V oxide in an electrolyte of 50 ml acetic acid to 100 ml tap water.

Despite the visible improvements in the anodic oxidation attempts the MIM diodes electrical characteristics were unrepeatable. Most MIMs were shorts. Investigating the literature for anodic oxidation I found that anodic oxidation is most suitable for thick oxides (> 10 nm) and often contained ionic current components (Diesing, 1999). As a result alternative oxide formation techniques were sought.

Further investigations of anodic oxidation of titanium should begin with alternative electrolytes. Climent has produced TiO_2 films suitable for capacitors at low voltages using non-aqueous solutions of sodium acetate in ethyl glycol (2.97 %) (Climent, 1993). The aqueous solutions of nitric acid to water (1.79 %) were found to form nonuniform and poorly adhering oxides. Higher oxidation rates may also be possible by simultaneous illumination with UV radiation (Kalra, 1994). Additionally, higher dielectric constants can be obtained by anodic oxidation at elevated temperatures (Shibata, 1994).

I made several attempts to form the oxide by evaporation of silicon monoxide. I used thermally evaporated silicon monoxide in a previous project for alignment layers in ferroelectric and nematic liquid crystal cells and was familiar with the evaporation procedure (Eliasson, 1999). I evaporated 2 nm and 6 nm thick SiO layers on a titanium base metal with chromium top contacts to form MIM diodes. Unfortunately, the evaporated SiO was found to contain pin-holes and resulted in shorted devices. Attempts to reduce the pinholes in the SiO by moving the substrate during the evaporation were unsuccessful.

Atomic layer deposition was next used to form the oxide layer in MIM diodes. The atomic layer deposition of Al_2O_3 was carried out by Jason Klaus and Stephen Ferro from Steve George's research group in the chemistry department at the University of Colorado at Boulder. ALD is a self-limiting chemical deposition process. Water, transported by nitrogen, is introduced into a tube chamber containing the sample to be coated. Hydrogen peroxide has also been shown to produce Al_2O_3 (Fan, 1991). By chemisorption the wafer is fully coated by one molecular layer of water. The system is then flushed with nitrogen. Trimethylaluminum or TMA, $Al(CH_3)_3$, is next introduced into the chamber using the nitrogen carrier gas. TMA reacts violently with the water on the surface of the substrate resulting in the formation of Al_2O_3. The TMA is then flushed out with nitrogen and the process is repeated until the desired thickness of Al_2O_3 is obtained (George, 1995).

Initial ALD films proved to be problematic for several reasons: making electrical contact to the metal below the ALD film, long range uniformity in oxide thickness, and large currents in response to applied voltages. The long range non-uniformity in oxide thickness was verified by ellipsometry. A non-uniformity in oxide thickness results in a scatter in the current magnitude measured from contact to contact on a single substrate.

ALD oxide thickness on chromium substrates was measured with a manual ellipsometer using a wavelength of 632.8 nm at an incident angle of 70 degrees. A Cr sample with a native Cr_2O_3 layer was tested prior to the ALD deposition to extract n and k values for the uncoated substrate. I obtained a composite value for the Cr/Cr_2O_3 substrate of n=3.34 and k=2.266 (Tompkins, 1993). Using a nominal value of Al_2O_3 dielectric constant of 1.77 I calculated the Δ vs ψ trajectory for the single film in Figure (2-2) and extracted the oxide thickness from experimental Δ and ψ values.

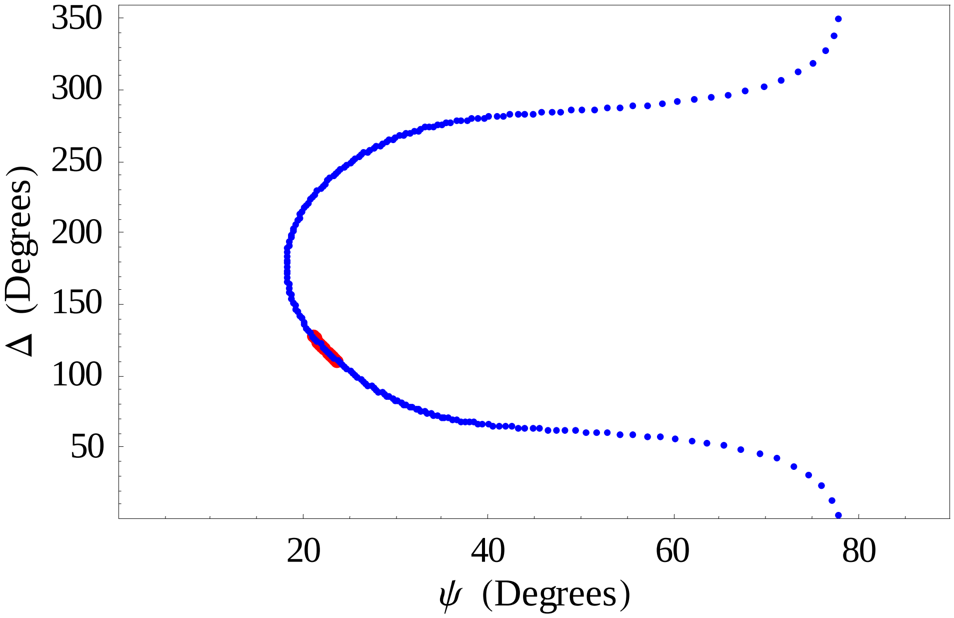

Fig. 2-2. *Calculation of the Δ vs ψ trajectory for a single film with n=1.77 on a composite Cr/Cr_2O_3 substrate. The region of the trajectory for a 0 to 10 nm thick film is shown in red.*

On MIM 12A-12D I measured the following oxide thickness from ellipsometry. For MIM12A, which had a nominal ALD thickness of 10 nm, I measured values of 7.7, 7.3, and 7.4 nm across the film. For MIM12B, which had a nominal ALD thickness of 4 nm, I measured values of 3.1, 3.5, and 4.1 nm across the film. For MIM12C, which had a nominal ALD thickness of 3 nm, I measured values of 3.7, 4.0, and 3.6 nm. For MIM12D, which had a nominal ALD thickness of 2 nm, I measured values of 2.9, 2.5, and 2.7 nm. The measurements indicate both a deviation from the nominal thickness and a deviation across the sample.

The large current magnitudes (90 mA/cm^2 at 0.5 volts through a 10 nm thick oxide) were speculated by Steve George to be due to hydroxyl groups within the oxide. As a result, several ALD MIM diodes were fabricated using various temperature anneals to drive out the hydroxyl groups. These experiments were inconclusive due to the melting temperature of the base metals being lower than the temperatures required to fully drive out the hydroxyl groups (1000 K). Furthermore, due to the slow turn-around time that we initially experienced with the ALD films I began investigating other oxidation methods. I later returned to using ALD oxides deposited by Jeff Elam from Steve George's group to form MIM diodes with a dual insulator layer.

A significant discovery during these initial MIM diode fabrication attempts using ALD was that the ALD did not adhere fully to the silver metal as it did to chromium and aluminum. As a result, I was able to use Ag to mask off regions of the substrate from ALD deposition and solve the problem of contacting to the base metal below the ALD film.

With semiconductors the best oxides are formed by thermal processes. Consequently I investigated forming Al_2O_3 by thermal oxidation of the base metal. I attempted to repeat the work of Pollack and Morris (Pollack, 1964). Pollack and Morris formed thermal oxides of aluminum and subsequently MIM diodes that matched theory. Various attempts were made to form MIM diodes in this manner. The evaporated base aluminum layer was oxidized for up to 54 days at 180 °C both in oxygen and ambient environments. All devices formed resulted in short circuits.

Subsequently, I attempted to oxidize the aluminum at elevated temperatures in hopes of forming a thick oxide, at which point I could then reduce the thickness of subsequent oxides to the desired thickness range by reducing the oxidation temperature. The oxidation was carried out in a tube furnace at temperatures between 400 and 500 ^{o}C for 20 minutes to 2 hours with an oxygen flow of just over 1 cm^2/s parallel to the sample. Lower flow rates in oxygen resulted in a visibly non-uniformity in the oxides.

After the oxidation, I noticed bubbles on the surface of certain aluminum samples. The bubbles were isolated to poor adhesion of the aluminum to the substrate. Using a tape test poor adhesion of the aluminum was confirmed and found not to occur in the samples with good adhesion. These experiments were carried out before I routinely used Cr bond layers.

I also noticed other particulates form on the surface of the aluminum after the oxidation. Close examination of these particulates showed their crystalline nature as shown in Figure (2-3).

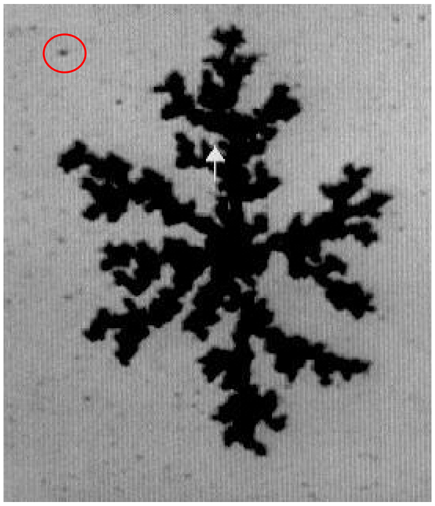

Fig. 2-3. *An 80 X optical microscope image of crystallization in* Al_2O_3 *formed by high temperature oxidation. Note also the bumps (one is circled in the upper left corner), that are formed on the surface of the aluminum oxide surrounding the crystallized region.*

A publication by Wefers and Misra explains that the growth of crystaline aluminum oxide occurs at temperatures greater than 377 ^{o}C. The crystalline aluminum oxide is coincided by cracking in the amorphous aluminum oxide layer that is formed at lower temperatures. Consequently, for tunnel quality oxides we should oxidize at temperatures below 377 ^{o}C. Aluminum oxide may be formed in the presence of water or dry. However, if water is present the concentrations of water, oxygen, and aluminum must be carefully controlled to prevent the formation of alumina gels. These gels of aluminum are not the electrical device quality oxides desired and result in the formation of crystallized "chunks." (Wefers, 1987)

In parallel with the high temperature oxidation experiments I attempted to oxidize the aluminum base metal at room temperature. Most MIM diodes formed at room temperature were short circuits. However, several functional MIM diodes were fabricated. Given this finding, along with the crystallization problems associated with high temperature aluminum oxidation, I decided the best way to obtain working MIM diodes was by near room temperature oxidation of the aluminum base metal in a dry environment.

The environmental control was provided by the bell jar of the evaporator. A moveable shadow mask was developed which allowed the position of the shadow mask with respect to the sample to be shifted from outside of the bell jar without breaking vacuum. Multiple electrodes were installed in the evaporator so that different metals could be evaporated during a single pump down. An oxygen bottle, fitted with particulate filters and line dryers, was also connected to the evaporator so that the bell jar could be back filled with pure dry oxygen during the oxidation stage. I could then fabricate successful MIM diodes within the bell jar of the evaporator.

Completely controlling the environment is not possible for MIM diodes formed using photolithography since a portion of the fabrication process occurs outside of the evacuated bell jar. The lithographic MIM diodes were oxidized either in an ambient environment or in a separate chamber that had oxygen flowing over the surface of the samples directly from an oxygen bottle. This continuous oxygen flow over the sample eliminated the possibility of organic contamination during the oxidation process.

I also used the native oxide of Cr to form the oxide of MIM diodes. From my experiences using Cr to form electrical contacts I knew it formed an oxide. Under thermal oxidation conditions Cr forms Cr_2O_3 (Fu, 1981). Cr_2O_3 produces a smooth oxide, due to ion migration following the Mott-Cabrera Model, up to 600 ˚C (Young, 1977). Native oxidation of Cr in air produces an oxide approximately 2 nm thick and moisture has no effect on the oxidation condition at higher temperatures (Alessandrini, 1972). Cr turned out to produce good MIM diodes.

Patterning

Patterning MIM diodes was accomplished by either direct evaporation through shadow masks or using photolithography and lift-off or etching techniques. Patterning MIM diodes using shadow masks has the advantage that it is a cleaner process since no photoresists or chemical developers are involved. Photolithography has the advantage that much smaller device areas can be obtained along with the formation of many more MIM diodes in a single fabrication run.

For MIM diodes fabricated using shadow masks initial devices were made by evaporating an unpatterned base metal layer over the entire surface of the substrate. This base metal was then oxidized and top contacts were evaporated through a shadow mask. These devices required puncturing the native oxide of the base metal to make electrical contact to the base metal.

For certain metals, chromium in particular, puncturing the native oxide with the tungsten probes proved to be quite problematic and the resistance between the probe and the base metal was often large and dependent upon the contact pressure. Figure (2.4) shows the current vs voltage curve for a single chromium base metal layer while successively increasing the contacting pressure. A dramatic increase in current magnitude as the tungsten probe punctures through the oxide is evident.

Freshly deposited silver pads, the top dashed trace, have a low resistance on first contact.

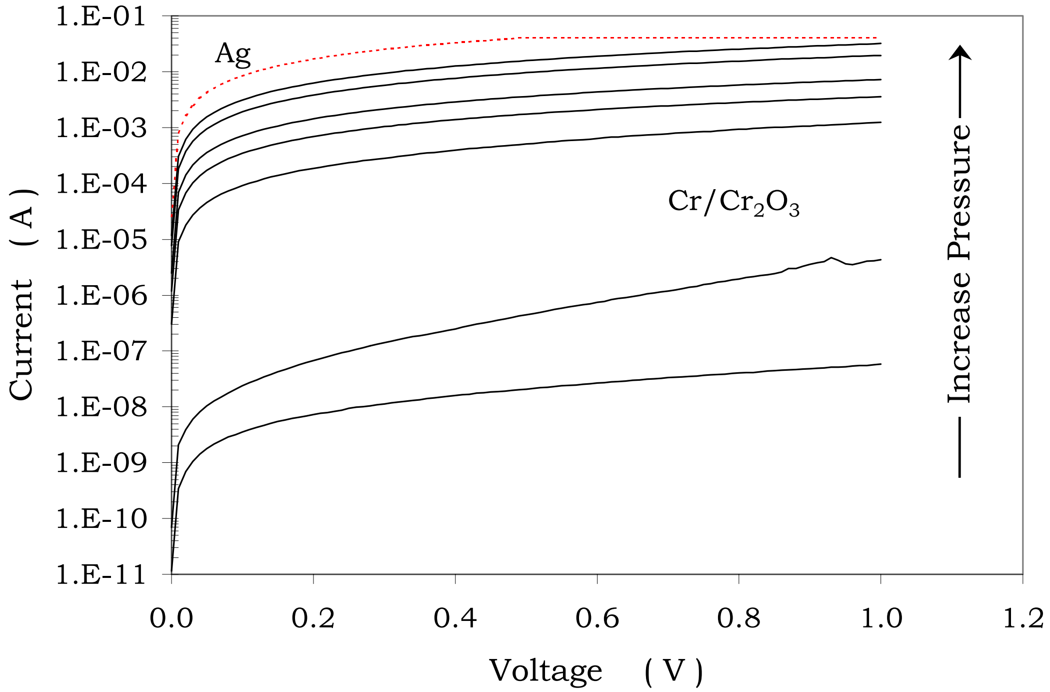

Fig. 2-4. *The current vs voltage curve for contacting the Cr/Cr$_2$O$_3$ base of MIM15 with successive increases in probe contact pressure. The top dashed trace is for the first contact of freshly deposited Ag metal. The current is limited to 40 mA.*

Furthermore, obtaining a top contact to the device required probing directly on top of the active junction area of the MIM diode which makes puncturing through the diode a possibility. The moveable shadow mask system, in addition to controlling the oxidation environment, allowed electrical contacts to be made away from the active junction area circled in Figure (2-5).

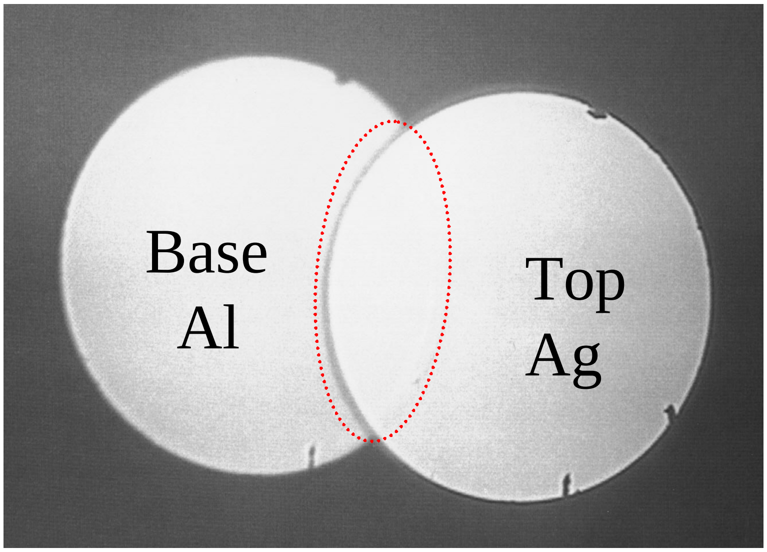

Fig. 2-5. *Microscope image of an MIM diode formed using the moveable shadow mask system. The active area of the MIM diode is outlined in red (Area=0.0014 cm^2).*

MIM diodes formed using the moveable shadow mask system were quite successful. The disadvantage of these MIM diodes was that the number of MIM diodes fabricated for each run was small (49), the junction area was large and only a single size device was produced for each run.

In order to decrease the junction area size and increase the number of MIM diodes formed for each fabrication run photolithography was introduced. For my initial efforts I did not have a dedicated mask for MIM diodes. Using old masks that had suitably shaped structures I formed MIM diodes by overlapping patterns from two subsequent photolithography steps by eye shown in Figure (2-6).

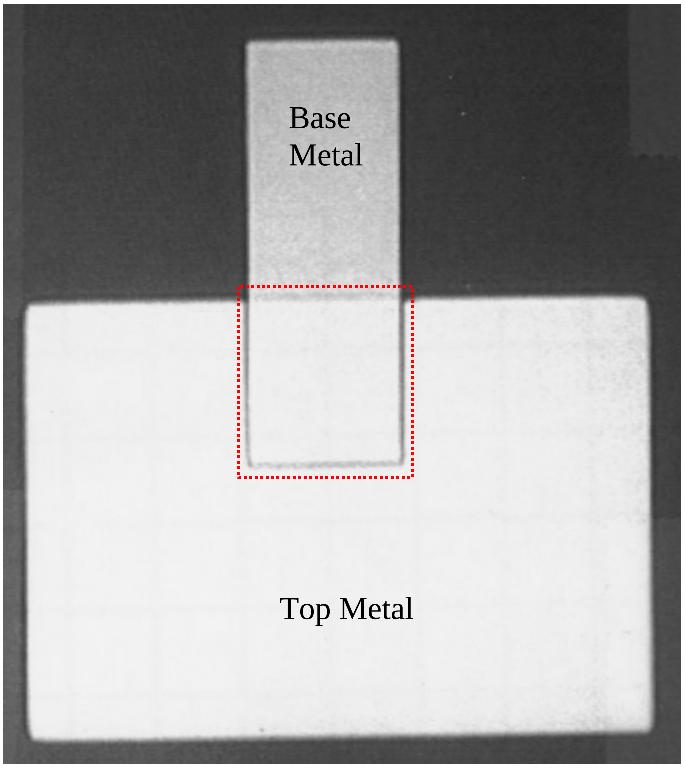

Fig. 2-6. *Optical microscope image of an MIM diode formed using photolithography. The junction area of the MIM diode is indicated by the red line. (Area=2.3 x* 10^{-5} *cm*^{2}*)*

Without a dedicated mask and proper alignment marks the device area fluctuated and obtaining a good back contact through the native oxide of the base metal remained problematic.

I designed a mask, in AutoCAD Light 97 (AutoDesk, 2001), specifically for MIM diodes. This mask incorporated base contact pads and produced many MIM diodes of various areas on a single substrate. Ultimately, all lithographic MIM diodes were fabricated using this mask shown in Figure (2-7).

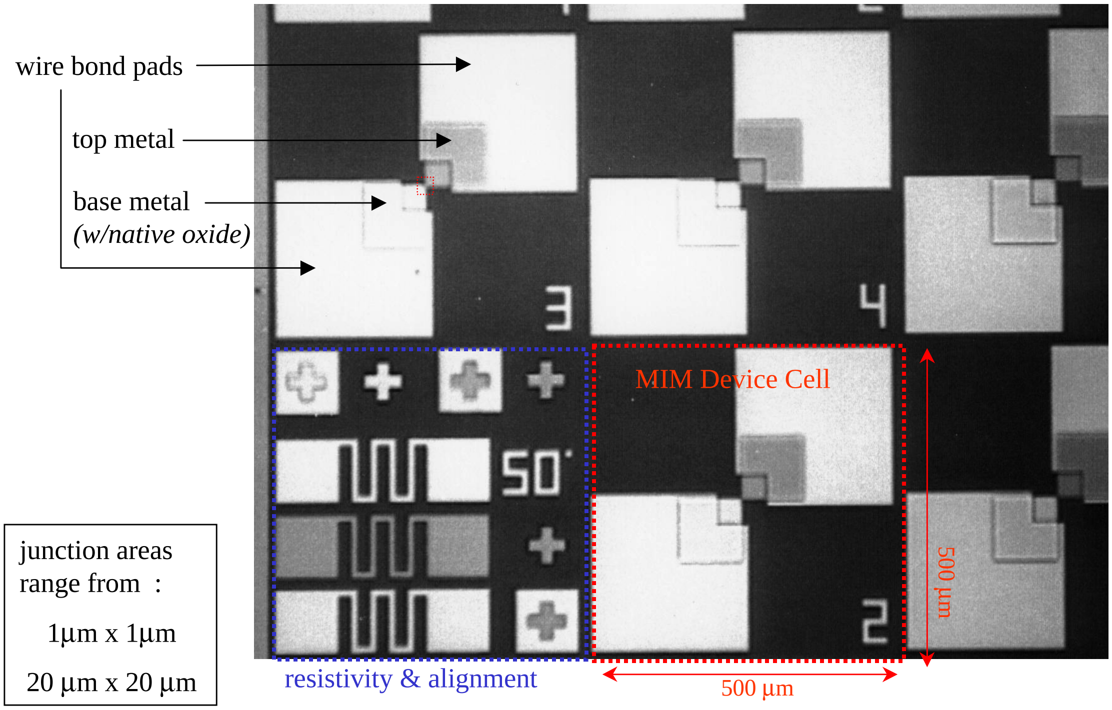

***Fig. 2-7.** Optical microscope image of an MIM diode formed by the dedicated MIM diode mask. An individual MIM diode cell (outlined in red) is 500 µm x 500 µm, with device areas ranging from 1 µm^2 to 400 µm^2. The region in the lower left of the image includes structures for alignment among the three lithography layers and evaluating the resistivities of the metals.*

The photolithography process I used was almost exclusively lift-off with positive photoresist. Although etching would be preferred in many situations because it allows for thicker metal layers and a cleaner process, it was not always possible due to the chemical etch attacking one of the previously deposited layers. Lift-off works by using a negative image of the desired pattern. The resist was removed by the developer in regions that were exposed to the UV light through the photolithography mask.

The developed openings were cleaned with an oxygen plasma system. I found that the developer, even with overdevelopment (or even acetone), would completely remove resist from a wafer once applied. The oxygen plasma was able to remove residual resist that was left in the developed regions and ensure good metal adhesion. The oxygen plasma system would also sputter old resist from the electrodes onto the sample. These resist splatters were approximately 100 nm in diameter. Placing the samples on clean quartz plates prevented sputtering from the electrodes.

Metal was then evaporated onto the substrate both over the resist and into the openings. The photoresist is approximately 1 μm thick, which limits the maximum metal thickness that can be lifted off. Once the evaporation was complete the sample was submersed in acetone to remove the resist and the overlying metal layer leaving only the metal that was evaporated into the developed resist openings on the substrate. If the metal layer was too thick, or the photoresist overdeveloped ultrasonic cleaning was used to encourage the lift-off.

The specific photolithography steps are outlined below.

1) Spin on HMDS at 6000 rpm for 30 seconds
2) Spin on positive resist at 6000 rpm for 30 seconds
3) Pre-bake photoresist at 90 ˚C for 25 minutes
4) Align sample with mask using Karl Suss mask-aligner
5) Expose resist to UV light for 27 seconds
6) Develop resist for approximately 60 seconds
   (4:1.2 of DI water to AZ400K developer)
7) Rinse resist in DI water (3 beaker rinse, minimum 30 seconds each)
8) Blow dry with nitrogen
9) 35 seconds at 200 W at 1 Torr O_2 Plasma

This process was repeated for each layer of the MIM diode.

ii. MIM Diode Measurements

A table of the MIM diodes fabricated during this thesis work is provided in Appendix III. I will now describe the equipment used to measure the MIM diodes and subsequently present a portion of the experimental data measured.

Measurement Equipment

Current vs voltage measurements were made with an HP4145 Semiconductor Parameter analyzer connected to a probe station (Agilent, 2001). Contact to the MIM diode was made using two tungsten probes. The resistance of the contact pads to the MIM diode were low enough that 4-terminal measurements were not used (Dunne, 1990)

Capacitance measurements were made using a Stanford Research SR530 dual lock-in amplifier (Stanford Research, 2001). A 0.01 V peak 1 MHz sinusoidal voltage was applied to the sample and provided as a reference to the lock-in. The sample was housed in a metal enclosure and with the tungsten probes. To calibrate the system I adjusted the phase of the lock-in, with the probes removed from the sample, until zero in-phase current was measured. This ensured that the resistance was infinite when the probes were removed and the circuit is open. The current 90 degrees out of phase was then treated as an offset due to stray capacitance of the wires and connectors. The probes were brought into contact with the sample and the resulting current, both in and out of phase was measured using the lock-in amplifier. The capacitance and resistance was then calculated (Schroder, 1998).

This technique for determining the oxide thickness does not include the field penetration into the electrodes. This field penetration results in a portion of the applied voltage being dropped across the electrodes and effectively decreasing the measured capacitance (Simmons, 1965). The field penetration, which has a more noticeable effect for thinner oxides, would result in an over estimate of the oxide thickness when extrapolated from C(V) measurements.

Un-illuminated Current vs. Voltage

MIM66 is an example of an MIM diode fabricated entirely within the bell jar of the evaporator. The substrate was cleaned with the RCA cleaning process. The base aluminum metal was evaporated at 0.25 to 0.3 nm/s through a shadow mask with 0.005 cm^2 holes. After evaporation of the base metal, the bell jar was backfilled with oxygen to 500 Torr and the sample was oxidized for 2 hours just above room temperature. The shadow mask was moved and 200 nm of silver was evaporated at 0.15 to 0.5 nm/s to form the top contacts. The resulting MIM diode had a measured area of 0.0014 cm^2 and was shown in Figure (2-5). The current density vs voltage plot for 10 of the MIM diodes are shown in Figure (2-8).

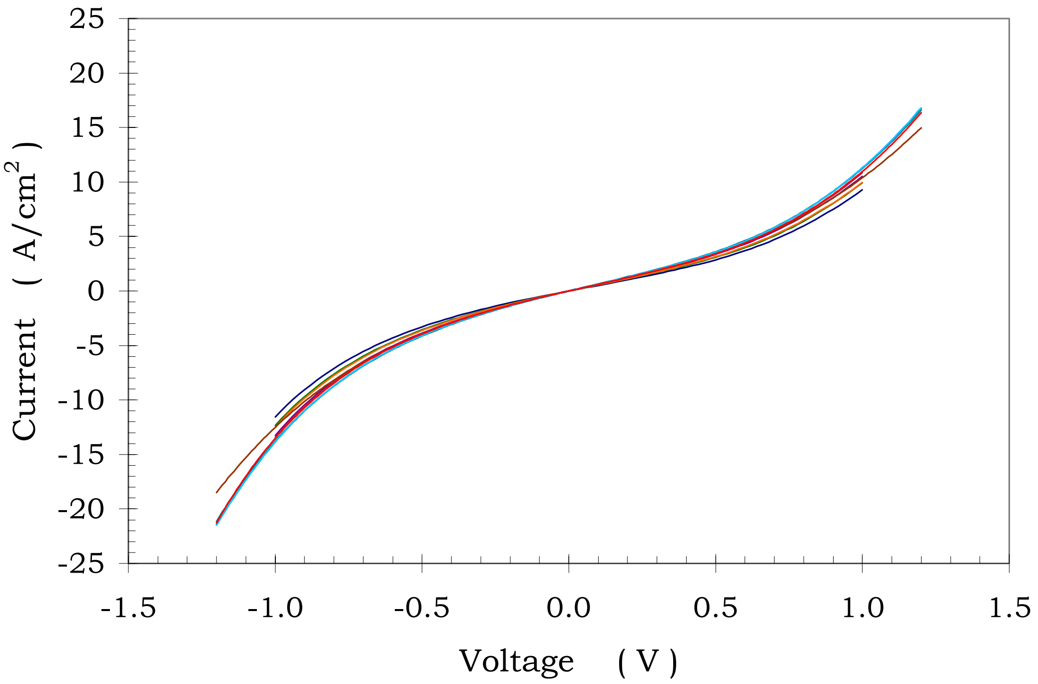

Fig. 2-8. *Experimental current density vs voltage measurement for 10 of the MIM diodes on MIM66 (Al/Al_2O_3/Ag). The area of the MIM diodes are approximately 0.0014 cm^2.*

MIM66 exhibited low scatter in current density magnitude from one MIM diode to the next.

Capacitance measurements estimated the oxide thickness to be 2.1 nm. The measured oxide thickness combined with literature values for the Al work function (4.28 eV), Ag work function (4.26 eV), and electron affinity of the Al_2O_3 (1.78 eV) result in simulations which agreed well in magnitude with the measured currents.

MIM84 is an example of a MIM diode fabricated by overlapping lithographic patterns. The base Nb metal was e-beam evaporated onto an Si/SiO_2 substrate. The Nb was then etched with a niobium etch solution made of 70 % nitric acid, 27 % H_2O and 3 % hydrofluoric acid (Lichtenberger, 1993). Following the etch the samples were cleaned with TCE, acetone, and IPA on a spinner (30 s each) and allowed to rest in an ambient environment for 3 days to allow the freshly etched edges to oxidize. Top silver contact pads were formed by a photolithographic lift-off technique. The active area of the devices is 5.2×10^{-5} cm^2. A MIM diode with a similar pattern was shown in Figure (2-6).

The experimental current vs voltage curves are shown in Figure (2-9).

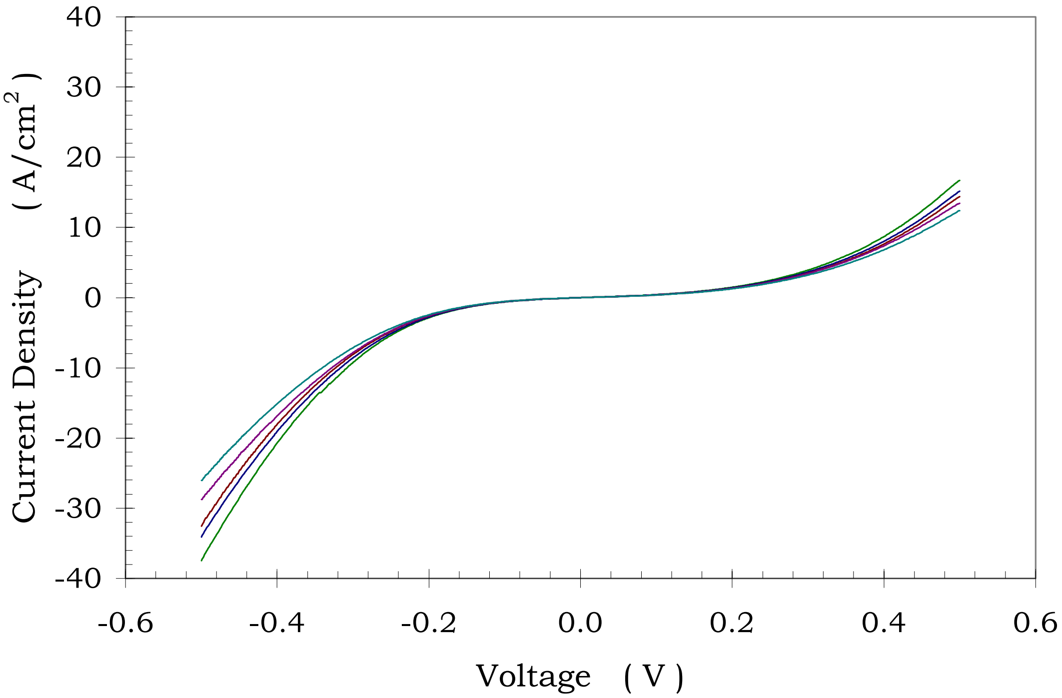

Fig. 2-9. *Experimental current density vs voltage curve for a Nb/Nb oxide/Ag diode MIM84. The MIM diode's area is approximately* 5.2×10^{-5} *cm*^{2}.

Several contacts are shown in Figure (2-9) and the scatter is reasonably low. The barrier between Nb and its native oxide is lower than the barrier between the silver and the niobium oxide. Consequently, we would expect higher currents under low negative applied biases.

MIM93 is a Nb/Nb oxide/Ag MIM diode that was fabricated with the dedicated MIM diode mask. In addition an argon plasma was used to mill down the thickness of the native niobium oxide in hopes of decreasing the resistance of the MIM diode. I found that the argon milling had three alternative effects. First, I found the measured currents scaled with edge length as shown in Figure (2-10).

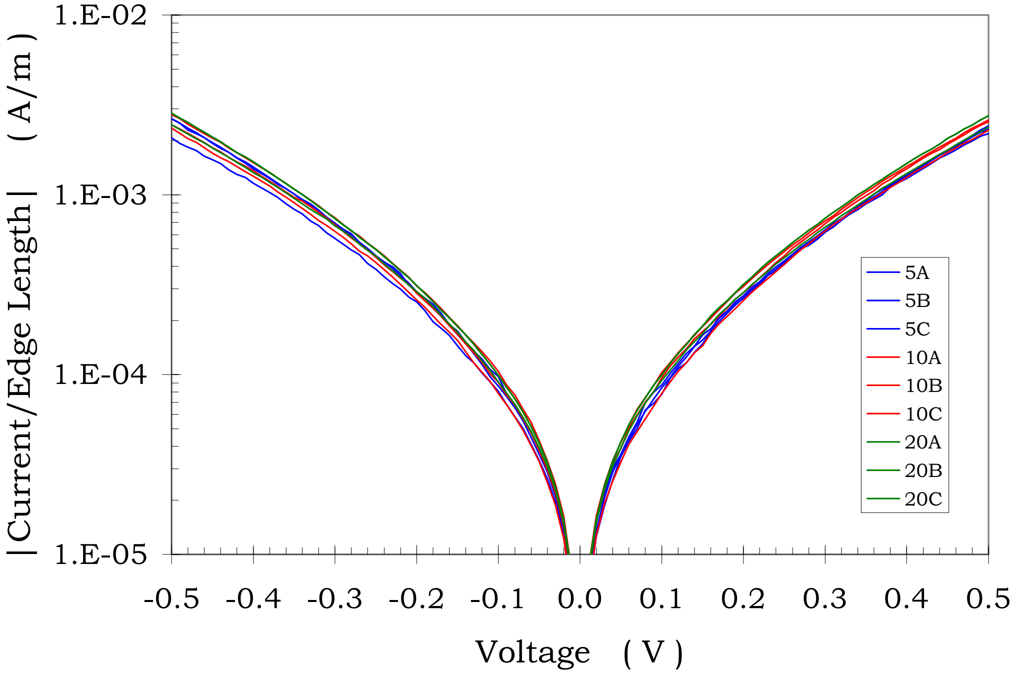

Fig. 2-10. *Experimental current density vs voltage curve for a Nb/Nb oxide/Ag diode MIM99. The niobium oxide was subjected to a 10 min argon plasma mill (Forward Power: 112 W, DC voltage: -218 V). The resulting devices did not scale with area, rather scaled by the length of the edge.*

In other words, the current did not scale by the area of the device as would be expected for MIM diodes but rather scaled by the length of the edge in the MIM diode. Second, milling resulted in a decrease in currents over MIM84. This is suspected to be due to sputtering aluminum off of the plasma system electrode which deposit onto the sample and subsequently oxidized to decrease the current. Third, the soft silver contact pads were visibly roughened due to the argon ion bombardment.

Aluminum MIM diodes formed with the moveable shadow mask were found to be stable for current vs voltage measurements that were repeated during a single measurement session. Measurements made a minimum of 24 hours later had a lower current magnitude than the previous day's measurement as shown in Figure (2-11).

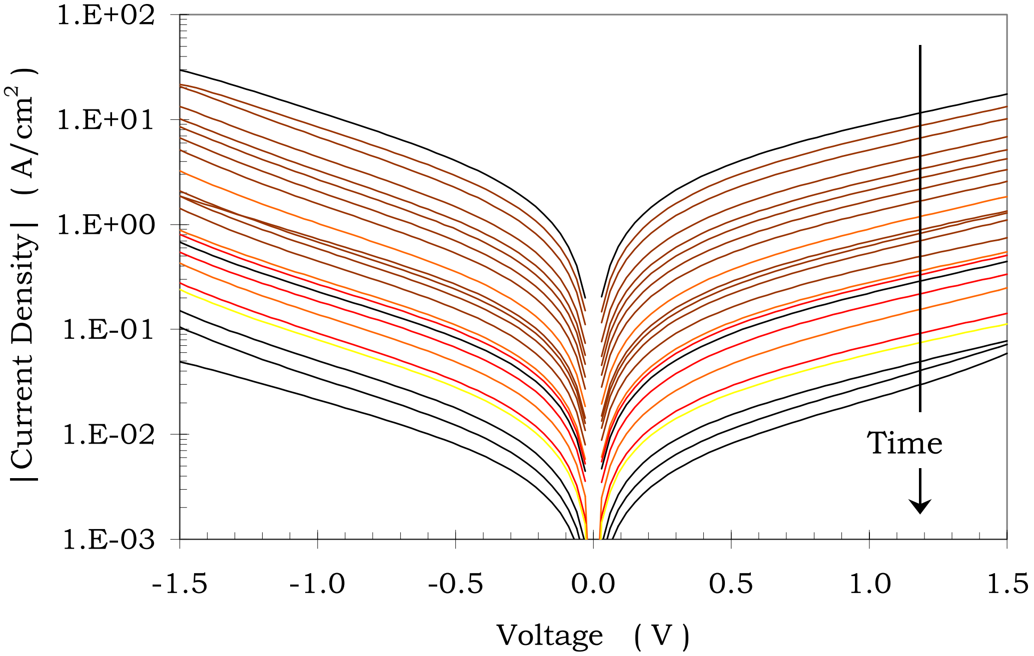

Fig. 2-11. *The current density vs. voltage measurement for MIM81 (Al/Al_2O_3/Ag). The decrease in current magnitude of a single contact over a two month period is shown. The time between measurements was a minimum of 24 hours. The diode area is approximately* 1.1×10^{-3} *cm*^{2}.

If the measurement was repeated 2 hours later the current density did not decrease substantially. Measurements taken more than 24 hours later did not appear to decrease substantially more than a measurement made exactly 24 hours later. A plot of the current density at positive and negative 1 volt vs time is shown in Figure (2-12).

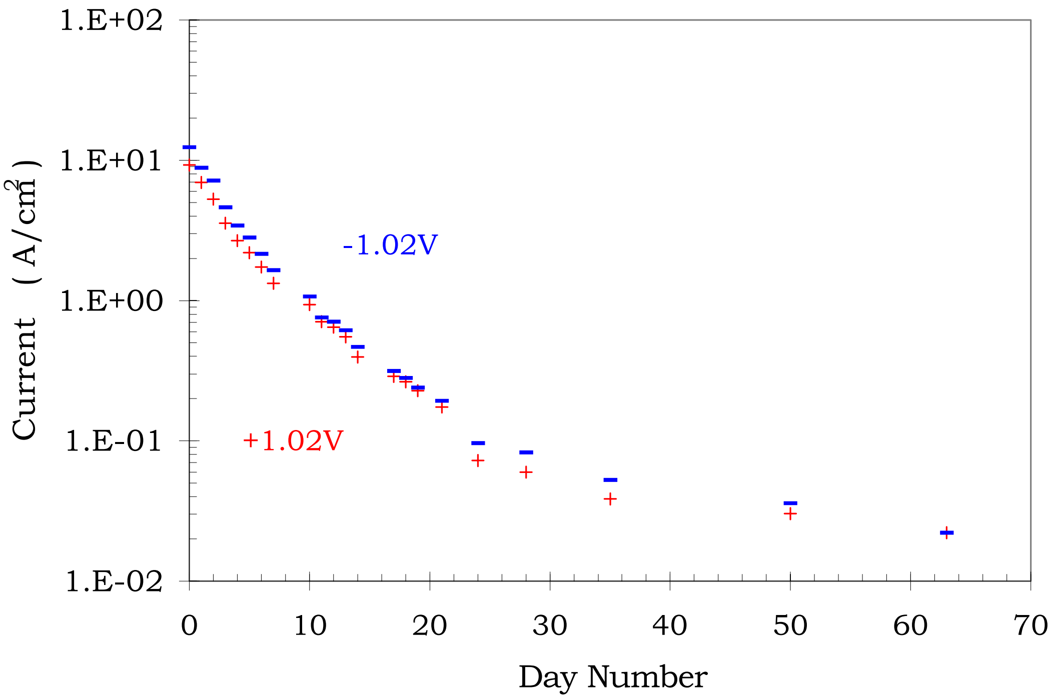

Fig. 2-12. *Current density for MIM81 at positive and negative 1.02 V vs the day the measurement was made.*

The substantial decrease in current indicates that the oxide thickness was increasing with subsequent measurements. MIM81 broke down to a short on the 62nd day.

I suspect this current decrease was the result of current induced oxidation of the aluminum (Snow, 1996). I speculate that the minimum 24 hour time period was the time required for the MIM diode to saturate with oxygen and moisture from the atmosphere and as a result facilitate the current induced oxidation. As the oxide thickness increased the electric field decreased subsequently decreasing the oxide thickness growth with time.

MIM106 is a small area Al/Al_2O_3/Ag MIM diode fabricated by photolithography. The base aluminum was allowed to oxidize by sitting in ambient conditions for several days. Measurements were made on a single 20 μm × 20 μm device. In the small area MIM diode I found a saturation time on the order of 10 seconds as opposed to the 24 hours required in the larger area devices. Furthermore, evidence for ions within the oxide was found in the smaller area devices.

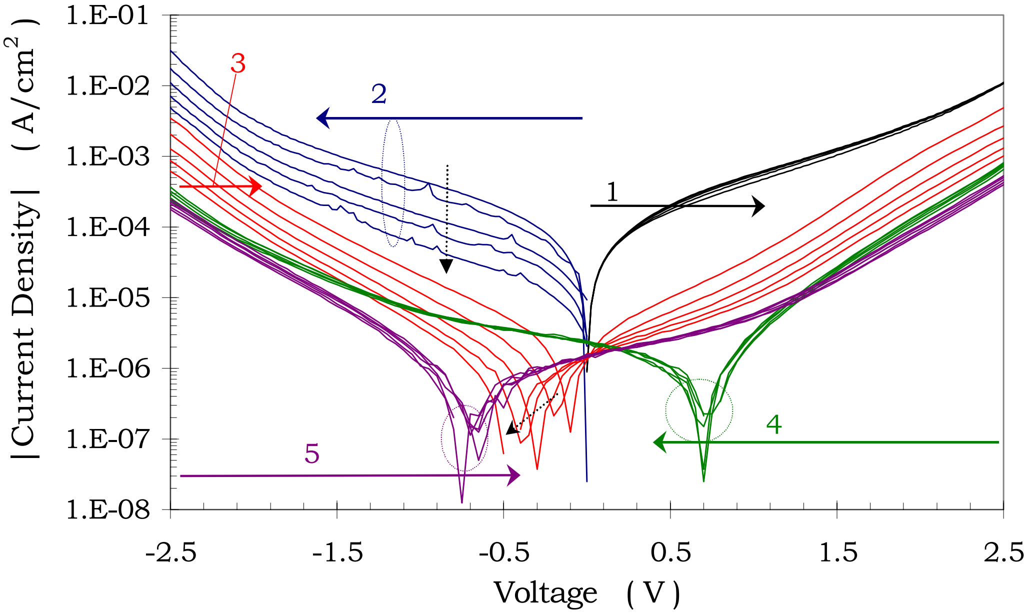

Fig. 2-13. *MIM106 (Al/Al_2O_3/Ag) exhibits rapid aging. The numbers and solid arrows indicate the measurement order and direction. The dashed arrows indicate the direction the current shifted between subsequent measurements. The size of the MIM diode is 20 $\mu m \times 20$ μm.*

In Figure (2-13) the initial sweep from zero volts to 2.5 V was repeatable with no decrease in current and no shift in the minimum of the J(V) curve. This indicates that if ions are responsible for the current lag they are not activated with a positive bias. This could be explained by saying that the ions are positive and located at the Al/Al_2O_3 interface. An argument for negative ions at the Al_2O_3/Ag interface could also be applicable though I will assume the former throughout.

The second measurement was a sweep from zero to negative 2.5 volts. A decrease in current was found to occur in this set of measurements. This current decrease may be due to shielding of the applied voltage by the activated ions or a increase in the oxide thickness due to field-induced oxidation. Field-induced oxidation is expected to be possible for electric fields of 10^7 V/cm. A –2.5 volt oxidation potential indicates that the native oxide of the Al was approximately 2.5 nm thick. Because there was no voltage shift in the J(V) curve minimum from zero in subsequent measurements the activated ions must redistribute from one sweep to the next.

The third sweep was from negative to positive voltage. The current magnitude continued to decrease with subsequent sweeps and a shift in the curve to the left is evident. This shift is due to ions in the oxide lagging behind the applied voltage. The magnitude of the shift is proportional to the number of activated ions in the system.

The fourth sweep was from positive to negative voltage. The current magnitude no longer decreased in this set of measurements. Furthermore, the minimum in the J(V) curve is of opposite polarity and equal magnitude to that of the previous scan. Either we have reached saturation in the number of ions that will be activated, or this sweep direction does not activate ions.

As we see in sweep five from negative to positive voltage, we have simply reached saturation. The current magnitude continued to decrease slightly, perhaps due to a small but continued field induced oxidation. The magnitude of the voltage offset was constant and much like sweep four the current magnitude continued to decrease only slightly.

The above process was repeated on a different contact. This time however, after a zero to positive voltage sweep the next measurement was taken from positive to negative voltage. The shift in the J(V) curve was evident. Again the magnitude of the offset in the current minimum reached a saturation.

I attempted to limit the aging process by depositing and subsequently oxidizing through a thin aluminum layer sandwiched between two silver electrodes. Unfortunately, the devices were all shorts (2 Ω). Using thermal evaporation, I was unable to produce thin continuous layers of aluminum.

It is possible that hermetically sealing MIM diodes would produce stable devices. However, due to the aging in these unsealed devices I abandoned aluminum and its native oxide.

I attempted fabricating several MIM diodes using a nickel base metal. I found that nickel evaporated from a powder source resulted in a highly resistive metal layer. Evaporating from nickel pellets resulted in 30 Ω resistors even for applied voltages from mV to volts. The problem was the evaporated nickel from our system exhibited inconsistent conductivity.

Subsequent MIM diodes were fabricated from chromium and its native oxide. Having fought with trying to contact chromium metal in the past I knew it would easily form a native oxide. Following some initial difficulty forming repeatable tunnel oxides I constructed a chamber so that the chromium could oxidize under the continuous flow of oxygen. This technique ensured organic contamination did not interfere with the oxidation process. Furthermore, my oxides formed from Cr_2O_3 did not show signs of aging or ions.

A symmetric MIM diode fabricated from chromium is shown in Figure (2-14).

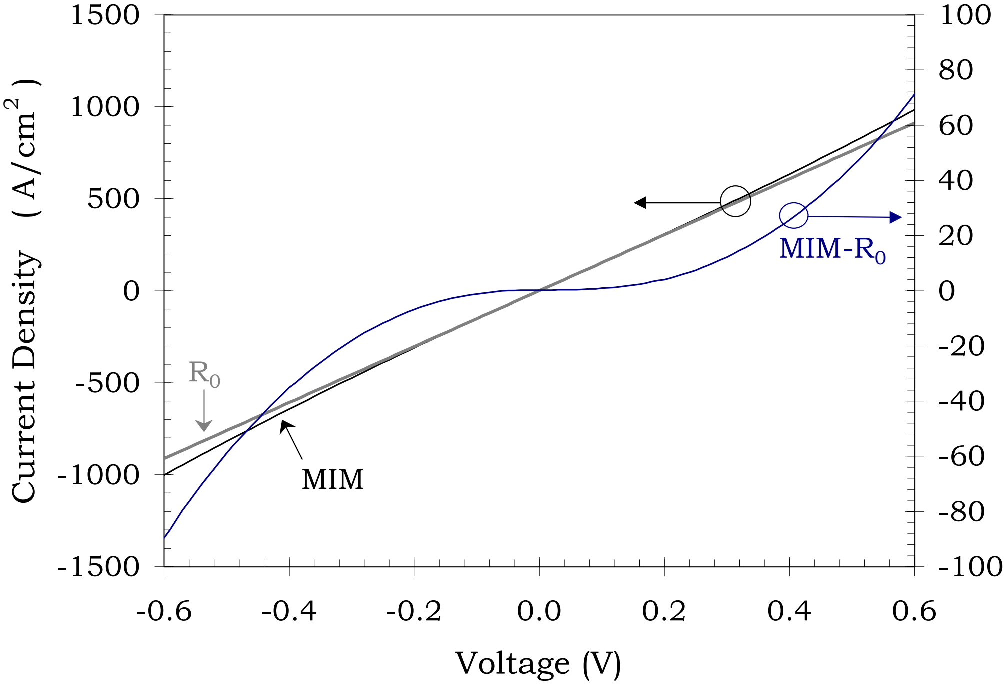

Fig. 2-14. *Cr-Cr_2O_3-Cr MIM diode (MIM161). The black trace is the MIM current density data. The thick gray trace is a straight line fitted to the zero bias resistance of the diode. The blue trace is the difference between the MIM diode J(V) curve and the straight line. This illustrate the nonlinearity in the MIM diode. The device size is 10 $\mu m \times 10$ μm.*

MIM161 had about an order of magnitude scatter in the current vs voltage curves from one MIM diode to the next. The J(V) curve was symmetric for all diodes measured. The nonlinearity was made evident by plotting the difference between the current vs voltage curve for the MIM diode from a straight line fitted to the zero bias resistance of the diode.

Asymmetry may be introduced into the system by using a top electrode made from a different material. MIM 162 has a top electrode made of palladium. The current vs voltage measurement for this diode is shown in Figure (2-15).

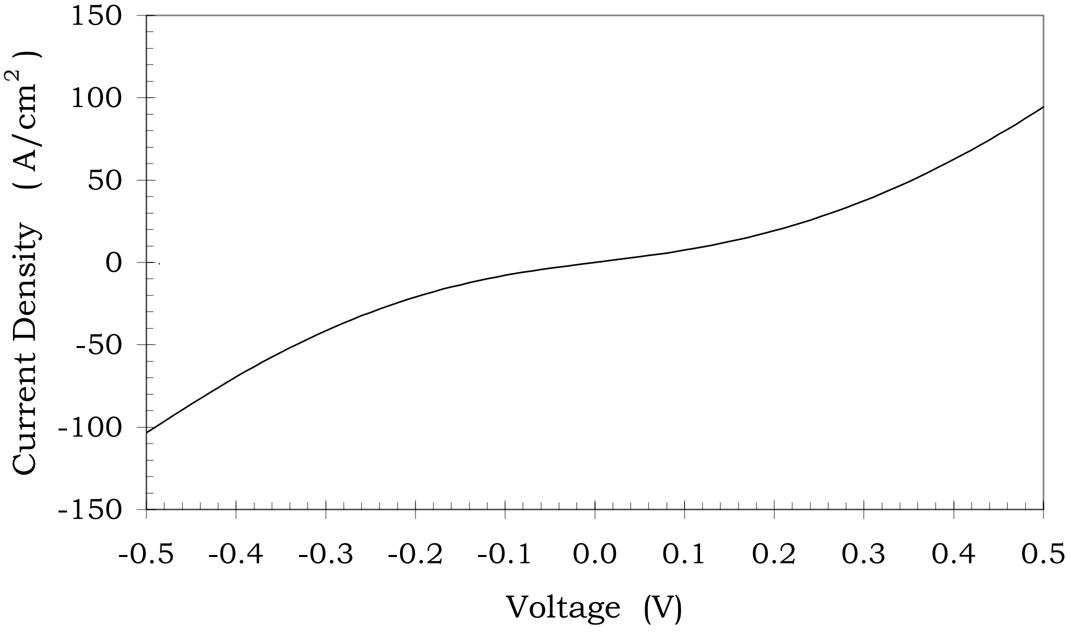

Fig. 2-15. *Cr/Cr$_2$O$_3$/Pd MIM diode (162). The device size is 20 $\mu m \times 20$ μm.*

The nonlinearity in the Cr-Cr$_2$O$_3$-Pd MIM diode is evident directly from the measured data. The current density has decreased from the symmetric chromium MIM diode. A decrease in current density is expected due to the larger barrier between Pd and

Cr_2O_3 as compared to Cr and Cr_2O_3. The barrier also introduces an asymmetry in the J(V) curve favoring negative bias voltages.

Even further asymmetry can be obtained by using a magnesium top electrode as shown in Figure (2-16).

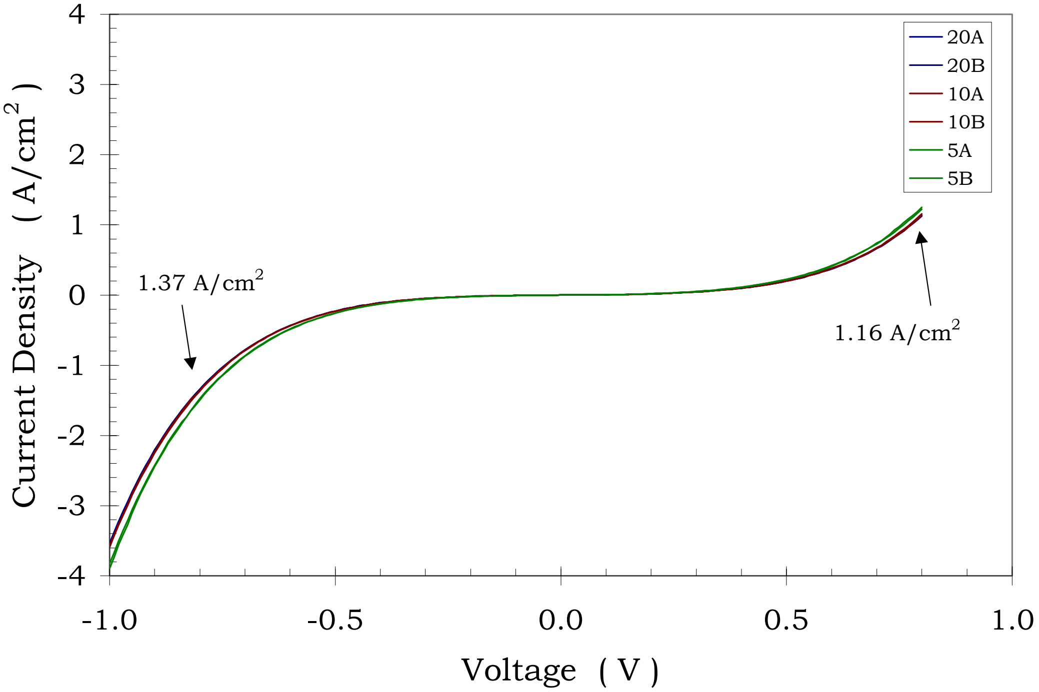

Fig. 2-16. *Cr/Cr_2O_3/Mg MIM-L152diode. The chromium oxide was formed under ambient conditions. The traces are blue for the 20 μm × 20 μm devices, the red for the 10 μm × 10 μm devices, and the green for the 5 μm × 5 μm devices (two of each device are plotted). The diodes broke down at forward applied biases greater than 0.8 V. The current densities for sample 10B at +/- 0.8 V are labeled.*

The diode made with a magnesium top electrode was found to have relatively little scatter in the current density from device to device. Additionally, the current scaled well with area.

In Figure (2-16) the diode to diode scatter in MIM152 is negligible for large area contacts. As the contact size decreased to less then 5 µm × 5 µm the diodes current density also decreased (the scatter among a given size group remained small). I speculate that this decrease in current magnitude with decreasing device size is due to over development in the photolithography process. Overdeveloping the resist results in rounding of the corners (visible through the microscope). Overlapping squares with rounded corners reduce the actual size of the MIM diode as compared to two overlapping squares without any edge rounding as shown in Figure (2-17).

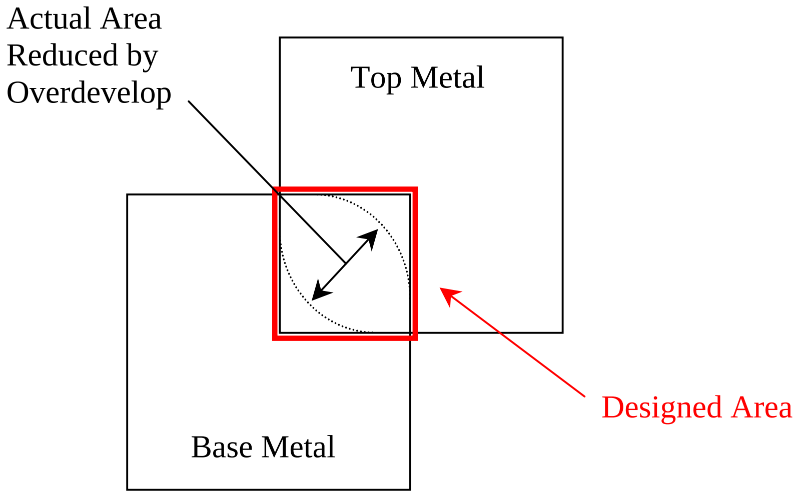

***Fig. 2-17.* – *Effect of overdevelopment on MIM diode area. Two squares represent the base and top metal layer overlapping to form the MIM diode. The red line outlines the MIM diode area formed by perfect squares overlapping. With improper development, the edges of the square are rounded (shown only on the overlapping corner). Rounding due to over development results in a diode area that is smaller than what would be produced by two perfect squares of the same size overlapping.*

In a lift-off process overdeveloping alone enlarges the squares while rounding the corners. However, the area I use to calculate area was measured from the width.

The rounding would occur on devices of all sizes but would have a more dramatic effect on smaller area devices. To correct for the rounding the area used in calculating the current density must be decreased which would inturn increase the current magnitudes.

While fabricating Cr MIM diodes I found that the thickness of chromium could be increased by elevating the temperatures. Oxidations at temperatures up to 500 °C were carried out. I also found that the oxygen plasma system both increases the oxide thickness and introduces an asymmetry into the system even when quartz plates were used to shield the sample from contamination. Using the oxygen plasma system on the Cr_2O_3 after formation did not introduce an asymmetry in the J(V) curve. Consequently, using the oxygen plasma system to clean and oxidize freshly coated chromium was abandoned.

The MIM diodes fabricated experimentally were all large area (greater than 1 μm × 1 μm) with thick (> 40 nm) contacts. No optical response was detected from these diodes. The diodes were fabricated to explore the different material systems assuming that the performance of the large area devices would be equivalent to the performance of the small area devices. Of the diodes I fabricated the ones with the most asymmetry were the $Nb/NbO_x/Ag$ and $Cr/Cr_2O_3/Mg$ diodes. The polarity of the asymmetry was in the direction expected from theory.

In conclusion, I have fabricated and tested MIM diodes made from oxidized base metals of Ti, Ni, Cr, Al and Nb and a variety of counter electrodes. Various substrates, cleaning procedures, patterning methods, and oxidation techniques were explored. I found the best MIM diode substrate to be an oxidized silicon wafer cleaned with SPM, SC1 and SC2. Thermal evaporation of metals should be carried out at a low evaporation rate to produce a smooth surface. My best oxides were formed by oxidizing the base metal in a chamber connected to dry oxygen. Contact pads made of chromium covered with gold resulted in both good adhesion to the substrate and good electrical contact. An oxygen plasma clean was required to fully remove the developed resist. Care must be taken to ensure that the oxygen plasma process does not contaminate the sample. Aluminum formed a good oxide but the fabricated devices were not stable over time. Chromium produced good MIM diodes that were stable over time. Finally, if atomic layer deposition is used either gold or silver may be used to selectively control the regions where the ALD alumina adheres to the sample. The comparison between the experimental diode presented and theory are presented in section III.

III. UNILLUMINATED MIM DIODE

In this section I present the theory of MIM diode current density vs voltage J(V) curve in the absence of illumination. Understanding the dark J(V) curve of MIM diodes is a prerequisite to effectively optimizing the device structure and calculating the response to optical illumination. Simulations based on the dark J(V) expressions help guide the material selection for optimal performance, gauge the quality of the fabricated devices, calculate the illuminated properties of the device, and the ultimate goal: predict the solar energy conversion efficiency of MIM diodes.

i. Current Density vs Voltage Theory

In this section I work through the theoretical expression for the current density vs voltage curve J(V) of the MIM diode in the absence of illumination. The final expression I develop for the J(V) relation in an MIM diode is equivalent to that found in Sze (Sze, 1981). However, the explanations provided there make it difficult to determine what assumptions are used. Furthermore, in the MIM diode literature it is standard practice to use the analytical approximation of the MIM diode J(V) curve derived by Simmons (Simmons, 1963) and use the WKB (Wentzel, Kramers, Brillouin) approximation to the electron tunneling probability (Griffiths, 1995). These approximations neglect the detailed shape of the insulating barrier.

I limit the number of approximations made and derive the J(V) curve from first principles. I use the independent electron approximation and develop a one-dimensional expression for the current density as a function of applied bias voltage. I focus on the MIM diode although in practice this same technique may be easily extended to the current density calculation for multi-layer metal-insulator tunneling systems as will be shown in section VII.

The energy band diagram for an MIM diode is presented in Figure (3-1).

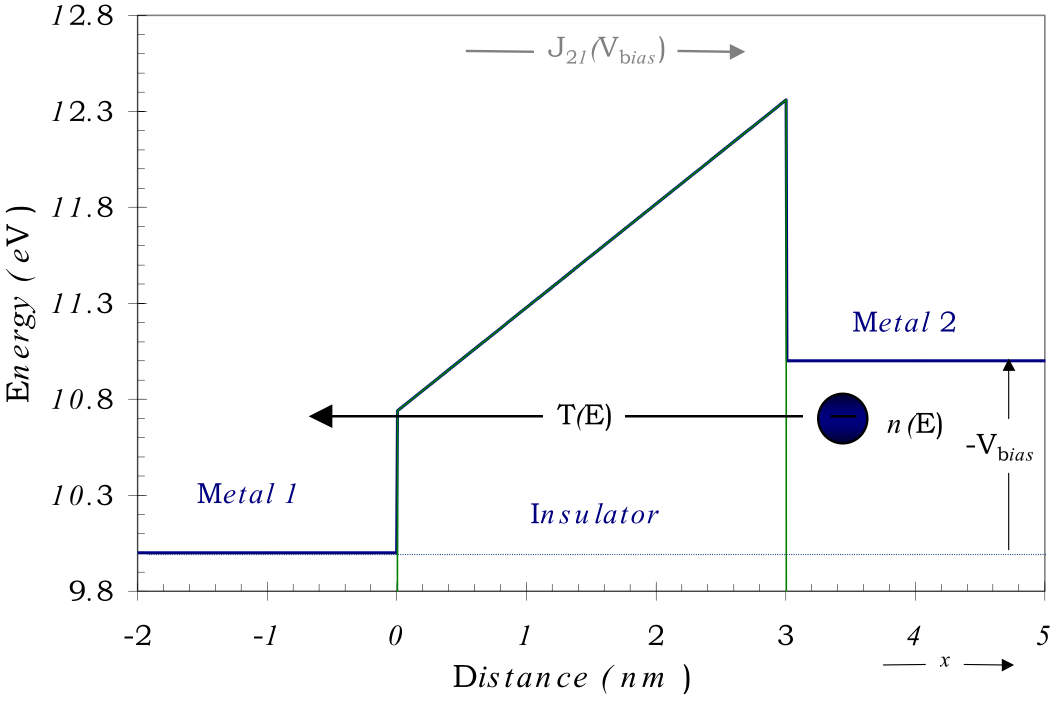

Fig. 3-1. *The energy band diagram for an MIM diode with a negative applied bias voltage. Electrons in metal 2 tunnel through the insulator and are collected in empty states within metal 1. The result is a current from metal 1 to metal 2.*

The particular material system of the MIM diode in Figure (3-1) is a Cr base metal (metal 1) with a 3 nm thick native chromium oxide (Cr_2O_3) and a top metal (metal 2) made of Pd. Material property values are provided in Appendix II. Due to the large bandgap of most insulators the valence band is generally omitted in the energy band diagrams of MIM diodes.

In Figure (3-1) a negative bias voltage is applied to metal 2, referenced to metal 1. The negative bias voltage results in a current from metal 1 to metal 2. The current flow in the MIM diode is due to electrons emitted from metal 2 that tunnel through the insulator and are collected in metal 1.

The current density is the product of: the charge carrier density passing through a plane perpendicular to the conduction direction per second, the carriers velocity in the direction of conduction υ_x, and the charge of the carrier -q. In an MIM diode, the number of carriers contributing to the current is limited by the concentration of carriers $n_2(E)$ available in the emitting electrode, and the probability they are able to quantum mechanically tunnel through the insulating barrier T(E). The Fermi distribution functions for metal 1 $f_1(E)$ and metal 2 $f_2(E)$ where the bias voltage is applied to metal 2 takes the form

$$f_1(E) = \frac{1}{\exp\left(\frac{E - E_f}{kT}\right) + 1} \qquad f_2(E) = \frac{1}{\exp\left(\frac{E - E_f + qV_{bias}}{kT}\right) + 1} \qquad (3.1.1a,b)$$

where E_f is the Fermi level within the metal, k is the Boltzmann constant, and T is the absolute temperature.

Mathematically we may express the current from metal 2 to metal 1 in the MIM diode as a function of voltage as

$$J_x = -q n \upsilon = -q n_2(E) \upsilon(E) T(E_x) \qquad (3.1.2)$$

where

$$n_2(E) = g_2(E)\, f_2(E) \tag{3.1.3}$$

I assume parabolic energy-momentum bands within the electrode and consequently use the effective mass approximation to calculate the three dimensional density of states (Pierret, 1989). The density of states has a square root dependence on energy (Kittel, 1986)

$$g(E) = \frac{4\pi\,(2m)^{\frac{3}{2}}}{h^3}\sqrt{E}\, dE \tag{3.1.4}$$

where m is the electron mass, and h is Planck's constant.

We convert the density of states expression from a function of velocity as in equation (3.1.2) to a function of kinetic energy by using

$$E = \tfrac{1}{2} m\upsilon^2 \quad \therefore \quad dE = m\upsilon\, d\upsilon \tag{3.1.5}$$

The substitution of equation (3.1.5) into equation (3.1.4) results in a density of states expression that is a function of carrier velocity.

$$g(\upsilon) = \frac{8\pi\, m^3}{h^3}\upsilon^2 d\upsilon \tag{3.1.6}$$

We must make the distinction between the carrier total velocity, as is in equation (3.1.6), and the component of velocity in the conduction direction x. Carriers that do not have a component of velocity in the x direction do not contribute to the current. The distinction in direction is made by transforming from spherical coordinates, used in the density of states, to Cartesian coordinates. In spherical coordinates, the density of states is a sphere that when combined with the Fermi function extends from the origin outward a radial distance equal to the Fermi velocity. Figure (3-2) pictorially illustrates the density of states sphere in Cartesian coordinates.

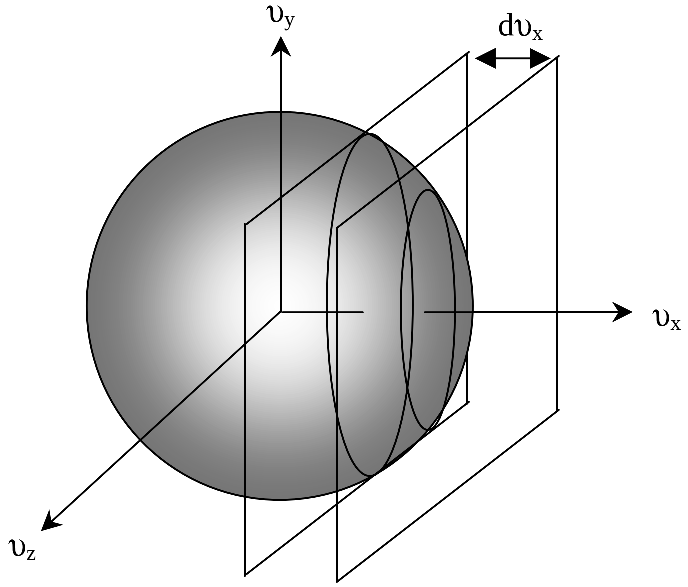

Fig. 3-2. *The spherical to Cartesian coordinate system relation for the density of states. In the current density calculation we are interested in calculating the number of carriers with components of velocity in the x direction between* υ_x *and* $\upsilon_x+d\upsilon_x$*. This corresponds to the portion of the density of states sphere contained between the two intersecting planes at* υ_x *and* $\upsilon_x+d\upsilon_x$*.*

In Figure (3-2), the spherical components are: Phi ϕ which originates from the x axis and rotates within the x-y plane, theta θ which originates from the z axis and rotates towards the x-y plane, and R which is the radial distance outward from the origin.

To calculate the density of states with velocities between υ_x and $\upsilon_x+d\upsilon_x$ we must calculate the volume of the sphere contained between the two intersecting plains at υ_x and $\upsilon_x+d\upsilon_x$. The Cartesian coordinate components are related to the spherical coordinates by the following trigonometric relations:

$$dx = R\sin(\theta)\,d\phi \qquad dy = R\,d\theta \qquad dz = dR \tag{3.1.7}$$

Combining the Cartesian coordinate components together a differential volume is formed.

$$dx\,dy\,dz = R^2\sin(\theta)\,d\phi\,d\theta\,dr \tag{3.1.8}$$

Integrating theta and phi over their entirety, from -π/2 to +π/2 and 0 to 2π respectively, we are left with a volume element containing only a radial velocity dependence.

$$dx\,dy\,dz = 4\pi R^2\,dr \quad \therefore \quad d\upsilon_x\,d\upsilon_y\,d\upsilon_z = 4\pi\upsilon_r{}^2\,d\upsilon_r \tag{3.1.9}$$

Substituting equation (3.1.9) into the velocity dependant density of states we convert the density of state into Cartesian coordinates.

$$g(\upsilon) = 2\frac{m^3}{h^3}\,d\upsilon_x\,d\upsilon_y\,d\upsilon_z \tag{3.1.10}$$

We still have components of velocity in the y and z directions that we would like to fold into the total energy. We do this by converting the dυ_x and dυ_y terms back into spherical coordinates with the use of equation (3.1.8).

$$d\upsilon_x \, d\upsilon_y = \upsilon_r \, d\theta \, d\upsilon_r \tag{3.1.11}$$

The differential in theta may then be removed by integrating from 0 to 2π. The differential in radial velocity is converted into radial (total) energy with the use of equation (3.1.5).

$$d\upsilon_y \, d\upsilon_z = \frac{2\pi}{m} dE \tag{3.1.12}$$

We combine equation (3.1.10) and equation (3.1.12) and multiply by the Fermi distribution function f(E) to write the expression for the carrier density as a function of velocity in the x direction.

$$n(\upsilon_x) = \frac{4\pi m^2}{h^3} \int f(E) \, dE \, d\upsilon_x \tag{3.1.13}$$

We have the necessary pieces to write the full expression for the current due to electron tunneling from metal 2 to metal 1 by substituting equation (3.1.13) into equation (3.1.2).

$$J_{2\to 1} = \int_{\upsilon_x} q\upsilon_x \frac{4\pi}{h^3} \int_E f_2(E) \, dE \, T(E_x) \, d\upsilon_x \tag{3.1.14}$$

As a final step we convert the x directed velocities into x directed energy using equation (3.1.5).

$$J_{2\to 1} = \frac{4\pi m_2 q}{h^3}\int_0^{\infty} T(E_x)\left[\int_{E_x}^{\infty} f_2(E)\,dE\right]dE_x \qquad (3.1.15)$$

The expression $J_{2\to1}$above represents the total current density flowing from metal 2 to metal 1. Using a similar procedure an expression is derived for the total current due to electron tunneling from metal 1 to metal 2.

$$J_{1\to 2} = \frac{4\pi m_1 q}{h^3}\int_0^{\infty} T(E_x)\left[\int_{E_x}^{\infty} f_1(E)\,dE\right]dE_x \qquad (3.1.16)$$

The total current in an MIM diode is simply a combination of current from metal 2 to metal 1 and the current from metal 1 to metal 2.

$$J_{Dark}(V) = J_{2\to 1} - J_{1\to 2} = \frac{4\pi m q}{h^3}\int_0^{\infty} T(E_x)\left[\int_{E_x}^{\infty} f_2(E-V) - f_1(E)\,dE\right]dE_x \qquad (3.1.17)$$

In $J_{Dark}(V)$ I have assumed the effective mass in metal 1 is equal to the effective mass in metal 2. This is the total expression for the un-illuminated, or dark, current density due to electron tunneling between two nearly free electron metals through an insulating barrier.

Inspecting the dark current density expression we make several observations about the MIM diode characteristics. First, notice that the current is controlled by the electron tunneling probability $T(E_x)$ which is a function of the potential barrier between the metals. As we shall see, the tunneling probability dominates the expression. Consequently, the precise shape of the barrier is of utmost importance in MIM diode design. Second, the only temperature dependence of the MIM diode current density results from the Fermi distribution function. In the next subsection, we will see that the tunneling probability does not introduce any temperature dependence. Finally, the density of states in the metal has a linear effect on the current density magnitude through the electron's mass within the metal.

ii. Electron Tunneling

The current expression for an MIM diode equation (3.1.17) is complete once the exact form of the electrons tunneling probability $T(E_x)$ is included. The probability of an electron tunneling through a barrier from metal 2 to metal 1 may be calculated using wave mechanics. We will find that the tunneling probability dominates the shape of the MIM diode J(V) curve.

The MIM diode current expression, equation (3.1.17), assumes a definite electron energy E_x and as a result we will be completely uncertain of the electron position. This uncertainty is contained in the plane wave form of the wave function Ψ.

$$\Psi = \exp\left(-ikx - \frac{iE_x t}{\hbar} \right) \tag{3.2.1}$$

For a particle, such as an electron, the uncertainty in position may be reduced by using a wave packet, or a summation of plane waves.

Boundary conditions must be imposed on the wave function throughout structure. The first boundary condition is that the magnitude of the wave function must be continuous. The second boundary condition requires that the derivative of the wave function, with the exception of delta function potentials, is continuous (Kroemer, 1994). Additionally, the electron momentum must be conserved in the tunneling transition.

The probability of finding an electron can be calculated from the wave function. Because the wave function is a plane wave, with no certainty in absolute position, we instead look at the relative magnitude of the wave function on each side of the barrier to determine tunneling probability. Specifically, the tunneling probability of an electron is defined as the square of the ratio between the magnitude of the forward traveling portion of the wave function within metal 2 to the magnitude of the forward traveling portion of the wave function within metal 1.

For simple barriers, such as the square barrier and triangular barrier, the tunneling probability may be solved analytically (Schiff, 1968). In a real MIM diode the barrier may not have a simple analytical form and the tunneling probability must be solved for numerically.

I numerically calculate the tunneling probability using a transfer matrix approach. For a single interface we can write the spatial wave function on both the left ψ_l and right ψ_r side of the interface as a summation of a forward and reverse traveling plane-waves.

$$\begin{aligned}\psi_l &= A\exp(i\,k_l\,x) + B\exp(-i\,k_l\,x)\\ \psi_r &= C\exp(ik_r\,x) + D\exp(-ik_r\,x)\end{aligned} \tag{3.2.2 a,b}$$

The time dependence of the wave function, $\exp(-iE_x t/\hbar)$, has been suppressed. The momentum $k_{l,r}$, as a result of the nearly free electron approximation, is defined as

$$k = \sqrt{\frac{2\,m\,q\,(E-V)}{\hbar^2}} \tag{3.2.3}$$

where ħ is Planck's constant divided by 2π and V is the potential energy (Kittel, 1986).

By imposing the boundary conditions that the wave function and its derivative are continuous at the interface we can derive a transfer matrix between the components of ψ_l and ψ_r.

$$\begin{bmatrix} A \\ B \end{bmatrix} = \begin{bmatrix} \dfrac{\exp\left(-i(k_l - k_r)x\right)(k_l + k_r)}{2k_l} & \dfrac{\exp\left(i(k_l + k_r)x\right)(k_l - k_r)}{2k_l} \\ \dfrac{\exp\left(i(k_l + k_r)x\right)(k_l - k_r)}{2k_l} & \dfrac{\exp\left(i(k_l - k_r)x\right)(k_l + k_r)}{2k_l} \end{bmatrix} \begin{bmatrix} C \\ D \end{bmatrix} \tag{3.2.4a}$$

$$\begin{bmatrix} A \\ B \end{bmatrix} = \begin{bmatrix} m_{11} & m_{12} \\ m_{21} & m_{22} \end{bmatrix} \begin{bmatrix} C \\ D \end{bmatrix} \tag{3.2.4b}$$

When the effective mass changes across an interface we must multiply the transfer matrix by the sqrt(k_l/k_r) to ensure tunneling probabilities do not exceed unity. Physically this is just conservation of momentum.

We next divide the barrier into a series of infinitesimally small sections and calculate the transfer matrix for each interface. The transmission of the total barrier may then be calculated by multiplying together all of the individual transfer matrices from each interface. From the total transfer matrix we calculate the tunneling probability of an electron with energy E_x. We assume that the wave function of the electron within the second metal, after tunneling through the barrier, has no reflected component and set the value of D in the complete transfer matrix equal to zero. As a result, the tunneling probability is simply the square of C/A, which is

$$T = \left(\frac{1}{m_{11}} \right)^2 \tag{3.2.5}$$

Inspecting the transfer matrix element m_{11} we find that the tunneling probability of an electron is temperature independent.

The transfer matrices contain the spatial form of wave function. Consequently we may calculate the wave function, or a wave packet, from the transfer matrices. For example, the Cr/Cr_2O_3/Pd MIM diode of Figure (3-1) is replotted in Figure (3-3). I divided the barrier into 600 sections and calculated the transfer matrices for an electron 2 eV above the Fermi level in the Cr metal (12 eV in the Figure) that is tunneling from the Cr electrode to the Pd electrode. I then plotted the wave function, both the real and imaginary components, of the 12 eV electron tunneling from the Cr electrode to the Pd electrode. The absolute magnitude of the wave function is irrelevant and is plotted on an arbitrary magnitude scale. The tunneling probability of this 12 eV electron is found from the relative magnitude of the wave function on each side of the barrier: T(12 eV)=0.064, and is equal for tunneling in either direction if we neglect scattering. If we include scattering, we must account for the fact that if the electron scatters within the oxide the field will have an influence and force the electron toward the Cr electrode.

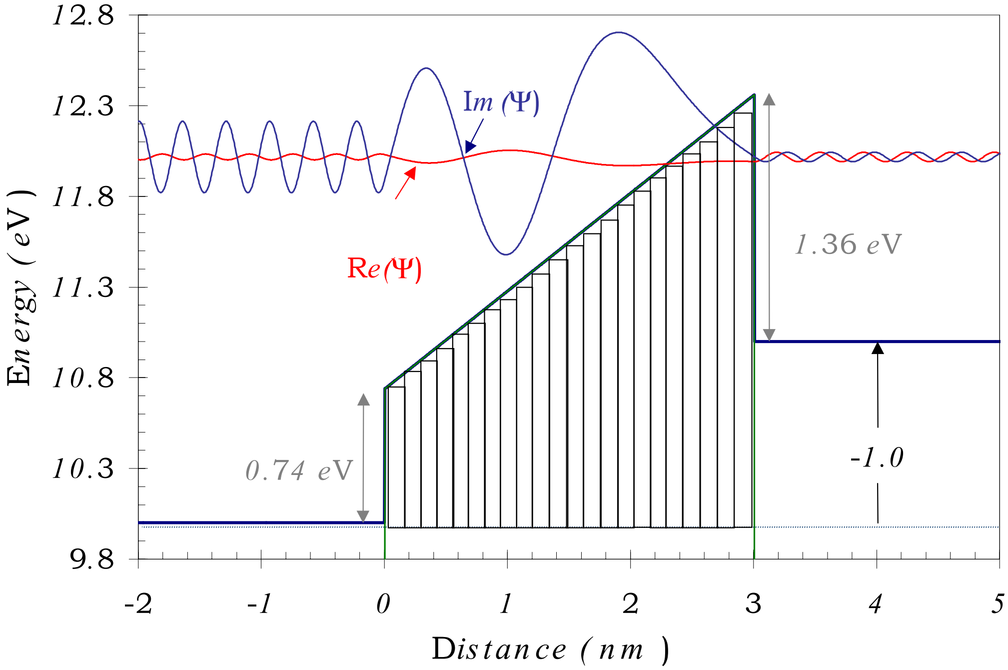

Fig. 3-3. *The wave function used to evaluate the transmission probability of a 12 eV electron tunneling from metal 1 to metal 2.*

After evaluating the tunneling probability for an electron of a single energy, we may repeat the process over a span of energies to calculate the electron tunneling probability as a function of energy. The complete T(E) is plotted in Figure (3-4).

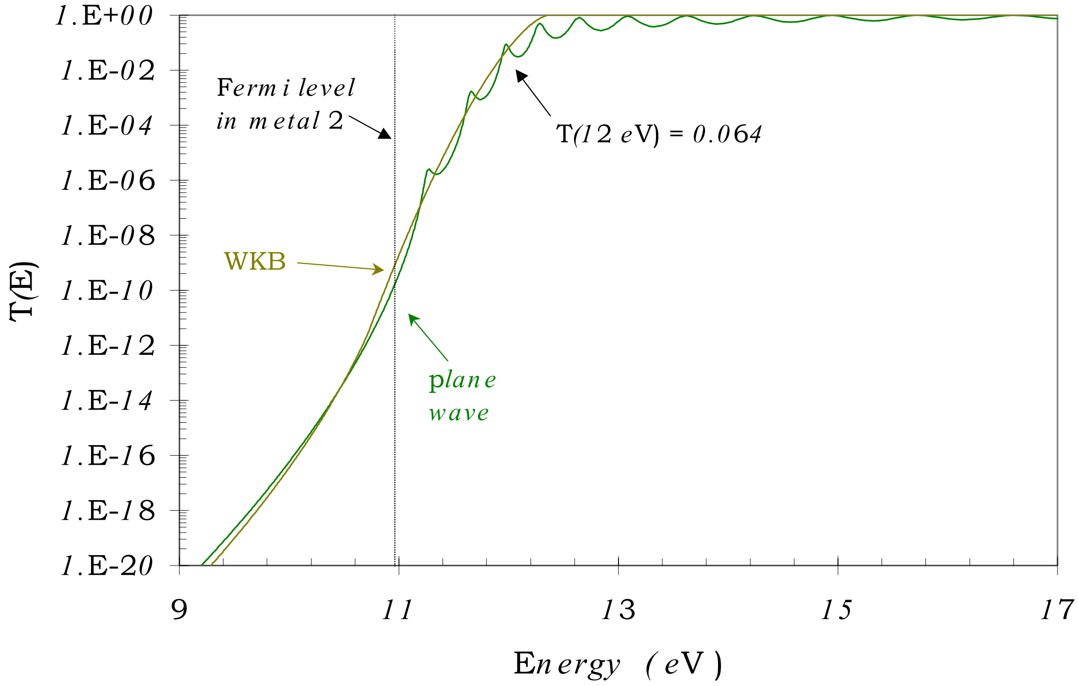

Fig. 3-4. *The tunneling probability as a function of energy for the 3 nm Cr/Cr$_2$O$_3$/Pd MIM diode with a negative applied bias of one volt. The plane wave solution, using transfer matrices, and the WKB solution are shown.*

In Figure (3-4) I have included the WKB approximation to the tunneling probability. The WKB approximation neglects the reflected wave within the barrier region to produce an analytical function for the T(E) in arbitrary barriers. Notice that at the Fermi level of metal 2, 11 eV, the WKB approximation results in a transmission probability value approximately 6 times larger than the plane wave solution. At energies above the Fermi level of metal 2 we find that the difference between the WKB and plane wave approximation becomes more noticeable in certain regions. Furthermore, notice that the transmission probability limits to unity in the WKB approximation for energies greater than the height of the barrier (12.36 eV) while in the plane wave solution oscillations due to reflections are present even at energies above the barrier height. The depth of the valleys in the T(E) are affected by the energy of the electron relative to the top of the barrier.

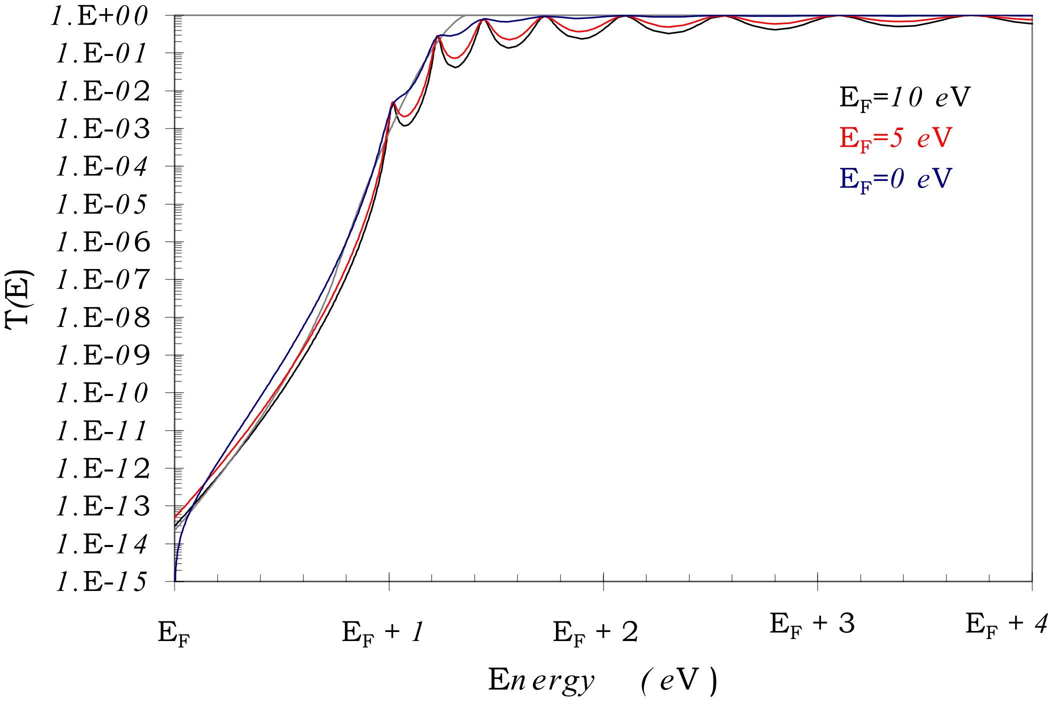

Fig. 3-5. *The tunneling probability as a function of energy for a Cr/Cr_2O_3/Pd MIM diode. The plot shows that the oscillation depth in the T(E) decreases as we decrease the Fermi level in the metal electrodes.*

The transfer matrix method for calculating the tunneling probability has several advantages. First, we are not limited to simple barrier shapes that have analytical solutions. We can numerically calculate both the spatial component of the wave function and the tunneling probability for any barrier shape. Second, we do not need to neglect reflections within the barrier as is done in the WKB approximation. This becomes particularly important if we would like to calculate coherent tunneling through a multilayer structure containing resonant energy levels. Third, we may extend this method to calculate the time dynamics of electron tunneling by forming a wave packet (a summation of plane waves) and calculating its temporal propagation through the structure at energies both above and below the maximum barrier height.

Simulating wave packets propagating through barriers produces entertaining movies. On the practical side these movies offer insight into the temporal dynamics of electrons tunneling through a barrier and through resonant energy levels. Wavepackets are formed are formed by a summation of planewaves over a range of electron energies and as a result tend to dampen the oscillations in the T(E) that are found in the single energy plane wave solution to tunneling.

iii. J(V) For The Cr/Cr_2O_3/Pd MIM Diode

We are now at the position to numerically calculate the full J(V) curve for an MIM diode using the current equation (3.1.17) developed in section 3.1 and the tunneling probability calculations of section 3.2. I assume the Fermi level in both metals is 10 eV and unity effective mass throughout the structure. The calculated |J(V)| curve for the Cr/Cr_2O_3/Pd MIM diode of Figure (3-1) is plotted on a logarithmic scale in Figure (3-6) where the calculated points are connected by straight lines.

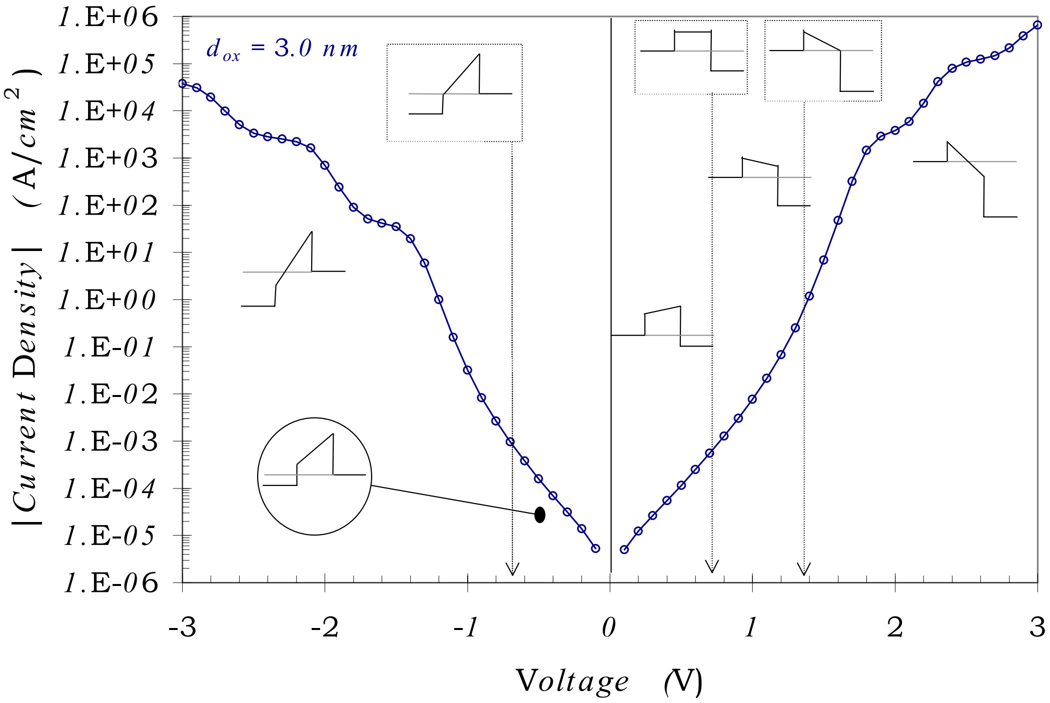

Fig. 3-6. *The simulated current density magnitude vs. voltage curve for a Cr/Cr_2O_3/Pd MIM diode with a 3 nm thick oxide. MIM diode band diagrams have been included at and between the various transition points. The band diagrams within boxes are for a particular applied voltage, while the other band diagrams are for the indicated regions between.*

The oscillations in the current magnitude as a function of voltage evident in the J(V) curve are a result of the oscillations in the T(E) curve. The physical cause of these oscillations is quantum mechanical interference due to the reflections of the tunneling electron within the barrier. In my measured MIM diodes of section II these oscillations are not evident. The damping of the oscillations in the T(E) result from fluctuations in oxide thickness, scattering events that break the coherence of the electron, and the uncertainty in the electron energy.

The current vs voltage curve shows several distinct regions that may be correlated with the shape of the band diagram. The band diagrams of the MIM diode have been superimposed on the J(V) curve at and between the important transition regions. With low applied biases (< 0.74 V) of either polarity, direct tunneling of the electron through the entire width of the oxide limits the current magnitude. Note however, that under negative applied bias the tunneling is occurring in a direction opposing the internal electric field while under positive bias tunneling is occurring in the same direction as the electric field. If a collision were to occur in the tunneling process the electric field direction would play a role and alter the asymmetry. However, since I am neglecting scattering, the electric field direction affects only the manner in which the band shape changes with increasing bias voltage. As we increase the bias voltage beyond the first transition point, 0.74 V, the negative voltage band diagram enters into the Fowler-Nordheim tunneling regime where the electron tunnels through only a fraction of the oxide width (Fowler, 1928). The band under positive bias reaches a point of zero electric field in the oxide at +0.74 volts and subsequently continues direct tunneling, only this time in a direction opposing the electric field direction. As we continue increasing the bias voltage in the positive direction we reach the second transition point, +1.36 V, where the electrons enter the Fowler-Nordheim tunneling regime. Under reverse bias, this is not a transition point and Fowler-Nordheim tunneling continues. Once we apply sufficiently high negative biases, the 1.36 eV Cr_2O_3–Pd barrier and the number of electrons available to tunnel will limit the current magnitude. Under large positive biases the 0.74 eV Cr-Cr_2O_3 barrier and the number of electrons available to tunnel will limit the current magnitude. Since we have assumed the densities of states and Fermi levels of the two metals are equal, any differences in the maximum current magnitude in forward and reverse bias will be due to differences in the barrier heights. Consequently, we find higher current magnitudes under large positive bias, where the smaller barrier limits the current, than under large negative bias.

iv. Rectification Reversal

The ratio of the magnitude of the current produced under forward bias to that produced under reverse bias varies as a function of applied voltage for an asymmetric MIM diode structure. We define forward bias to be that bias voltage polarity which produces the higher current for large-magnitude bias voltages. The Cr/Cr_2O_3/Pd MIM diode of Figure (3-5) produces a higher magnitude current under high positive biases than under equivalent negative biases, and consequently is defined as being forward biased when a positive voltage is applied to the top Pd metal.

Rectification reversal occurs at voltages where the higher current is produced under reverse bias. For a trapezoidal barrier the polarity of the bias that produces the higher tunneling probability varies with the magnitude of the applied voltage. Thus, replotting the data of Figure (3-7) using the absolute value of voltage we clearly see a rectification reversal that occurs in the J(V) curve of the Cr/Cr_2O_3/Pd MIM diode.

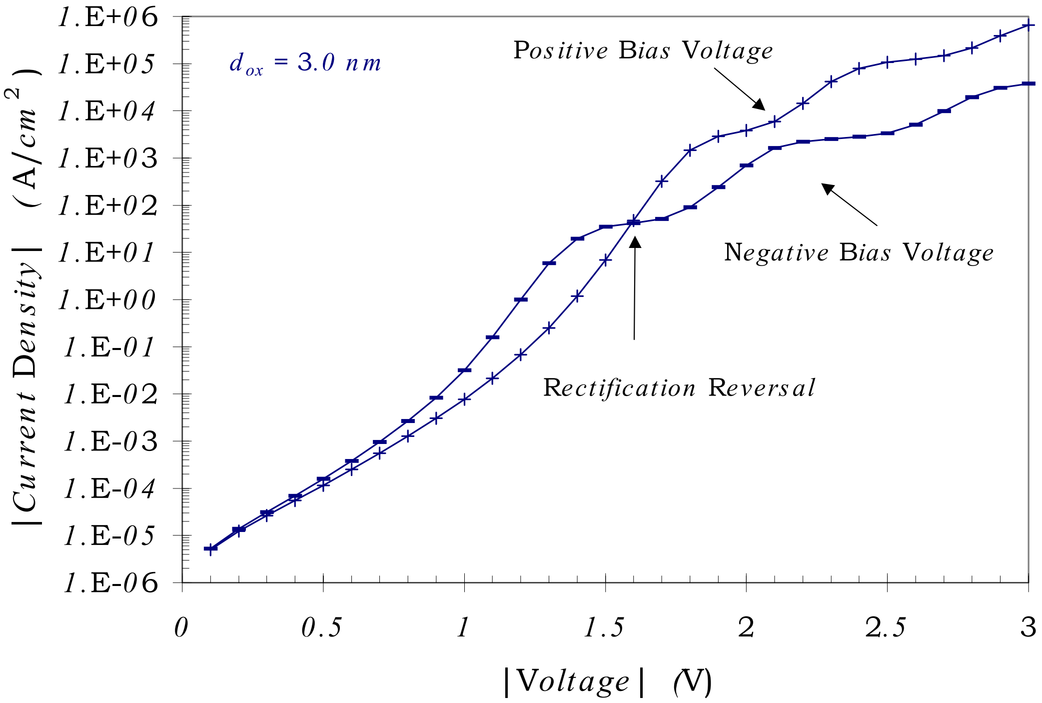

Fig. 3-7. *Theoretical calculation of the absolute value of current vs. the absolute value of voltage for a Cr/Cr_2O_3/Pd MIM diode. Rectification reversal occurs at approximately 1.6 volts.*

Rectification reversal may be understood in terms of the electron tunneling probability. The WKB approximation to the electron tunneling allows us to illustrate the physical cause of rectification reversal. The WKB approximation is

$$T_{WKB}(E) = \exp\left[-2\int |k(x)|\,dx\right] \qquad k(x) = \sqrt{\frac{2m_0\,(E_c(x) - E_{electron})}{(h/2\pi)^2}} \qquad (3.4.1)$$

where E_c is the energy of the conduction band within the oxide and $E_{electron}$ is the energy of the tunneling electron (Griffiths,1995). The tunneling probability is a function of the integral of $(E_c\text{-}E_{electron})^{1/2}$ over the fraction of the oxide through which the electron tunnels, where the energy of the conduction band E_c is greater than the energy of the tunneling electron $E_{electron}$ and subsequently the momentum k(x) is real. The integral of the $(E_c\text{-}E_{electron})^{½}$ term is responsible for rectification reversal. Direct tunneling is when the electron must tunnel through the entire width of the potential barrier, which occurs for low voltages. Fowler-Nordheim tunneling occurs when the electron tunnels through only a fraction of the oxide's full width, at higher forward biases because E_c is less than $E_{electron}$ over part of the barrier width. Physically, rectification reversal is due to the transition between the direct tunneling and the Fowler-Nordheim tunneling regimes occurring at different magnitudes of bias voltage in forward and reverse bias, resulting from dissimilar barrier heights at the two metal-oxide interfaces.

In addition to adjusting the reversal point by changing the barrier heights, we can also control the voltage location of the reversal point by adjusting the oxide thickness. I have illustrated this point by calculating the current vs. voltage curve for the Cr-Cr_2O_3-Pd MIM diode using various oxide thickness' and plotted the results in Figure (3-8).

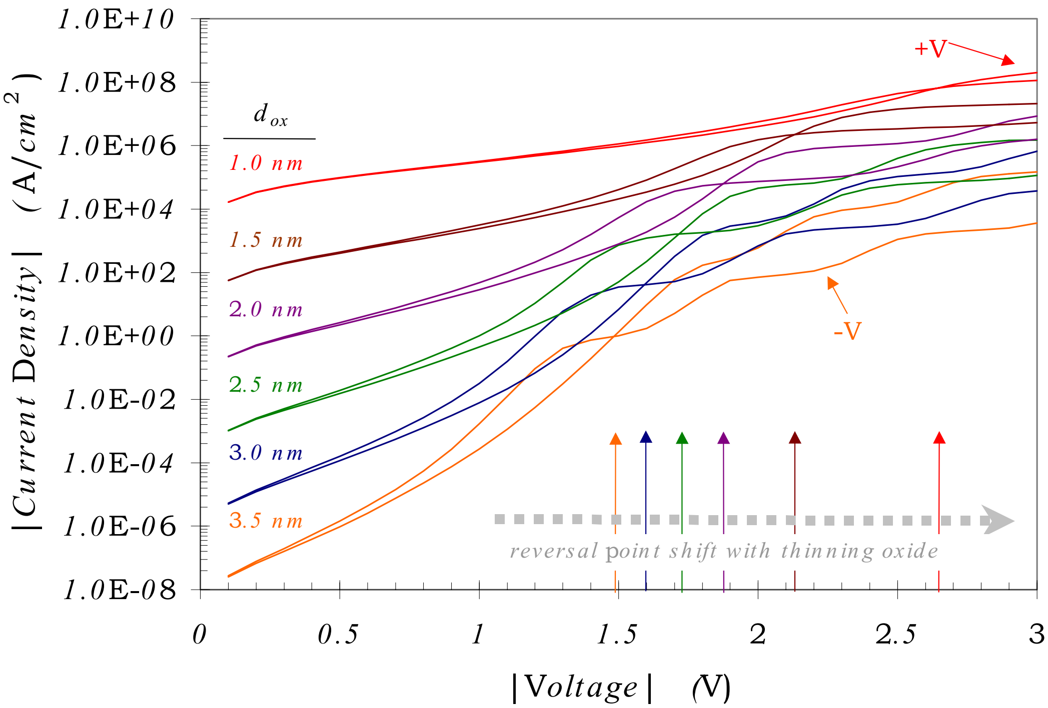

Fig. 3-8. *The simulated current density magnitude vs. absolute voltage curves for Cr/Cr_2O_3/Pd MIM diodes with various oxide thicknesses. The figure illustrates the shift in the rectification reversal point to larger voltages as the oxide is made thinner.*

As we decrease the thickness of the oxide layer the reversal point shifts to higher voltages as the MIM diode conduction becomes dominated by direct tunneling. In some MIM diode applications it may be possible, by judicious choice of the oxide thickness, to shift the rectification reversal point out of the diode's operating range.

I next investigate the effects of changing the barriers in a 3 nm thick Cr/Cr_2O_3/Pd MIM diode. Figure (3-9) shows the effects of increasing and decreasing the work function of the base Cr metal by 0.1 eV.

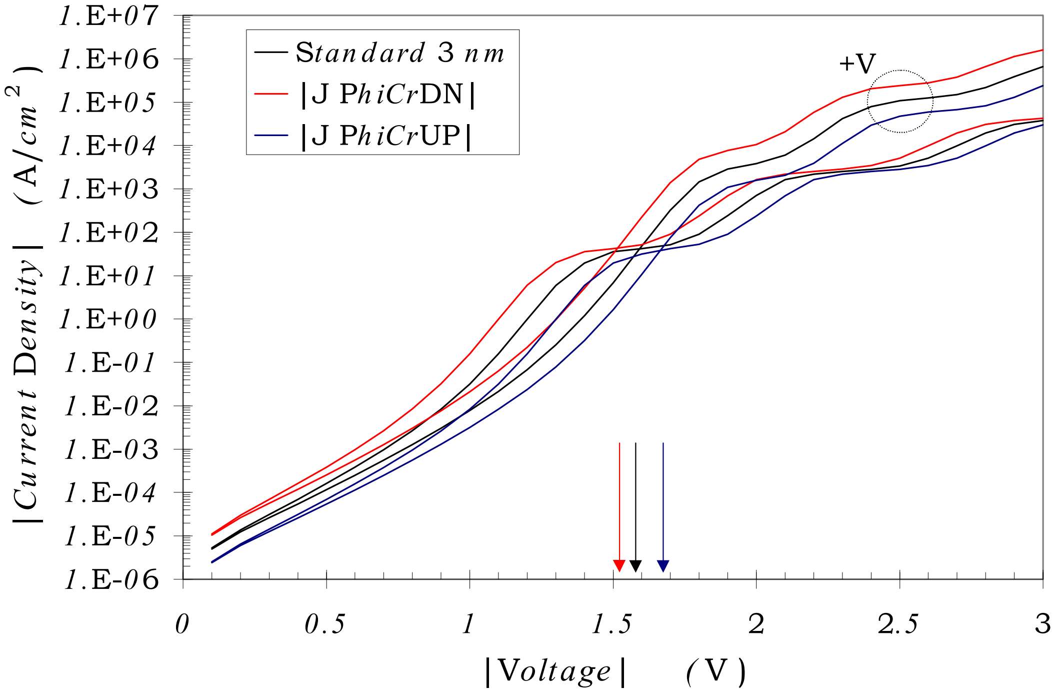

Fig. 3-9. *Current vs voltage for a Cr/Cr$_2$O$_3$/Pd MIM diode with a 3 nm thick oxide. The black trace is the standard MIM diode. The red trace has the work function of the Cr decreased by 0.1 eV and in the blue trace it is increased by 0.1 eV.*

Decreasing the work function of the Cr metal increases the current magnitude, which is expected since we are decreasing the left barrier between the Cr and its native oxide. This also shifts the reversal point in toward lower voltages.

Figure (3-10) shows the effects of increasing and decreasing the work function of the top Pd metal by 0.1 eV.

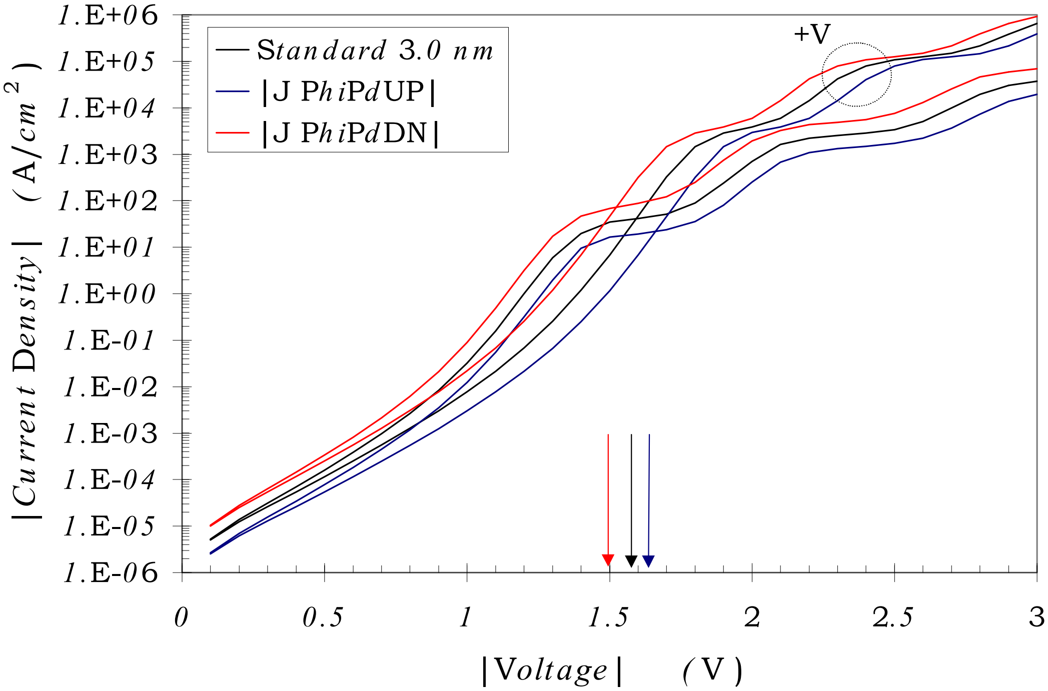

Fig. 3-10. *Current vs voltage for a Cr/Cr_2O_3/Pd MIM diode with a 3 nm thick oxide. The black trace is the standard MIM diode. The red trace has the work function of the Pd decreased by 0.1 eV and in the blue trace it is increased by 0.1 eV.*

Decreasing the work function of the Pd metal increases the current magnitude, which is expected since we are decreasing the right barrier between the Pd and the Cr_2O_3. This also shifts the reversal point in toward lower voltages.

Figure (3-11) shows the effects of increasing and decreasing the electron affinity of the Cr_2O_3 by 0.1 eV.

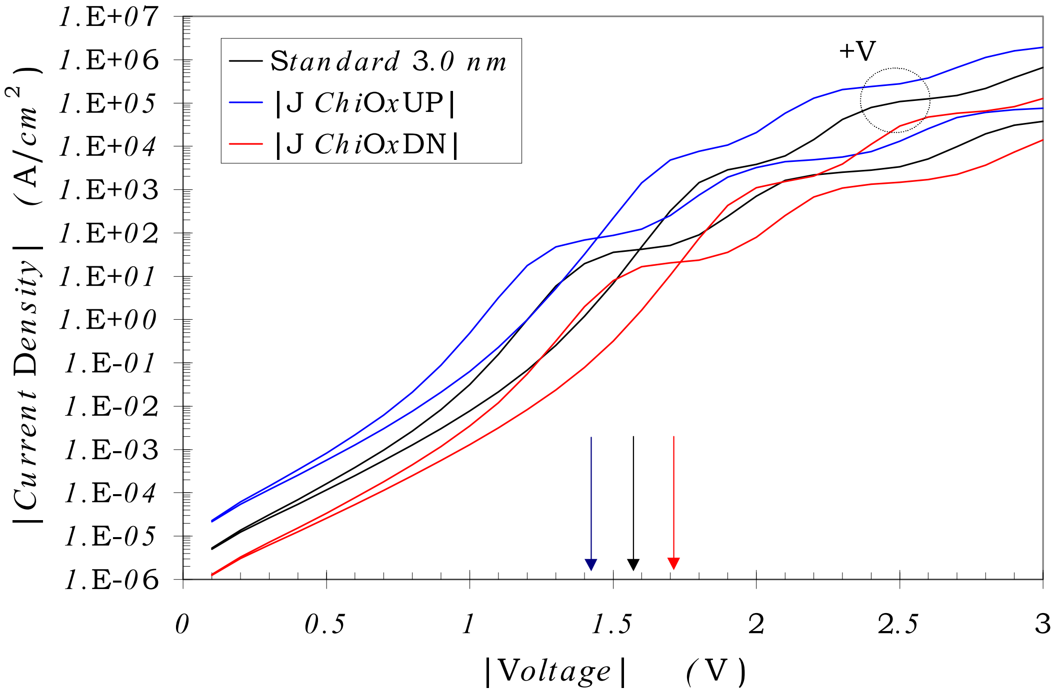

Fig. 3-11. *Current vs voltage for a Cr/Cr$_2$O$_3$/Pd MIM diode with a 3 nm thick oxide. The black trace is the standard MIM diode. The red trace has the electron affinity of the Cr$_2$O$_3$ decreased by 0.1 eV and in the blue trace it is increased by 0.1 eV.*

Increasing the electron affinity of the oxide increases the current magnitude which is expected, since we are decreasing both barriers in this case. Increasing the electron affinity of the oxide by 0.1 eV is the same as decreasing the work functions of both metals by 0.1 eV. This shifts the reversal point in toward lower voltages.

Finally, Figure (3-12) shows the effect of decreasing the electron mass in the oxide from unity to 0.5.

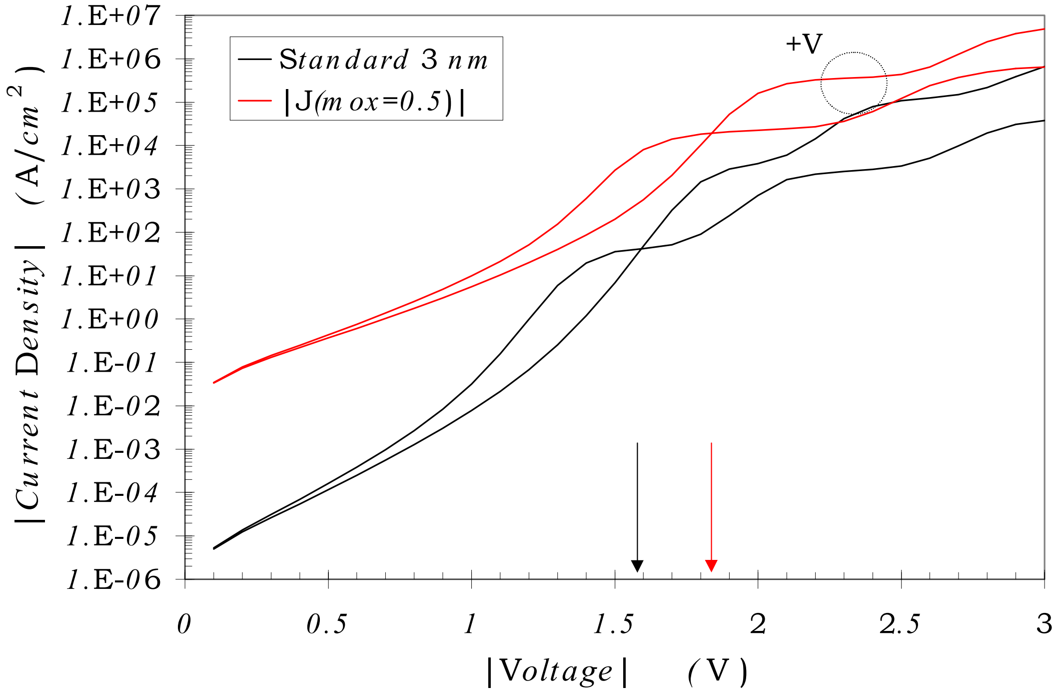

Fig. 3-12. *Current vs voltage for a Cr/Cr_2O_3/Pd MIM diode with a 3 nm thick oxide. The black trace is the standard MIM diode. The red trace has the effective mass of the electron in the oxide decreased from unity to 0.5.*

Decreasing the effective mass results in a larger electron tunneling probability. Consequently, the current magnitude increases with decreasing effective mass and the reversal point shifts inward to lower voltages.

v. Deviations From The Ideal Barrier

The shape of the energy barrier in an MIM diode was discussed in Section I. We found that the shape of the barrier was determined by the magnitude of the metal-insulator barrier height at each interface. The metal-insulator barrier height is ideally determined by the difference between the work function of the metal and the electron affinity of the insulator. Any deviation in the barrier shape will alter the electron tunneling probability and subsequently the resultant J(V) curve. In this subsection I briefly mention the main barrier altering effects and their consequences.

The rectification reversal point in the J(V) curve will be altered if appreciable field penetration into the electrodes is present. If the field penetration is different in the two metal electrodes the asymmetry will also be affected (Simmons, 1967). I have neglected the field penetration in this work.

Image Force

The image force may play a significant role in altering the ideal barrier shape by effectively lowering the barrier height as seen by a tunneling electron. The image force is the result of a redistribution of the electrons within the metal due to a point charge within the barrier. Classically the potential due to the image force can be written as follows for an MIM diode (Simmons,1963)

$$V_{image} = -\frac{q^2}{4\pi\,\varepsilon\,\varepsilon_o}\left[\frac{x}{2} + \sum_{n=1}^{\infty}\left(\frac{n\,d_{ox}}{(n\,d_{ox})^2 - x^2} - \frac{1}{n\,d_{ox}}\right)\right] \qquad (3.5.1)$$

where d_{ox} is the thickness of the insulator, x is the point particle distance from the metal-insulator interface, and ε is the permitivity of the insulator. The optical permitivity is used due to the short time associated with the passage of the electron from the metal.

The classical form of the image force is often used within the scientific literature to account for barrier heights extracted from experiments measuring the optical emission of electrons from a metal into vacuum. As we will see, it is inappropriate to use the classical image force in most un-illuminated (or low temperature) tunneling experiments.

The more accurate technique for calculating the image force is using quantum mechanics. The quantum mechanical formulation takes into consideration that the electron is not a classical point charge within the insulator and that there is a finite probability of finding the electron within the barrier region.

Quantum mechanically, the image force takes on the following form (Weinberg, 1978).

$$V_{image} = -\int_{-\infty}^{0} \frac{q^2 \left| \Psi(-r',t) \right|^2}{2\varepsilon (r - r')} dr' \quad = \quad -\int_{0}^{\infty} \frac{q^2 \left| \Psi(r',t) \right|^2}{2\varepsilon (r + r')} dr' \tag{3.5.2}$$

In equation (3.4.2) that the magnitude of the image force is a function of the wave function (a wave packet for an electron). The wave function in turn is a function of the barrier shape which is altered from the ideal case by the image force. Consequently the problem must be solved numerically in an iterative self-consistent fashion.

By approximating the wave function of the electron as a delta function, Weinberg showed that the quantum mechanical image force is simply a scaling of the classical image force by the electron tunneling probability. The approximation of the electron wave packet as a delta function is acceptable if we assume that the wave packet is not significantly dispersed by the barrier during the tunneling process.

The magnitude of the image force varies depending upon the energy of the electron. We can generalize the effect of the image force as being classical for carriers well above the conduction band of the insulator where the electron tunneling probability is near unity and negligible for carriers well below the conduction band of the insulator. In the intermediate regions, the image force is somewhere between the classical result and being negligible.

In the simulations including the image force, I use the classical result and scale it by $T(E_x)$. In these cases it is necessary to iterate to a self-consistent solution at each energy level, between the $T(E_x)$ value and the barrier height due to the image force. Including the image force in the un-illuminated current density vs voltage for the Cr-Cr_2O_3-Pd MIM diode in Figure (3.5) does not produce a noticeable effect. This is because in an MIM diode most of the carriers contributing to the current are located near the Fermi level and the barrier is typically several kT above the Fermi level, resulting in a relatively small $T(E_f)$ value. Consequently the probability of an image particle in the barrier region is small and thus so is the image force effect. In my simulations, unless noted otherwise, I have neglected the image force.

Surface States

Surface states alter the barrier height at the metal-insulator interface (Bardeen, 1947). Surface states are typically due to contamination of the metal or insulator during fabrication or the chemical structure of the surface. Any deviation in the barrier heights found experimentally, are most likely due to these surface states and a clean fabrication process should minimize their effect. Any deviations that result between theory and experiment that can be accounted for by simply adjusting a barrier height are attributed to surface states.

Pinholes

Pinholes in the oxide will introduce a second conduction mechanism in parallel with the tunneling current. Pinhole conduction is generally orders of magnitude larger than the tunneling currents. In addition, pinhole conduction can be isolated from tunneling conduction by the different temperature dependencies. Pinhole formation is most likely due to the oxidation process. Any deviations between theory and experiment that can not be accounted for by tunneling conduction are attributed to pinholes.

Traps

Traps within the insulator may result in an increased current density in MIM diodes (Penley, 1962). This is due to the increased tunneling probability through the electron traps. Trapping time would be expected to limit the response time of the MIM diode incorporating trap assisted conduction. However, if the traps hold charge the current will be decreased due to the space-charge (Geppert, 1962).

Effective Mass

The effective mass within the oxide is inseparable from the barrier height in its effect on the tunneling probability. The effective mass in the metals also plays a role in the density of states. Because the effective mass of the oxide cannot be isolated from the barrier height I have simply assumed a unity effective mass throughout the structure. This is a common assumption.

The single value effective mass is only valid near the band edges and will effect the magnitude and shape of the MIM diode I(V) curve. For electron tunneling away from the band edge a Franz and Kane type of two-band model is more appropriate (Gundlach, 1973). In this model two parabolic effective masses, one from the conduction band and one from the valence band, are combined to form the effective mass.

Ionic Space Charge

Ionic space charge may be present in many forms and is neglected in our ideal MIM diode. Interface dipoles, ionic defects, traps, metal ions in the insulator, electronic space charge, etc., all alter the dominant conduction mechanisms through the oxide barrier. Positive ions incorporated into the barrier result in an increase in current (Schmidlin, 1966). Qualitative shape, temperature, and temporal dependencies separate these mechanisms from ideal tunneling.

Hot-Electron Tunneling Damage

The tunneling of hot electrons through the oxide can result in damage to the oxide-silicon interface at the receiving electrode (Vogel, 2000). The tunneling hot-electrons introduce trap states that allow for electron trapping and charging of the device.

vi. Simulation

During the course of this thesis work a significant portion of extra time and effort was committed to developing simulations to accurately calculate the MIM diode's J(V) curve. This simulation, MIMSIM, has been written and subsequently improved and mutated through many forms.

The fundamental structure of the simulation has remained consistent. MIMSIM evaluates the MIM diode current density equation (3.1.17) and the T(E). The numerical calculation is facilitated by a two dimensional grid of fixed step sizes in energy and distance to define the MIM diode.

The first simulations were calculations made within an Excel 97 spreadsheet incorporating custom Visual Basic routines (Microsoft, 2001). Three techniques were used for calculating the T(E) : the WKB approximation, solving the Schröedinger wave equation by placing the MIM diode in an infinite square well, and the plane wave transfer matrix approach discussed in section ii. The WKB approximation to the tunneling probability, as I have shown, neglects the reflections of the electron wave. Placing the MIM diode within an infinite well resulted in T(E) values that were strongly dependent on the width of the well used. The complex numbers and transfer matrices, though producing reliable results, took too long to calculate within Excel.

A subsequent MIM diode simulation was written in Mathematica 3.0 (Wolfram, 2001). Mathematica offered the capability to easily incorporate flexible point densities, multilayer structures, and use of its computational engine that was superior to Excel in handling complex matrices. However, this ease of programming still retained computational overhead and the calculations, though performed with ease and flexibility, were quite slow.

I next wrote a Matlab 5.3 port of the Mathematica code (Mathworks, 2001). Matlab, unlike Mathematica, is fully numerical, and I had hoped this would decrease the computational system overhead and subsequently speed up the simulation. Unfortunately, Matlab was not significantly faster than Mathematica and further developments under the Matlab platform were abandoned.

It became clear that in order to remove the overhead inherent with these software packages it would be necessary to write a freestanding compiled version of MIMSIM. I chose to write a DOS version using Borland C++ 5.0 (Borland, 2001). The C version of MIMSIM was written specifically to handle a single insulator MIM diode, thus losing some of the flexibility I had incorporated into the Mathematica version.

Many of the mathematical function conveniences provided by Mathematica and Matlab are not present in the standard C libraries so I needed to write several mathematical functions. I first wrote code to provide a structure for complex numbers (Numerical, 1992). I then added routines to perform addition, subtraction, multiplication, division, absolute values, square roots, exponents, and conjugates of these complex numbers.

The simulation parameters were stored in two-dimensional dynamic data structures and thus I wrote routines to both create, clear, print and destroy these dynamic data structures. In order to calculate transmission matrices, I needed to be able to calculate using complex matrices. This was a simple extrapolation of the two-dimensional dynamic data structures incorporating the complex data structure as the matrix elements. In addition to the routines to create, clear, print and destroy these complex dynamic data structures I wrote a routine to perform matrix multiplication on them.

Upon completion, the version of the MIMSIM written in C was orders of magnitude faster than any of the previous incarnations of MIMSIM. However, with this speed came the requirement that great care must be taken to ensure accurate evaluation of the integrals. I used box integration with fixed step widths. Given the nature of the MIM diode current calculation, we are often dealing with numbers on the order of 10^{+22} multiplied by numbers on the order of 10^{-34}. This introduces the potential for numerical errors and care was required to make sure they did not surface and affect the end result. To a great extent these problems could be controlled by careful choice in the order that equations were evaluated.

I subsequently made one final port of the code, from DOS to the Windows 98 operating system. This final version of MIMSIM was written with Borland C++ Builder 5.0 in a combination of C and C++. This version was written with the primary purpose to ease my repeated interactions with MIMSIM via a graphical user interface. Furthermore, using spreadsheet and database techniques the multilayer capabilities in Mathematica were reintroduced. The Windows 98 version of MIMSIM could simulate any multilayer structure of metals and insulators sandwiched between two metal contacts. The simulation uses the transfer matrix technique to calculate the T(E) for the MIM diode. Furthermore, it is capable of including the quantum mechanical image force, calculating the wave-function of an electron in the MIM diode, and the time dependent traversal of a wave packet through the MIM diode (or multilayer) structure. A screen shot of the MIMSIM 3.0 is shown in Figure (3-13).

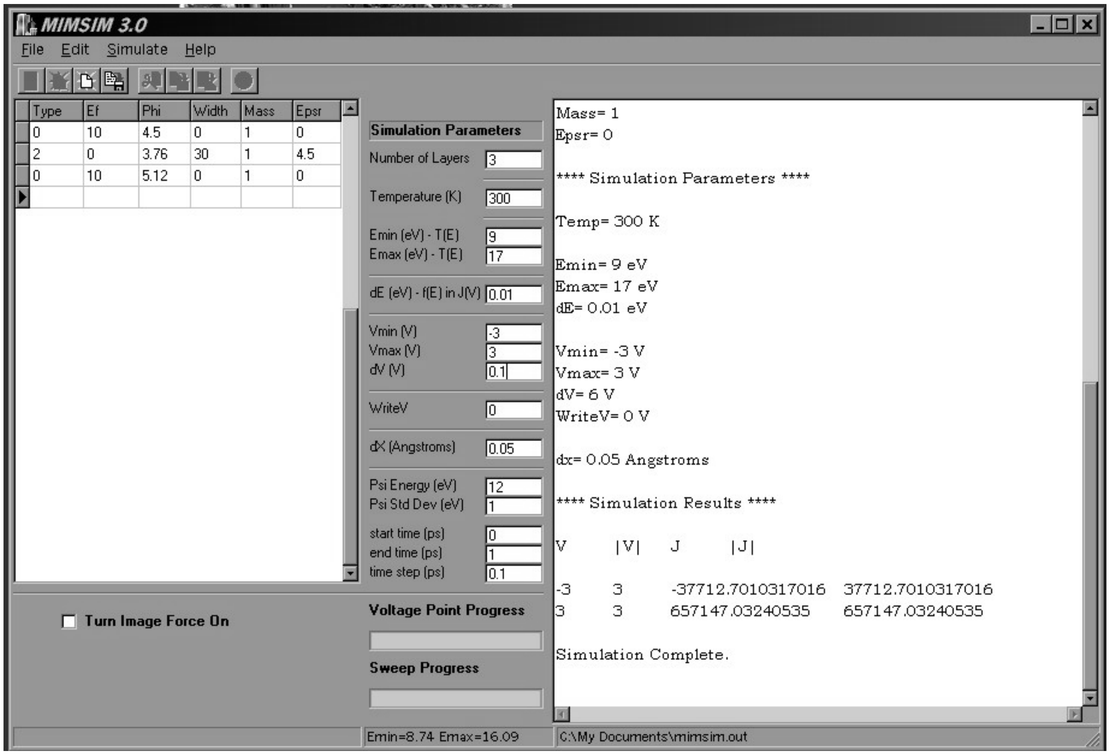

Type	Ef	Phi	Width	Mass	Epsr
0	10	4.5	0	1	0
2	0	3.76	30	1	4.5
0	10	5.12	0	1	0

Number of Layers: 3
Temperature (K): 300
Emin (eV) - T(E): 9
Emax (eV) - T(E): 17
dE (eV) - f(E) in J(V): 0.01
Vmin (V): -3
Vmax (V): 3
dV (V): 0.1
WriteV: 0
dX (Angstroms): 0.05
Psi Energy (eV): 12
Psi Std Dev (eV): 1
start time (ps): 0
end time (ps): 1
time step (ps): 0.1

☐ Turn Image Force On

```
Mass= 1
Epsr= 0

**** Simulation Parameters ****

Temp= 300 K

Emin= 9 eV
Emax= 17 eV
dE= 0.01 eV

Vmin= -3 V
Vmax= 3 V
dV= 6 V
WriteV= 0 V

dx= 0.05 Angstroms

**** Simulation Results ****

V       |V|     J          |J|

-3      3       -37712.7010317016   37712.7010317016
3       3       657147.03240535     657147.03240535

Simulation Complete.
```

Emin=8.74 Emax=16.09

C:\My Documents\mimsim.out

Fig. 3-13. *A screenshot of MIMSIM 3.0. The parameters for the Cr/Cr$_2$O$_3$/Pd MIM diode have been entered into the spreadsheet on the left portion of the screen. The central region are the various user entered simulation parameters. The two yellow bars display the status of the calculation during execution and the output file is displayed on the right side of the screen. The various simulation functions that may be performed are chosen from the "Simulate" menu.*

Even with a compiled version of the code, simulation times became unmanageable as the required point density in energy required to accurately evaluate the integrals increased. Certain structures, particularly those with resonant tunneling, require energy steps as small as 10^{-8} eV to accurately simulate the device. The small increments of energy resulted in extremely large grids due to the fixed increments of energy used and consequently dramatically increased the computation time. The solution was to remove the fixed energy step size and integration. I modified MIMSIM to dynamically choose a minimum integration range for each applied bias point and choose as large of energy step size as possible for each increment through the integration range. Trapezoidal integration techniques were used. The implementation of dynamic step sizes and integration ranges made structures, which with previous versions could not be accurately simulated within my lifetime, solvable overnight.

Additionally, the nested integral of equation (3.1.17), can be reduced to a single integral if sufficiently high precision numerical evaluations are used. This is possible since we know that the integral of $f_1(E)-f_2(E-V)$ from zero to infinity is equal to V. Consequently, instead of evaluating the integral each time, we can simply keep a running total of the integral from 0 to E_x and subtract this from the known total V. If sufficiently accurate numerical evaluations are not used, this method will not approach zero and an error will be introduced. I found that the computation time required to evaluate the integral was less than the time required to carry out the answer to a acceptable number of digits and so I did not implement this trick.

vii. Simulation vs Theory

In section II we looked at a few of the MIM diodes I have fabricated and measured. The comparison between theory and experiment agreed well qualitatively. The best quantitative fit was with the Al/Al_2O_3/Ag system in Figure (3-14). Using literature values for the metal work functions (see Appendix II) and the 2.1 nm oxide thickness extracted from capacitance measurements, I found the comparison between the simulation and experimental diode agree quite well in magnitude and curvature (by adjusting material parameters form their nominal values a precise fit is attainable).

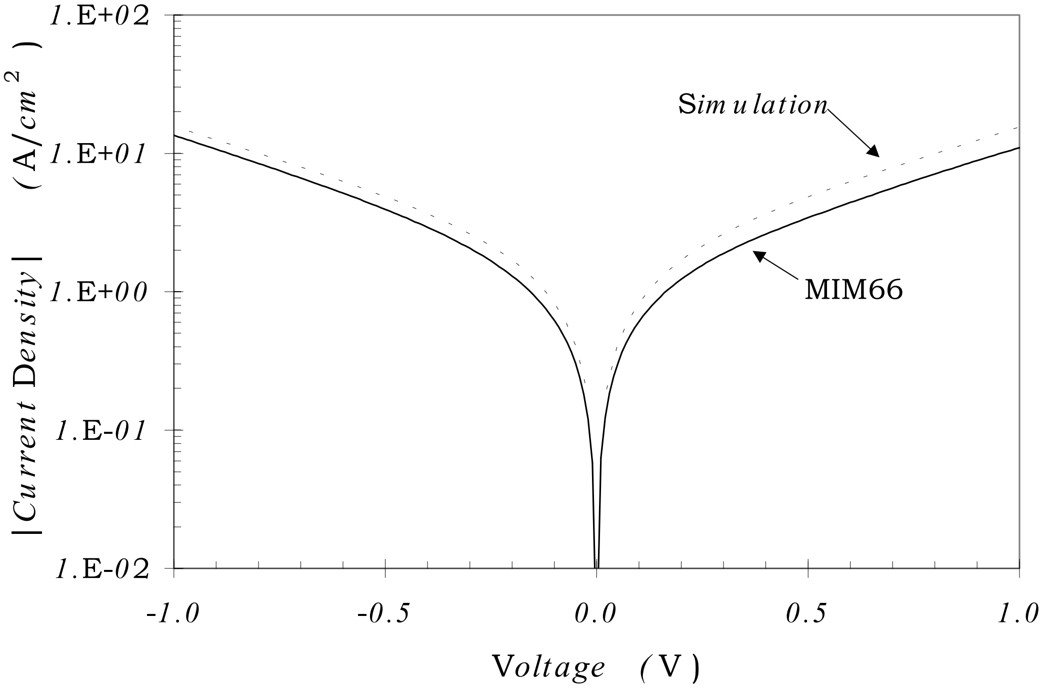

Fig. 3-14. *Experimental current density vs voltage curve for MIM diode 66 made from Al/Al_2O_3/Ag (solid line) and the theoretical calculation (dashed line).*

Quantitative fit with the niobium material system was not obtained. Current magnitudes predicted theoretically, at the maximum applied voltage, were orders of magnitude larger than the experimental results. Qualitatively the shape of the experimental data fit the theoretical predictions.

For the chromium MIM diodes, the current magnitudes predicted by theory were reasonably close to the experimentally obtained values. The curvature of the I(V) curves did not match the experimental data well. A chromium MIM diode (162) with a palladium top contact $Cr/Cr_2O_3/Pd$ is shown in Figure (3-15). The oxide thickness of MIM162 was estimated to be 1.7 nm from capacitance measurements assuming a dielectric constant of 10. The asymmetry, larger currents for negative applied bias, predicted from theory is present in the experimental data.

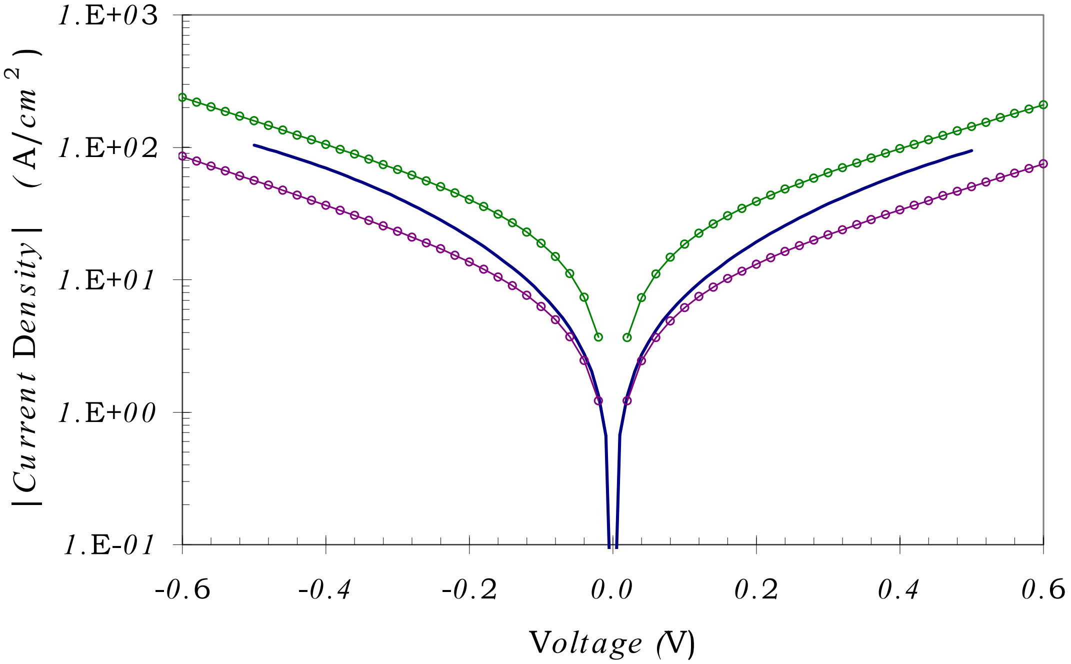

Fig. 3-15. *Experimental current density vs voltage curve for MIM diode 162, Cr/Cr$_2$O$_3$/Pd (thick solid line) and the theoretical calculations (circles) for a 1.6 nm (upper curve) and 1.7 nm (lower curve) oxide.*

Similar agreement was found for the symmetric Cr/Cr$_2$O$_3$/Cr MIM diode 161, shown in Figure (3-16).

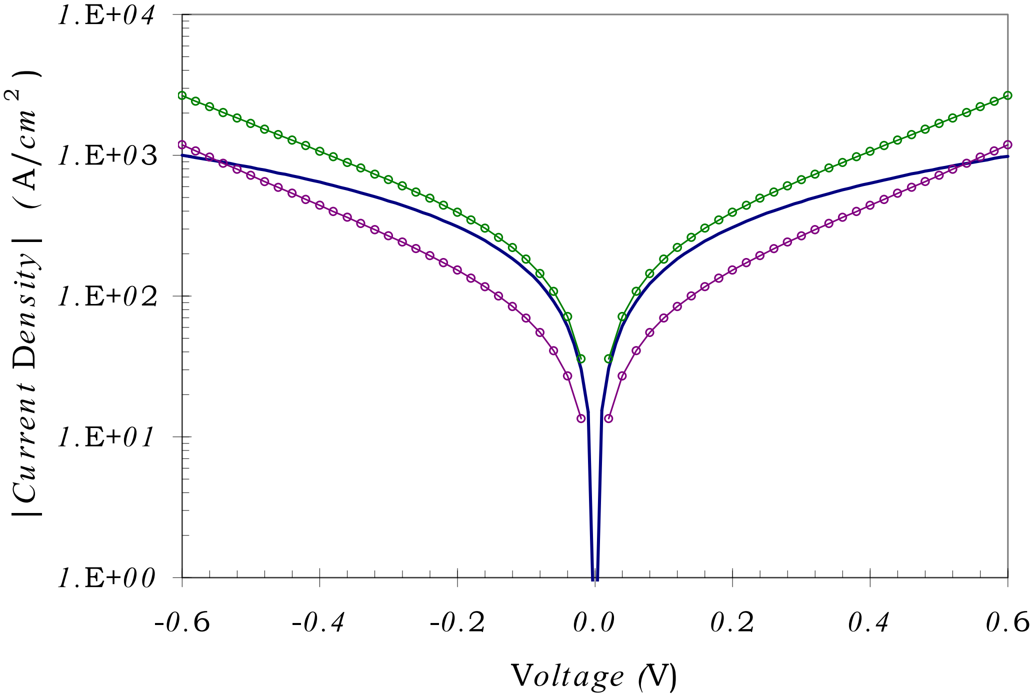

Fig. 3-16. *Experimental current density vs voltage curve for symmetric chromium Cr/Cr_2O_3/Cr MIM diode 161 (thick solid line) and the theoretical calculations (circles) for a 1.7 nm (lower curve) and 1.6 nm (upper curve) oxide.*

The current vs voltage curve is expected to show no asymmetry between positive and negative applied biases with current magnitudes approximately an order of magnitude higher than MIM162 (Cr/Cr_2O_3/Pd) having a Pd top contact.

In conclusion, a complete presentation of the theoretical dark current vs voltage curve for an MIM diode was presented. I presented a numerical method to calculate the electron tunneling probability for an arbitrary shaped barrier, without neglecting reflections within the barrier. I showed the cause of rectification reversal and its relation to the various material parameters. I developed several methods to evaluate the current density vs voltage with a computer. The results of the theoretical calculations, using literature values for the material parameters, were compared to the experimental diodes. I was able to obtain a range of results that spanned the experimental results. However, I could not uniquely fit the experiments because (a) the shape of the curves did not match (b) a perfect fit is of little value since multiple combinations are possible. To obtain a meaningful perfect fit further experimental data would be required to confirm the barrier heights, effective mass, and the oxide thickness.

IV. ILLUMINATED MIM DIODE – CLASSICAL THEORY

i. Classical Model

MIM diodes have been used for rectification and mixing of infrared radiation. The tunneling time of electrons, calculated using wavepackets, have been estimated to be on the order of 10^{-16} seconds by several authors and as a result the DC measured J(V) curve of an MIM diode is the same as that at high frequencies (Faris, 1973). The estimates of tunneling time calculated from wavepacket propagation, although frequently used, are questionable (Landauer, 1994). However, experimentally MIM diodes have been shown to rectify green light (514 nm), indicating the tunneling time of carriers is not yet a limitation in MIM diodes (Elchinger, 1976). The primary limitation of the MIM diode response time is the associated RC time constants.

Low frequency illumination of an MIM diode coupled to an antenna can be understood in terms of electrical engineering circuit theory. Electromagnetic radiation is incident upon the MIM diode antenna and is subsequently focused across the insulator of the MIM diode. Treating the incident radiation as a time-varying potential is acceptable when the MIM diode is much smaller than the wavelength of the incident light (Wengler, 1992). Furthermore, coupling 100 % of the incident power from the radiation field to a device smaller than a wavelength of the incident radiation is possible with proper impedance matching. This remains true at optical wavelengths (Grober, 1997).

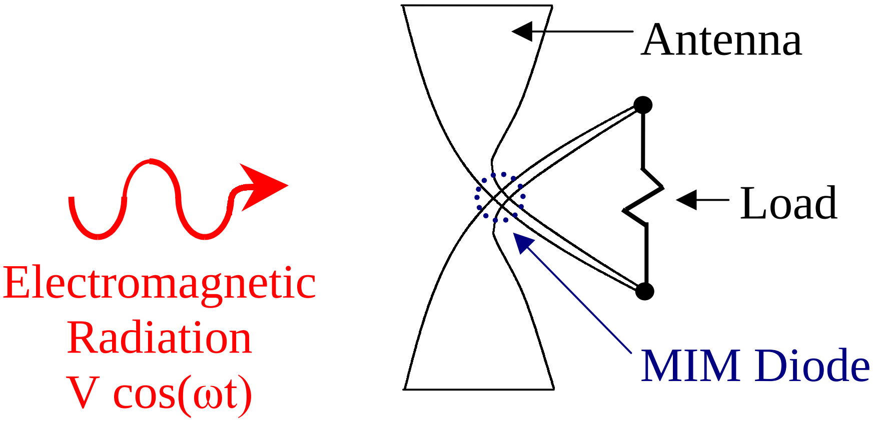

Fig. 4-1. *Electromagnetic radiation is incident upon the MIM diode antenna. The antenna subsequently focuses the electric field of the photons across the MIM diode (located at the overlap of the antenna). The MIM diode in turn rectifies the electric field to provide power to the load.*

The device shown in Figure (4-1) may be reduced to a classical circuit model using a sinusoidal voltage source, representing the incident electromagnetic field, a series resistance representing the antenna impedance, followed by the MIM diode connected to the load. The MIM diode is modeled as a voltage-dependent resistance in parallel with a geometric capacitance. This circuit model is an approximation because, at these frequencies, each of the elements is distributed, not lumped as shown in the circuit model.

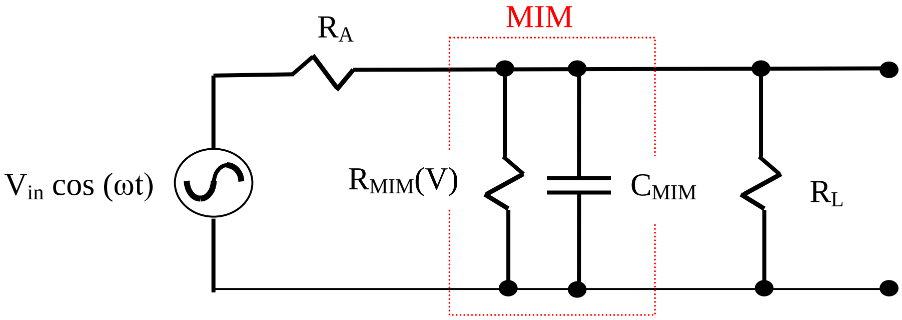

Fig. 4-2. *The classical circuit model of an MIM diode coupled to the incident radiation through an antenna. The nonlinearity of the diode is modeled with the voltage-dependent resistance $R_{MIM}(V)$. The rectified output voltage appears across the load resistor R_L. This simplified circuit model neglects the additional inductance(s), capacitance(s) and resistance(s) that may be associated with the metal and transmission lines.*

The basic circuit model of Figure (4-2) does not include the extra inductance(s), capacitance(s) and resistance(s) that may be associated with the metal leads to the antenna, MIM diode, substrate, and the load.

The complex conductivity associated of the metal may be calculated from the using the Drude model (Ashcroft, 1976).

$$\sigma(\omega) = \frac{\sigma_{DC}}{1 - j\omega\tau} = \frac{1}{\rho(\omega)} \tag{4.1.1}$$

By separating the complex conductivity of equation (4.1.1) into a real and imaginary portion the capacitance of the metal may be extracted from the imaginary impedance; where the impedance of a capacitor is equal to the inverse of the capacitance times the radial frequency. In Figure (4-3) I evaluate the imaginary impedance and associated capacitance of aluminum as a function of frequency $\sigma(\omega)$ using a nominal DC conductivity σ_{DC} value of 4.08×10^5 cm/ohm and a lifetime τ of 8×10^{-15} seconds.

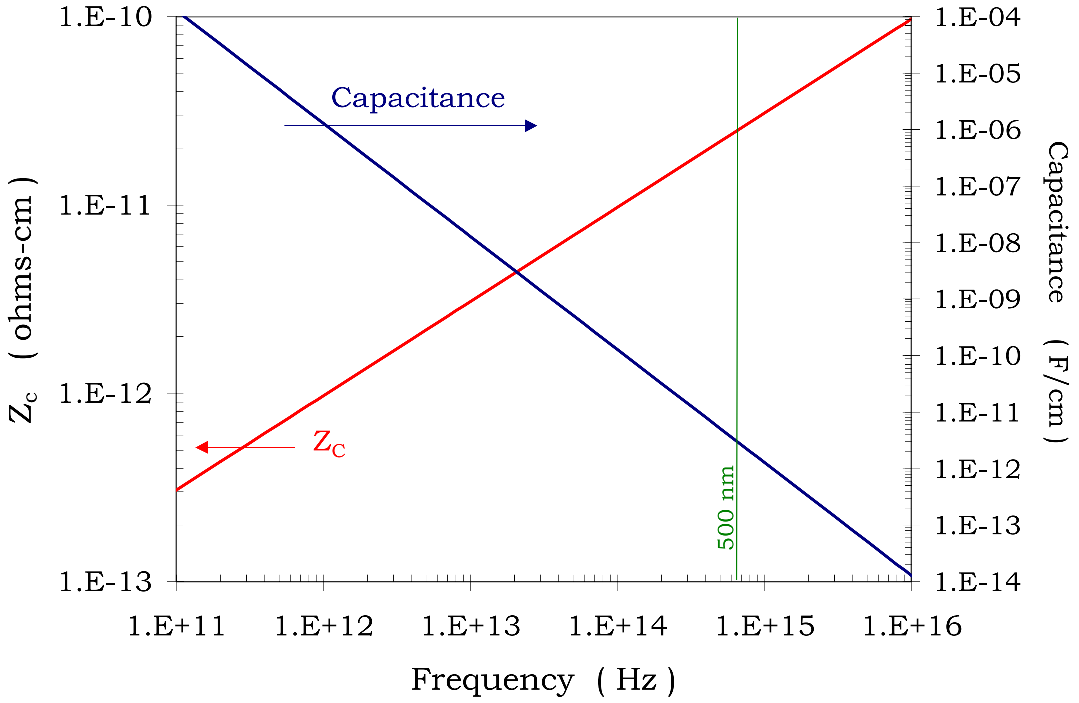

Fig. 4-3. *Capacitance and associated impedance as a function of frequency for aluminum calculated using the Drude model.*

If we assume that the relevant propagation distance is a quarter of the wavelength we find that for 500 nm light the capacitive impedance is approximately 25×10^{-21} ohms.

A more important factor at high frequency will be the increase in the resistance of the metal as a function of frequency due to the decreasing skin depth (Ramo, 1994). The skin depth in metal δ may be expressed in terms of the dc conductivity σ_{DC} and the dc permeability μ_{DC}.

$$\delta = \frac{1}{\sqrt{\pi \, f \, \sigma_{DC} \, \mu_{DC}}} \tag{4.1.2}$$

In Figure (4-4) I have calculated the sheet resistance of aluminum using a DC permeability value of $4\pi \times 10^{-7}$ H/m.

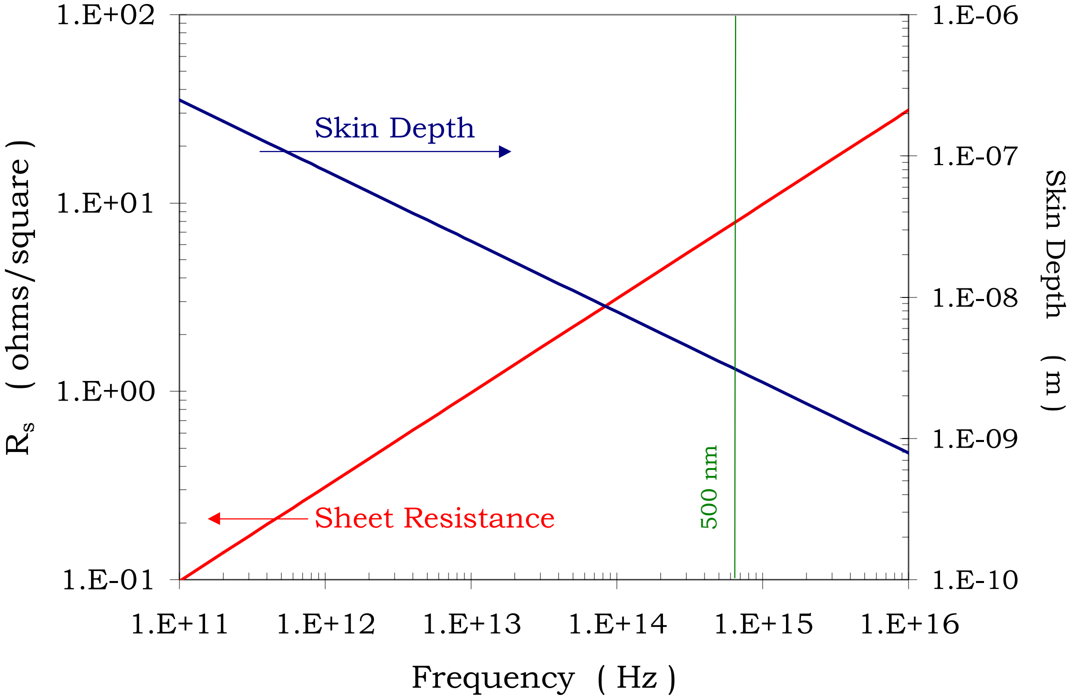

Fig. 4-4. *Sheet resistance and skin depth of aluminum as a function of frequency.*

In the green part of the spectrum, we find that the skin depth decrease to 3.4 nm with a sheet resistance of 7 ohms/square. Consequently, the impedance of the metal should be taken into consideration for both the antenna and transmission line design.

There is a further concern in assuming the solar radiation is coherent across the MIM diode and that a single sinusoidal source is an appropriate model. The radius of coherence for the sun may be estimated from the following relation (Saleh, 1991).

$$R_{coherence} = 1.22 \frac{\lambda}{2 \cdot \cot\left(\dfrac{R_{source}}{D_{source}}\right)} \tag{4.1.3}$$

where $R_{coherence}$ is the radius of coherence, R_{source} is the radius of the source, and D_{source} is the distance from the source. Using nominal values for the radius of the sun (695950 km) and the distance from the sun (1.6 million km) we find that the radius of coherence across the spectrum is approximately 1.5 wavelengths. Consequently, using a single sinusoidal source for a single MIM diode is appropriate. However, if an array of MIM diodes is used, it is unlikely that the sun will be coherent to all MIM diodes across the array.

Classical rectification may occur in two different manners: linear and square-law (Torrey, 1964). The dominant mechanism depends on the explicit shape of the MIM diode J(V) curve in relation to the magnitude of the oscillating voltage imposed across the diode. Linear rectification is a large signal model while square-law detection is a small signal model. In linear rectification we rely on the diode switching between highly resistive and highly conductive states. In square law detection the 2nd order derivatives (and higher 4th, 6th, etc.,) produce a rectified voltage across the MIM diode when only a small oscillation is being induced across the diode by the incident radiation.

ii. Square-Law Rectification

Sanchez developed an analytical small signal model for MIM diodes that rectify by square law detection (Sanchez, 1974). The model utilizes a circuit similar to the one in Figure (4-2). The responsivity of the MIM diode is used to determine the magnitude of the rectified current produced.

Responsivity is calculated from a second order Taylor series approximation to the MIM diode J(V) curve (Torrey, 1964).

$$I(V_{op}+V_s) = I(V_{op}) + \frac{I'(V_{op})}{1!}V_s + \frac{I''(V_{op})}{2!}V_s{}^2 + \frac{I'''(V_{op})}{3!}V_s{}^3 + \ldots \qquad (4.2.1)$$

The differential resistance of the MIM diode at the operating point is equal to the inverse of the first derivative of current with respect to voltage evaluated at the operating point. Retaining only the terms through second order in equation (4.2.1) the voltage out of the MIM diode, without applied bias, may be evaluated using Ohm's law.

$$V_{MIM} = \frac{1}{I'}\left[I'V_s + \frac{I''}{2}V_s{}^2\right] \qquad (4.2.2)$$

Consequently, the responsivity will be limited to regimes where the second order Taylor series expansion adequately models the MIM diode J(V) curve.

The small signal voltage induced upon the diode by the incident electromagnetic energy has the form $V_{ph} \cdot \cos(\omega t)$. We insert the small signal voltage into equation (4.2.2) to find the rectified voltage, and then through Ohm’s law, the rectified current.

$$I_{MIM} = \frac{I''}{2} {V_{ph}}^2 \cos^2(\omega t) \qquad (4.2.3)$$

The power absorbed in the MIM diode is equal to

$$P_{MIM} = {V_{MIM}}^2 I' \qquad (4.2.4)$$

The responsivity of the MIM diode is defined as the current produced per watt of power absorbed which may be obtained from the ratio of equation (4.2.3) to (4.2.4).

$$\Re(V) = \frac{1}{2} \frac{I''}{I'} \bigg|_{V=V_{op}} \qquad (4.2.5)$$

In the quantum limit responsivity times the photon energy is equal to the quantum efficiency.

Sanchez uses the circuit model of Figure (4-2) (neglecting the load resistor) and assumes that the MIM diode resistance $R_{MIM}(V)$ may be reduced to a single resistance value about a zero applied bias operating point. This simplifies the model and allows voltage across the MIM diode to be calculated by voltage division between the MIM diode and the antenna impedance.

Using the MIM diode responsivity the rectified current produced may be calculated and subsequently the rectified power at the diode. The power conversion efficiency of the diode is calculated from the rectified power out divided by the incident power.

$$\eta = 2(\Re_0 \, V_{MAX})^2 \left[\frac{\left(\dfrac{R_{MIM}}{R_A}\right)^3}{\left(1 + 2\left(\dfrac{R_{MIM}}{R_A}\right) + \left(1 + (\omega \, R_A \, C_{MIM})^2\right)\left(\dfrac{R_{MIM}}{R_A}\right)^2\right)^2} \right] \qquad (4.2.6)$$

We may make several observations on the conversion efficiency by means of square-law detection. First, in the limit that $R_A \cdot C_{MIM}$ is sufficiently small compared to the excitation frequency, equation (4.2.6) reduces to a polynomial equation in terms of the ratio of R_{MIM} to R_A. The efficiency is then maximized by setting $R_{MIM} = R_A$. Then the efficiency is limited by the value of responsivity and the maximum voltage that may be sustained across the MIM diode without breakdown (V_{MAX}). The limitations of the approximations are evident because the efficiency increases without bounds as we increase the responsivity and V_{MAX}.

Physically, in the quantum limit the responsivity has a maximum value of $1/E_{ph}$ where E_{ph} is the photon energy in electron volts. The maximum voltage V_{MAX} has an upper limit that depends on the magnitude of electric field that the oxide can support prior to breakdown.

Consider an MIM diode illuminated by 5 μm radiation, which corresponds to a frequency of 6×10^{13} Hz. The maximum value of responsivity is approximately 4

A/W. I will assume that the antenna resistance is equal to the impedance of free space, 377 Ω. A small area MIM diode with a small zero bias resistance will require a thin oxide. I will assume the oxide is 1.5 nm thick, has a relative dielectric constant of 10 and can support a constant electric field of 10^6 V/cm. The capacitance of the diode may then be evaluated as 5.9×10^{-6} F/cm^2. I will assume that the zero bias resistance of the diode is 377 Ω when the device is 100 nm × 100 nm in size which corresponds to a zero bias resistance of 3.77×10^{-8} Ω-cm^2. We may then calculate the efficiency from equation (4.2.6) as a function of the MIM diode area, or equivalently the edge length of a square MIM diode, shown in Figure (4-5).

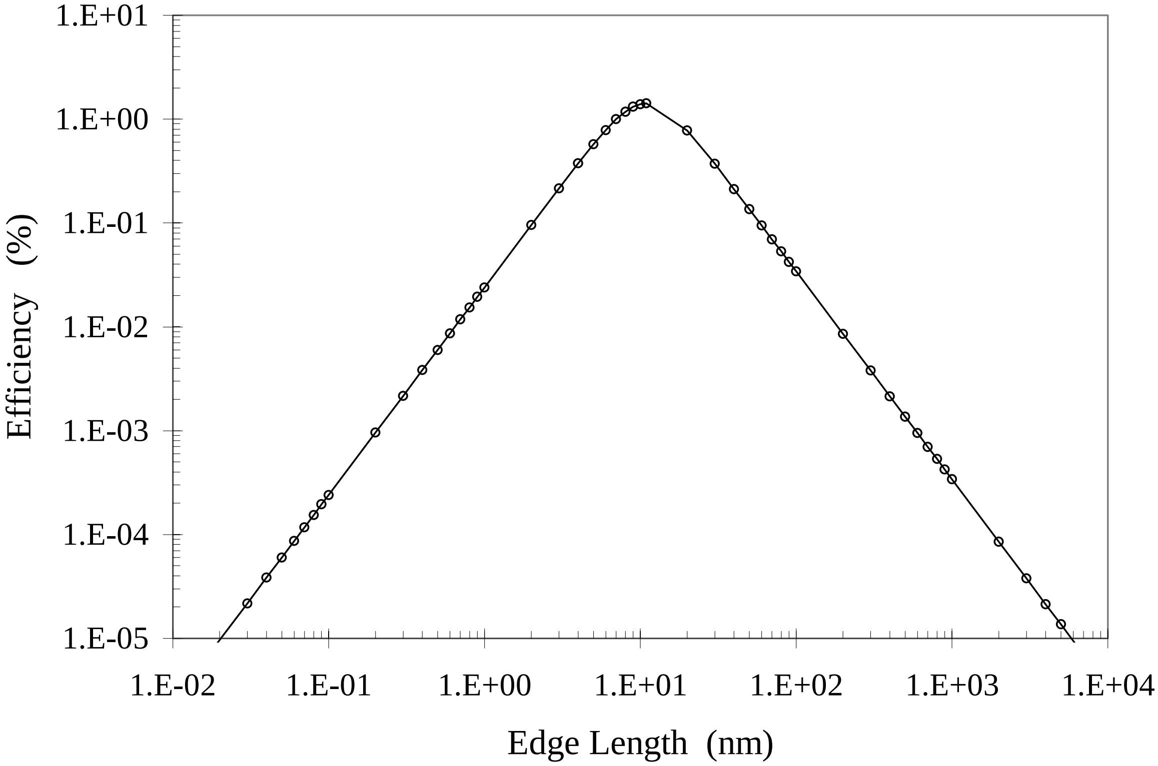

Fig. 4-5. *MIM diode efficiency, rectified power out divided by incident power, as a function of the diode size.*

This diode exhibits a peak efficiency of 1.4 % when the diode size is 11 nm × 11 nm. The peak in efficiency is a direct result of the impedence matching between the MIM diode and the antenna. A 11 nm × 11 nm diode has a capacitance is 7.1×10^{-18} F which translates to an impedance of 371 Ω. The resistance of the diode is 31.2 kΩ which may be ignored when in parallel with the smaller capacitor impedence.

If the capacitor were made sufficiently small such that $\omega R_A C_{MIM}$ were much less than 1, then the peak in efficiency would reach 60 % with a diode area of 100 nm × 100 nm, where the antenna resistance is equal to the diode resistance. Consequently, to obtain high efficiency at high frequencies, we must make the geometric capacitance of the MIM diode as small as possible, as shown in Figure (4-6).

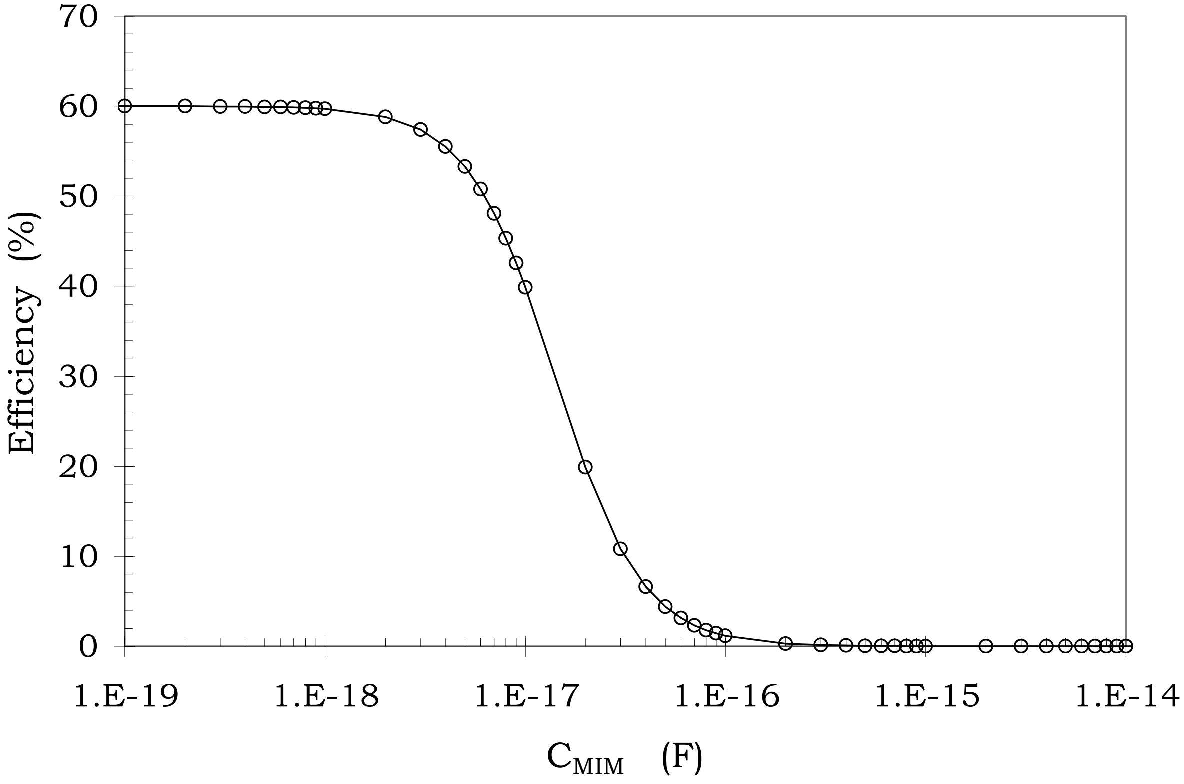

Fig. 4-6. *MIM diode efficiency as a function of the diode's geometric capacitance. Maximum efficiency is obtained with small MIM diode capacitance.*

The geometric capacitance of the diode may be reduced by decreasing the dielectric constant of the oxide, increasing the oxide thickness, or decreasing the device area. The capacitance of the MIM diode decreases linearly with increasing oxide thickness. Unfortunately, the oxide thickness effects both the resistance and capacitance of the MIM diode and the current decreases in a highly nonlinearly fashion with increasing oxide thickness. Subsequently in MIM diode design we decrease the geometric capacitance of the MIM diode by decreasing the area. Changes in area alter both the resistance and the capacitance of the MIM diode linearly.

Figure (4-7) shows the calculation of the required MIM diode size (edge length of a square diode) as a function of wavelength for various oxide thicknesses. In performing the calculation I have assumed the MIM diode resistance is equal to 377 Ω and that the dielectric constant of the oxide is 4.5.

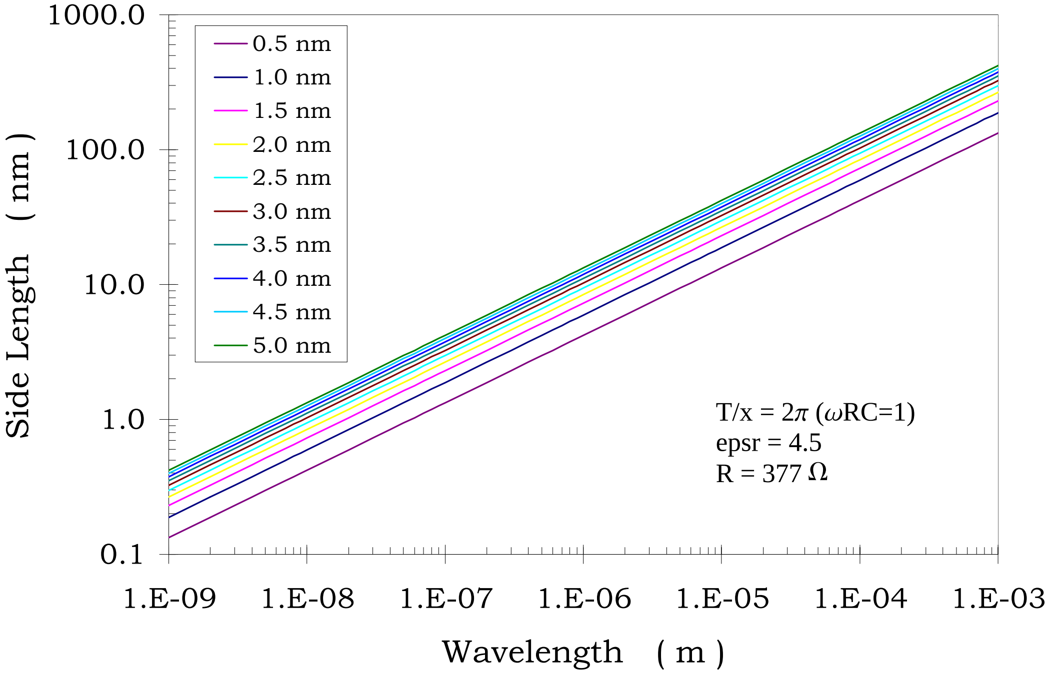

Fig. 4-7. *The required MIM diode size (side length) as a function of wavelength for various oxide thicknesses. The resistance is assumed to be 377 Ω and the capacitance chosen such that the RC time constant of the diode times the radial frequency is equal to 1 (the period of the photon oscillation T divided by the RC time constant is equal to 2π).*

The RC time constant of the diode is dictated by the size of the MIM diode. The RC time constant is limited to the period of the photon divided by 2π which is equivalent to RCω=1. We find that for the center of the solar spectrum a 5 nm × 5 nm diode is required. However, if a lower resistance diode is used this size will increase.

The resistance of the diode may be decreased substantially by decreasing the oxide thickness or tailoring the barrier heights. Tailoring the barrier heights does not change the MIM diode capacitance.

Despite the limitations of the model it teaches that if we effectively impedance-match the MIM diode to the antenna, Figure (4-3), minimize the capacitance, Figure (4-4), and maximize the responsivity, Equation (4.2.2), high efficiency may be obtained. If the magnitude of the voltage imposed upon the MIM diode become large enough that a second order Taylor series expansion of the I(V) curve no longer accurately represents the MIM diode I(V) curve we can no longer use this model. Numerical methods, such as the PSpice model used for linear rectification, must be used.

iii. Linear Rectification

In linear rectification the magnitude of the voltage oscillation across the MIM diode is large and the diode functions as a switch. The classical responsivity and small signal model developed by Sanchez are no longer valid due to the magnitude of the voltage swing across the MIM diode.

An ideal switching diode has an infinite reverse bias resistance and zero forward bias resistance. During the positive swing of the sinusoidal input, the diode is reverse biased and all of the power provided by the input source is dissipated in the load and antenna resistance since $R_{MIM} >> R_L$. At low frequencies, the maximum power transfer to the load is 50 % when the antenna is matched to the load $R_A=R_L$.

At high frequency the capacitance of the MIM diode is important. A capacitor has an impedance of $Z_c=1/(j2\pi f \cdot C_{MIM})$. Consequently, we must make C_{MIM} small such that its impedance Z_c is much greater than R_L (R_A) to prevent stealing power away from the load. This impedance requirement is met by the statement at the beginning of this section and in most MIM literature: that $R_A \cdot C_{MIM}$ must be sufficiently small to keep up with the incident radiation, or $R_A \cdot C_{MIM}$ is much smaller than the period of the input oscillation (where $R_A=R_L$).

During the negative voltage swing of the sinusoidal input the diode is forward biased and produces a short circuit across the load since $R_{MIM} << R_L$. Consequently, the power is dissipated in the antenna resistance. Furthermore, any attempt of charge storage by means of a capacitor will be ineffective due to the low diode resistance and subsequent low RC time constant path to ground. This means that although we can rectify the electromagnetic radiation, we are unable to remove the ripple and truly convert it to a DC signal with a capacitor. Rather, we must detect the average signal.

In standard rectifiers the load is placed in series with the diode. The RC time constant of the diode $R_{MIM} \cdot C_{MIM}$ must be kept small so that the diode may keep up with the incident radiation. In this series configuration a capacitor in parallel with the load is capable of removing the ripple in the rectified signal.

iv. PSpice Model

Accurate modeling of a MIM diode in a large signal circuit requires use of the I(V) curve at more than a single operating point. The PSpice model allows the diode's entire I(V) curve to be taken into consideration and thus also includes rectification reversal and self-bias effects. The PSpice model is not based on the device physics of MIM diodes, but instead replicates a user provided I(V) curve. This allows any electron device I(V) curve to be imported into PSpice and simulated in any electrical circuit.

The MIM diode I(V) curve is modeled with the use of three circuits: the main circuit and two isolated subcircuits. The main circuit is shown in Figure (4-8). This circuit represents the MIM diode and is connected to any circuit via nodes 20 and 30 (the two terminals of the diode). The voltage-controlled current source $G_{MIM}I(V101)$, where V101 is the voltage at node 101, in conjunction with the two subcircuits produces a current that is a function of the voltage across the MIM diode (between nodes 20 and 30). C_{MIM} is the geometric capacitance of the MIM diode.

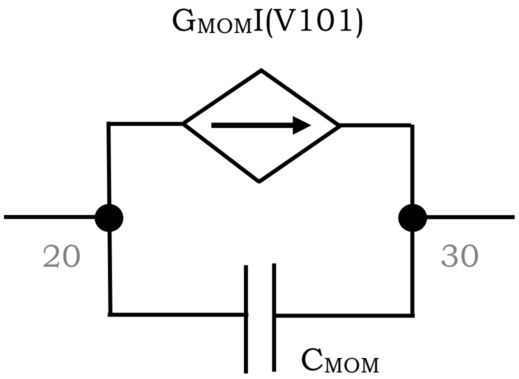

Fig. 4-8. *The main metal-insulator-metal diode subcircuit. $G_{MIM}I$ is a voltage dependent current source. The current produced is a function of the diode area and the voltage at node 101 in Figure (4-9).*

The first isolated subcircuit is shown in Figure (4-9). This subcircuit produces a voltage at node 101 which in-turn controls $G_{MIM}I(V101)$ in the main MIM diode circuit. This circuit must be included in the PSpice net list along with the main circuit of Figure (4-8), however, this circuit is isolated and node 101 must not be common with any other portion of the large signal circuit. The voltage at node 101 is produced by the voltage-dependent-current-source $G_{MIM}J(V100)$ forcing a current through the series resistor. $G_{MIM}J$ uses the PSpice table function to hold the MIM diode I(V) curve data. The 1 ohm series resistor functions as a multiplier to the current data in the I(V) table. To reproduce the table data without any scaling, the resistor value is set to 1 ohm. As a result, the voltage at node 101 is equal to the current produced by $G_{MIM}J(V100)$. A change in the scaling factor physically represents a change in the area of the diode.

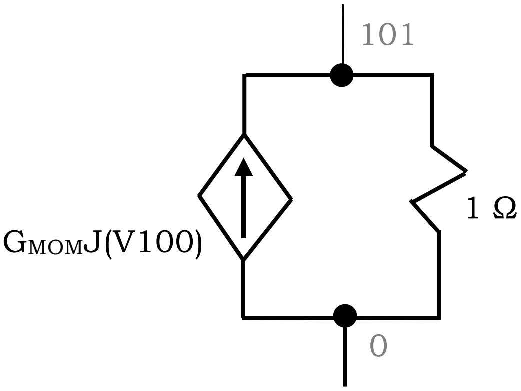

Fig. 4-9. *The first isolated subcircuit containing the table of user provided current vs voltage data.* $G_{MIM}J$ *is a voltage dependent current source. The current is dependent on the voltage at node 100 in the subcircuit of Figure (4-10). The current vs. voltage data is held in a PSpice table.*

The second isolated subcircuit is shown in Figure (4-10) The role of this circuit is to replicate the voltage across the MIM diode (nodes 20 and 30) and in turn produce a voltage a node 100 that controls $G_{MIM}J(V100)$. This subcircuit must be included in the PSpice net list, however, may not have node 100 in common with any part of the large signal circuit. The voltage-dependent-voltage-source $E_{MIM}V(V20-V30)$, replicates the voltage across the main MIM diode circuit (between nodes 20 and 30). The 1 megohm resistor is only used to complete the subcircuit.

The combination of the main MIM diode circuit and the two isolated subcircuits allow any theoretically, experimentally or hypothetically provided current vs voltage data to be replicated within PSpice.

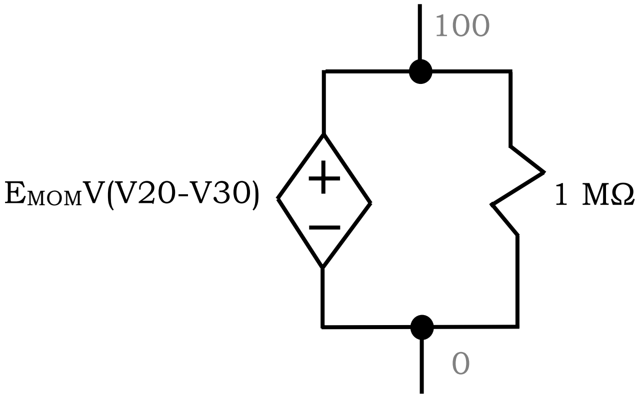

Fig. 4-10. *The second isolated subcircuit replicates the voltage across the MIM diode. $E_{MIM}V$ is a voltage dependent voltage source. The voltage produced is equal to the voltage across the MIM diode (the voltage difference between nodes 20 and 30 from Figure (4-8)).*

A series rectifier circuit consists of an ac input voltage source with a series resistance to represent the input electromagnetic radiation coupled through an antenna to the MIM diode, placed in series with the MIM diode model of Figure (4-8). A standard half-wave rectifier circuit has the load impedance in series with the diode. For the antenna coupled MIM diode the load impedance must be placed in parallel with the MIM diode so the electromagnetic field is applied across the oxide. With a parallel load we are able to rectify the electromagnetic radiation but we are unable to convert the rectified signal into a true DC signal by means of a capacitor. This is because a sufficiently large capacitor, to remove the ripple in the rectified signal, would introduce low resistance path around the load and MIM diode.

The frequency of the input source was chosen at a frequency of 6×10^{13} Hz (λ=5 μm) to simplify numerical convergence within PSpice (the minimum time step in PSpice is 10^{-21} s). Generally, the solar conversion device operates at much higher frequencies. In linear rectification the MIM diode operates as a switch and we want the load impedance equal to the antenna impedance for maximum power transfer during the diode forward bias cycle. We have set both the antenna and load resistances equal to 377 Ω.

The dc voltage V_{DC} across the MIM diode and load resistor and power conversion efficiency η of the rectifier are then calculated as a function of input voltage. The power conversion efficiency η is defined from equation (4.4.1-4.4.4).

$$P_{IN} = \frac{1}{T}\int_{t}^{t+T} V_{IN}(t)\, I_{IN}(t)\,\partial t \tag{4.4.1}$$

$$V_{DC} = \frac{1}{T}\int_{t}^{t+T} V_{LOAD}(t)\,\partial t \qquad I_{DC} = \frac{1}{T}\int_{t}^{t+T} I_{LOAD}(t)\,\partial t \tag{4.4.2a,b}$$

$$P_{DC} = V_{DC}\, I_{DC} \tag{4.4.3}$$

$$\eta = \frac{P_{DC}}{P_{IN}} \tag{4.4.4}$$

where P_{DC} is the average output power of the rectifier and P_{in} is the ac input power. The average output voltage and current are calculated by integration over an integral number of periods T.

The theoretical current vs voltage curve for a MIM diode having a left barrier height of 0.3 eV, a right barrier height of 2.75 eV, and an oxide thickness of 3.0 nm was simulated.

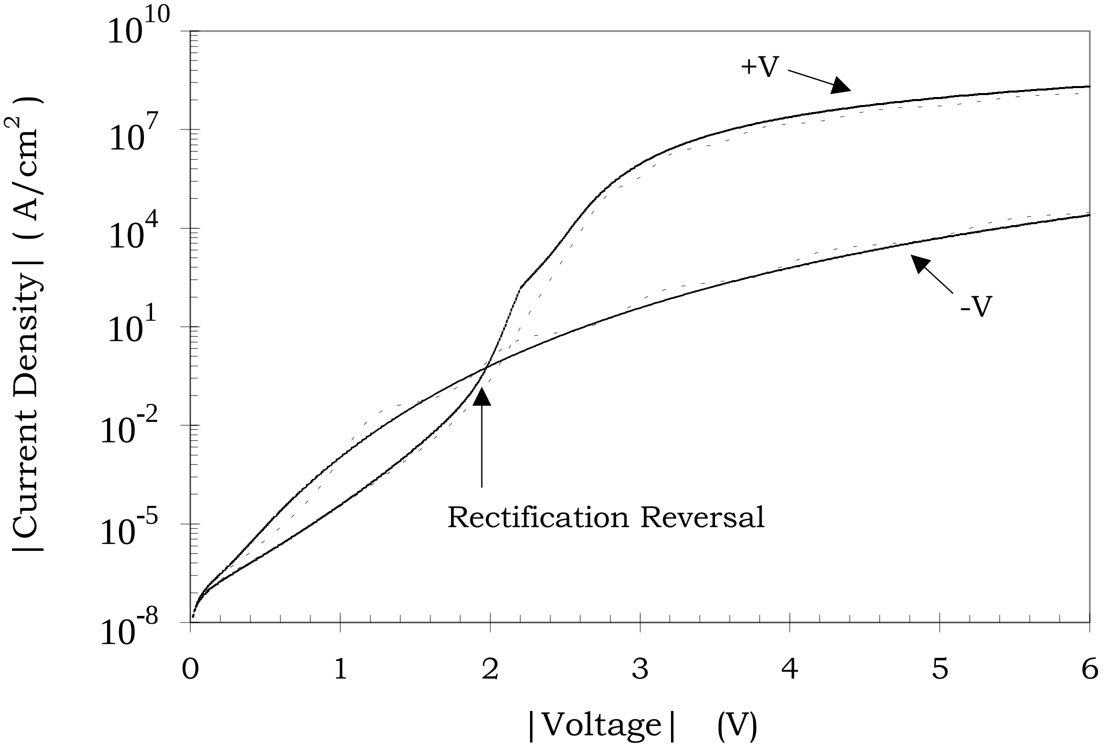

Fig. 4-11. *Theoretical room temperature current density vs voltage curve for a metal-insulator-metal diode with a left barrier of 0.3 eV, an oxide thickness of 3 nm, and a right barrier of 2.75 eV. The solid trace is calculated using the WKB approximation to the electron tunneling probability and the dashed trace uses the numerical plane wave solution. The base metal is grounded and the voltage is applied to the top metal.*

The diode J(V) data from Figure (4-11) was subsequently used with the PSpice MIM diode model.

I first used PSpice to simulate the MIM diode of Figure (4-11) within a standard series rectifier. In the series rectifier the limiting RC constant of the circuit is the resistance of the MIM diode times the capacitance of the MIM diode. I have set the capacitance equal to zero in the series circuit simulation because the resistance of the MIM diode increases to large values for low applied biases and would limit the upper frequency of operation. When the MIM diode is in series with the load resistance the conversion efficiency and voltage across the load vary as a function input voltage magnitude. Furthermore, the voltage across the load switches polarity and the conversion efficiency drops as we pass through the reversal point of the MIM diode. The efficiency calculation results are plotted Figure (4-12).

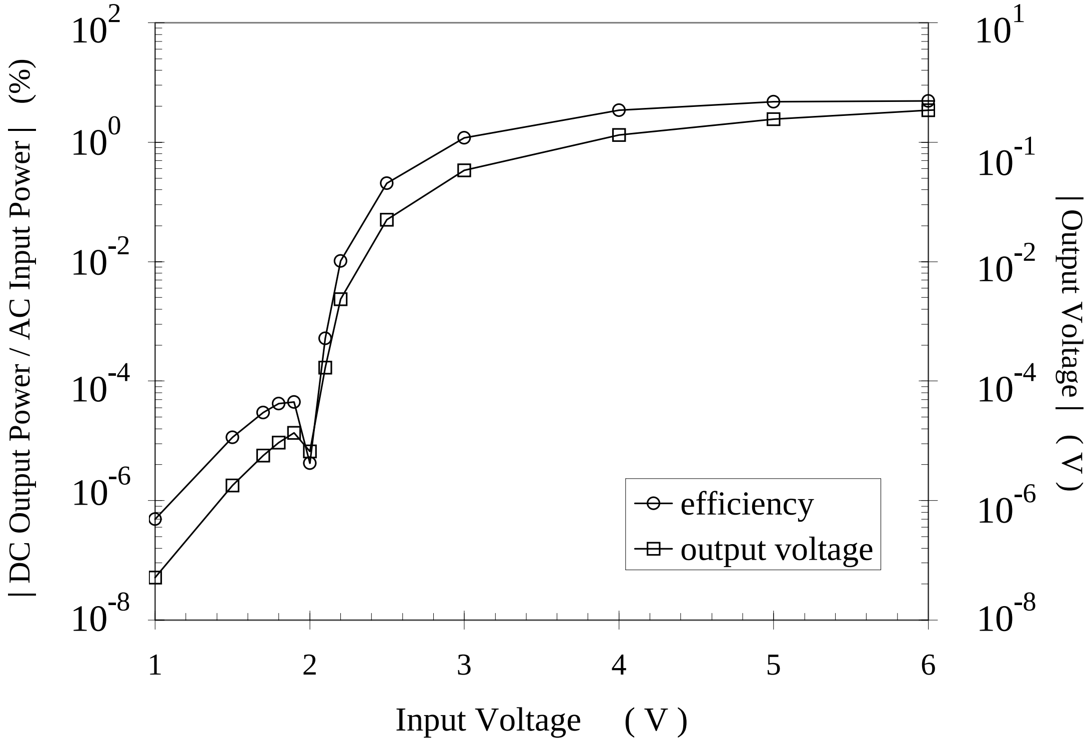

Fig. 4-12. *Power conversion efficiency (ac-to-dc) and rectified voltage output as a function of peak input voltage for a series rectifier circuit using the metal-insulator-metal diode of Figure (4-11). The WKB approximation to the electron tunneling probability is used in the MIM diode J(V) calculation and the diode capacitance is neglected. The output voltage is positive to the right and negative to the left of the dip.*

The polarity switch in rectified output voltage from the rectifier and the decrease in efficiency due to rectification reversal are clearly evident at the dip present in the logarithmic plot. The dc voltage across the load is positive to the right of this dip and negative to the left.

When the load is placed in parallel with the MIM diode, as we would find in a solar energy harvesting situation depicted in Figure (4-1), the voltage across the MIM diode and load is the same. The resistance of the MIM diode is a function of the voltage applied across the diode. As we sweep the input voltage to sufficiently high values, the MIM diode has a lower value of resistance than the load in both polarities and shorts out the load. A low resistance current path around the load is introduced through the MIM diode. With very low input voltages the resistance of the MIM diode is greater than the load under both forward and reverse biases. Consequently the high resistance MIM diode in parallel with the load does not affect the current through the load. Only over a small range of input voltages, where the diode resistance is larger than the load resistance for a bias of one polarity and smaller for the opposite polarity, does the MIM diode function as a switch. Consequently, sweeping the input voltage is not an effective method to detect the reversal when the diode is in parallel with the load. To illustrate the reversal phenomena in the parallel configuration I instead fix the input voltage to 5 volts and change the area of the MIM diode. By changing the area, the resistance of the MIM diode may be shifted with respect to the resistance of the load and therefore rectification reversal may be observed.

In the parallel rectifier the dominant RC time constant is the resistance of the antenna (assumed to be equal to the load) and the capacitance of the MIM diode. The capacitance of the MIM diode is a function of area. However, in this simulation I have set the capacitance equal to zero in order to remove the RC time constant limitations of the circuit and clearly illustrate the reversal. The efficiency calculation results are plotted in Figure (4-13).

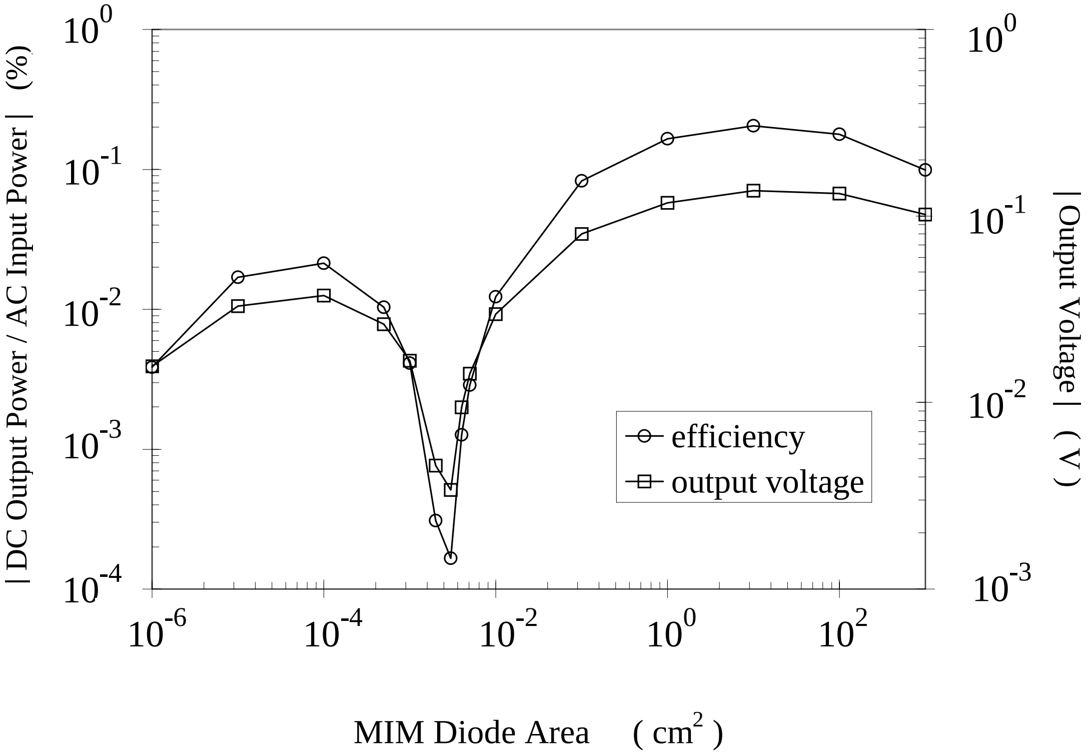

Fig. 4-13. *Power conversion efficiency (ac-to-dc) and rectified voltage output as a function of MIM diode area for a parallel rectifier circuit using the metal-insulator-metal diode of Figure (4-11). The capacitance of the MIM diode is neglected and the input voltage is 5 V. The WKB approximation to the electron tunneling probability was used in the MIM diode J(V) calculation. The output voltage is positive to the right and negative to the left of the dip.*

The polarity switch in rectified output voltage and decrease in efficiency due to rectification reversal are clearly evident at the dip present in the logarithmic plot. The dc voltage across the load is positive to the right of this dip and negative to the left. Choosing an MIM diode area away from the dip in Figure (4-13) will reduce the efficiency loss due to rectification reversal.

The RC time constant is a limitation of MIM diodes. I have set the capacitance of the MIM diode equal to zero in both the series and parallel configurations to clearly illustrate the reversal. Setting the capacitance to zero is acceptable if the RC time constant of the circuit is much smaller than the reciprocal of the input frequency. The capacitance of the unoptimized MIM diode we used to demonstrate rectification reversal would in reality limit the maximum operating frequency of the rectifier.

Again, rectification reversal is not a new phenomenon the implications have simply been neglected. Rectification reversal was observed by Simmons in his observations on MIM diode conductivity (Simmons, 1963). In small signal, biased detector applications rectification reversal is negligible and the MIM diode responsivity is a sufficiently accurate figure of merit. For MIM diodes in unbiased rectifier circuits rectification reversal can play a significant role.

The PSpice model illustrates the role of rectification reversal in unbiased classical rectifier circuits. The polarity of the dc output voltage for the rectifier circuit will depend on the peak voltage of the input signal. Power conversion efficiency will also be a strong function of the peak input signal voltage. Furthermore, with rectification reversal there is a particular input voltage that produces no rectification and no ac-to-dc power conversion.

The size of the rectification reversal in a MIM diode I(V) curve depends on the choice of metals, the oxide, and the oxide thickness. A thick oxide region reduces the rectification reversal effect by shifting the reversal location to higher voltage magnitudes at the cost of increasing the MIM diode resistance. The optimum MIM diode structure is thus a function of the particular rectifier circuit used.

The responsivity becomes an invalid figure of merit for MIM diodes as the input voltage, or field intensity, becomes large. A PSpice model has been developed to classically model MIM diodes for both large and small signal sinusoidal inputs, and is well suited to include rectification reversal. The PSpice model is a classical model and remains valid when the photon energy is less than any nonlinearity present in the MIM diode I(V) curve. In a rectifier circuit rectification reversal can cause a decrease in ac-to-dc power conversion efficiency and a polarity reversal in the rectified output signal. The PSpice model allows the user to accurately predict the importance of rectification reversal for their specific MIM diode and circuit. Since the model is based on user provided I(V) data it is not limited to MIM diodes.

iv. Classical Model Limitations

The models in this section are classical in nature. The classical models are limited to regimes where quantitization of the interaction between the MIM diode and the electromagnetic field are not required. As we will discuss in more detail in section V, this is reasonable when the quantum sizes of the field are small in comparison to the nonlinearities present in the MIM diode J(V) curve and the number of these quanta is large. Consequently, the classical picture is typically limited to long wavelengths where the photon energy is small.

It is important to keep in mind that equation (4.4.1) representing the input power is not physically correct for solar energy harvesting. This is because the sun continues to provide power even if the MIM diode and load do not draw any current from this power. In equation (4.4.1) if the MIM diode or load do not draw any current, the power in will be equal to zero. A more accurate representation would be to calculate the input power from the maximum power deliverable from the source.

$$P_{IN} = \frac{{V_{IN}}^2}{8R_A} \tag{4.4.5}$$

In regimes where the classical picture applies we are limited to efficiencies less than 25 %. Even with a perfect match between the antenna and the load 50 % of the power will be lost. Furthermore, because we are dealing with a half-wave rectifier 50 % of the power delivered to the diode will be lost in the rectification process. Therefore, we are limited to 25 % maximum conversion efficiency, less than obtainable by conventional semiconductor solar cell technology. The potential for higher conversion efficiencies are not found until we obtain photon stepping in the quantum regime.

In conclusion, I have presented the classical model of solar energy conversion with MIM diodes. I have shown that the designer of the antenna and bus lines between the MIM diode and the load will need to consider the increased impedance of the metal at high frequencies. I have shown that the incident photons are expected to be coherent over a region 1.5 times the their wavelength. Consequently, the incident photons are expected to be coherent for a single MIM diode. However, coherence would not be expected over an array of MIM diodes. I have presented

Sanchez's model for square-law rectification. From this model I have shown that we need to reduce the capacitance of the diode which may be accomplished by decreasing the diode area. Furthermore, the impedance of the diode must be matched to the antenna impedance for optimal conversion efficiency. The limitations of Sanchez's model to small input voltages was pointed out and I developed a PSpice model that will not be affected by the magnitude of the voltage swing across the diode. As a result the PSpice model may simulate linear rectification and include the effects of rectification reversal. The dependence of the rectified voltage polarity and decrease in conversion efficiency as a result of rectification reversal is presented. Finally, I have pointed out that the standard series rectifier is not appropriate for modeling solar energy conversion with MIM diodes and a parallel rectifier must be used. A consequence of the parallel rectifier configuration is that we cannot obtain a true DC signal out of the MIM diode solar cell.

V. ILLLUMINATED MIM DIODE – SEMICLASSICAL THEORY

i. Introduction

In classical MIM diode theory the MIM diode in conjunction with the light source is treated as a classical rectifier coupled to a sinusoidal voltage source representing the incident electromagnetic radiation. This classical theory is applicable to MIM diodes operating at low frequencies. At low frequencies the quantum nature of the MIM diode-radiation interaction may be ignored because the size of the electromagnetic field quanta is negligibly small and the classical PSpice model developed in section IV may be used.

At higher frequencies the quantum energy, or photon energy, of the electromagnetic field is not negligibly small and the quantum nature of the electromagnetic field interaction with the MIM diode must be accounted for. More precisely, the inadequacies of the classical treatment become evident when the photon energy is sizeable in comparison to the voltage width of the nonlinearity in the MIM diode's dark current vs voltage curve. Consequently, it is the MIM diode's dark current vs voltage curve (observed at non-negligible current magnitudes) that dictates the boundary between low and high frequency.

The classical to quantum transition is physically different from the transition between the small signal and large signal analysis techniques used in circuit theory. For example, the 10 kHz sinusoidal voltage that may be applied to a classical rectifier in the circuits lab has energy quanta of 4.1×10^{-14} V. However, we may make the voltage amplitude of the signal any value we desire within the limits of the signal source. For the dark current vs voltage curve for most electron devices the nonlinearity over a voltage span of 4.1 x 10^{-14} V is negligible. Consequently, we may neglect the quantum nature of a 10 kHz signal.

ii. Theory

In the semiclassical illuminated J(V) theory of MIM diodes the electric field of the incident optical radiation is treated as a classical quantity and time dependent perturbation theory is applied to the electrons in the electrodes of the MIM diode. The incident optical radiation is coupled from free space to the diode via an antenna. For this analysis we will assume the antenna is 100 % efficient at coupling the incident photons from free space and focusing their electromagnetic field across the oxide of the MIM diode.

When the coupling between the electromagnetic field and the MIM diode is weak the interactions with the vacuum field may be neglected. Additionally, if the field is sufficiently strong, or the number of photons is large, the uncertainty in classical field amplitude and phase of the radiation is small. In the regime of strong fields and weak coupling the semiclassical treatment of the electromagnetic field is well justified. When these conditions are not met quantum electrodynamics is required for proper treatment of the field. Finally, in the semiclassical treatment of the optical radiation only absorption and stimulated emission are accounted for, spontaneous emission is not included.

We begin with the time dependent Schrödinger wave equation

$$i\hbar \frac{\partial \Psi_e(\vec{r},t)}{\partial t} = \hat{H}\, \Psi_e(\vec{r},t) \tag{5.2.1}$$

where Ĥ is the Hamiltonian operator and Ψ_e is the electron wave function composed of both a spatial and time dependent parts. The complete system Hamiltonian is separated into two components: a time independent un-perturbed term H_o and a time dependant perturbed term H'(t).

$$\hat{H} = \left(H_o + H'(t)\right) \tag{5.2.2}$$

We recast the Schrödinger wave equation into vector notation and use the matrix formalism of quantum mechanics.

$$i\hbar \frac{\partial}{\partial t}\left|\Psi\right\rangle = \left(H_o + H'(t)\right)\left|\Psi\right\rangle \tag{5.2.3}$$

The eigenfunction of the perturbed system $|\Psi\rangle$ may be expressed in terms of the orthonormal eigenfunctions $|n\rangle$ of the unperturbed system by use of the expansion theorem.

$$\left|\Psi\right\rangle = \sum_{n=1}^{n=\infty} c_n(t)\left|n\right\rangle \tag{5.2.4}$$

We substitute the eigenfunction of the perturbed system into the Schrödinger wave equation and subsequently create the inner product with eigenvector m.

$$\left\langle m \middle| i\hbar \frac{\partial}{\partial t} \sum_{n=1}^{n=\infty} c_n(t) \middle| n \right\rangle = \left\langle m \middle| \left(H_o + H'(t)\right) \sum_{n=1}^{n=\infty} c_n(t) \middle| n \right\rangle \tag{5.2.5}$$

This is a typical procedure to simplify the Schrödinger wave equation. We expand and simplifying equation (5.2.5) making use of the orthonormality between eigenvector m and n. We may then reduce the equation to

$$i\hbar \frac{\partial}{\partial t} c_n(t) = \sum_{n=1}^{n=\infty} H_{mn} c_n(t) \tag{5.2.6}$$

where c_n is the expansion coefficients and H_{mn} is the Hamiltonian matrix.

The Hamiltonian matrix may be separated into an unperturbed Hamiltonian matrix and a perturbed Hamiltonian matrix.

$$H_{mn} = \begin{bmatrix} \varepsilon_1 & 0 & 0 & \cdots & 0 \\ 0 & \varepsilon_2 & 0 & \cdots & 0 \\ 0 & 0 & \varepsilon_3 & \cdots & 0 \\ \vdots & \vdots & \vdots & \ddots & \vdots \\ 0 & 0 & 0 & \cdots & \varepsilon \end{bmatrix} + \begin{bmatrix} H'_{11} & H'_{12} & H'_{13} & \cdots & H'_{1n} \\ H'_{21} & H'_{22} & H'_{23} & \cdots & H'_{2n} \\ H'_{31} & H'_{32} & H'_{33} & \cdots & H'_{3n} \\ \vdots & \vdots & \vdots & \ddots & \vdots \\ H'_{m1} & H'_{m2} & H'_{m3} & \ldots & H'_{mn} \end{bmatrix} \tag{5.2.7}$$

In the limit where the perturbation goes to zero, we are left with the eigen energies of the unperturbed system. In the perturbation matrix the elements along the diagonal effectively shift the unperturbed energy levels with respect so some fixed reference potential. The off-diagonal elements produce transitions between energy levels or quantum jumps. The first task in solving equation (5.2.6) is to calculate the explicit form of the system Hamiltonian for a MIM diode coupled to a sinusoidal perturbation.

The Hamiltonian describing the interaction between a classical electromagnetic field and an electron of mass m_e and charge –q is written as

$$\hat{H} = \frac{1}{2m_e}\left[\hat{p} + q\vec{A}\right]^2 + V(\vec{r}) \tag{5.2.8}$$

where A(r,t) is the vector magnetic potential, p is the momentum operator, and V(**r**) is the static electric potential (Kroemer, 1994). We make the common gauge choice of ∇•**A**=0 and separate the system Hamiltonian into the time dependent and perturbation terms.

$$\hat{H} = H_o + H'(t) = \left[\frac{\hat{p}^2}{2m_e} + V(\vec{r})\right] + \left[\frac{q}{m_e}\vec{A}\cdot\hat{p} + \frac{q^2\vec{A}^2}{2\,m_e}\right] \tag{5.2.9}$$

We assume the magnitude of the perturbation is small such that the quadratic term of the perturbed Hamiltonian may be neglected.

$$H_o = \left[\frac{\hat{p}^2}{2m_e} + V(\vec{r})\right] \tag{5.2.10}$$

$$H'(t) = \left[\frac{q}{m_e} \vec{A} \cdot \hat{p} \right] \qquad (5.2.11)$$

We then cast equation (5.2.11) into matrix notation

$$H'_{mn} = \left[\frac{q}{m_e} \vec{A} \cdot p_{mn} \right] \qquad (5.2.12)$$

where p_{mn} is the component of momentum. The vector potential for a plane wave is sinusoidal (Shiff, 1968).

$$\vec{A}(t) = \left| A_o \right| \cos(\vec{k} \cdot \vec{r} - \omega\, t + \alpha) \qquad (5.2.13)$$

Prior to substituting the expression for the vector potential into the system Hamiltonian we apply the dipole approximation. The dipole approximation assumes that the spatial dependence of the field may be neglected. We write the classical form of the electromagnetic vector potential where we have set the phase term equal to zero:

$$\vec{A}(t) = \left| A_o \right| \cos(\omega\, t) \qquad (5.2.14)$$

The relation between the vector magnetic potential and the electric field E is given by

$$\vec{E} = -\nabla V - \frac{\partial \vec{A}}{\partial t} \qquad (5.2.15)$$

where c is the speed of light. In free space equation (5.2.15) may be further reduced by neglecting the potential energy term (Cheng, 1993).

$$\vec{E} = -\frac{\partial \vec{A}}{\partial t} \qquad (5.2.16)$$

Notice that the direction of the vector potential is parallel to the electric field direction. We may subsequently convert the vector potential into terms of the electric potential

$$\vec{E}(t) = \omega \left| A_o \right| \sin(\omega t) = \left| E_o \right| \sin(\omega\ t) \qquad (5.2.17)$$

where I have introduced the field magnitude constant E_o.

$$\left| E_o \right| = \omega \left| A_o \right| \qquad (5.2.18)$$

Rewriting the vector potential using the more familiar electric field magnitude, as opposed to the vector potential magnitude, we obtain

$$\vec{A}(t) = \frac{1}{\omega} \left| E_o \right| \cos(\omega t) \qquad (5.2.19)$$

which may be substituted into the perturbation Hamiltonian matrix element of equation (5.2.12)

$$H'_{mn} = \frac{q}{\omega\, m_e} \left|E_o\right| \cos(\omega\, t) \cdot \left|p_{mn}\right| \tag{5.2.20}$$

Because of the dot product in equation (5.2.20) we must consider the direction of the electric field in relation to the momentum element. The perturbation Hamiltonian matrix element is non-zero only when the momentum is parallel to the electric field. In our MIM diode coupled to an antenna, the incident photons excite surface plasmons on the metal antenna. These surface plasmons, due to the resonant geometry of the antenna, transfer and focus the electric field of the incident photons across the oxide of the MIM diode. As a result, we have an electric field directed across the oxide of the MIM diode.

We calculate the momentum matrix element while at the same time converting from momentum space to real space.

$$\left\langle m \middle| p_x \middle| n \right\rangle = \left\langle m \right| \frac{i\, m_e}{\hbar} \left[H_o , \hat{x} \right] \left| n \right\rangle = i\, m_e \left|\omega_{mn}\right| \left|x_{mn}\right| \tag{5.2.21}$$

Inserting the momentum matrix element into the perturbation Hamiltonian matrix we obtain the complete perturbation Hamiltonian matrix element.

$$H'_{mn} = q \frac{\left|\omega_{mn}\right|}{\omega} \left|x_{mn}\right| \left|E_o\right| \cos(\omega\, t) \tag{5.2.22}$$

I assume that the relevant dipole distance x_{mn} in our MIM diode is the oxide thickness d_{ox}. As a final simplification the frequency difference between the two unperturbed states ω_{mn} is set equal to the incident radiation ω since all other transitions are improbable.

$$H'_{mn} = qV_{mn}\cos(\omega t) \tag{5.2.23}$$

The perturbation element is non-zero only on the diagonal terms. Consequently the electromagnetic field is equivalent to applying a sinusoidal voltage to the structure that modulates the unperturbed single electron energy levels in unison with the optical radiation field.

Tien and Gordon have solved this problem and shown that the expansion coefficients in equation (5.2.4) have a Bessel function dependence on the electric field strength

$$c_n = J_n\left(\frac{qV_{ph}}{\hbar\omega}\right) = J_n(\alpha) \tag{5.2.24}$$

where J_n is the nth order Bessel function. The perturbed electron wave function may be cast into the current voltage expression for the semiclassical illuminated J(V) curve (Tien, 1963):

$$J_{SCQM}(V_{bias}) = \sum_{n=-\infty}^{n=+\infty} J_n^2\left(\frac{qV_{ph}}{\hbar\omega}\right) J_{DARK}(V_{bias} + n\frac{\hbar\omega}{q}) \tag{5.2.25}$$

where the positive portion of the summation represents absorption and the negative portion represents stimulated emission.

At this point you may ask why I have gone into such detail to derive the semiclassical illuminated quantum mechanical illuminated J(V) curve. I did so to show the disjoint between classical rectification and hot-electron excitation (the photoelectric effect) within MIM diodes. Aversa has pointed out that the Tien and Gordon's model neglects field induced transitions (Aversa, 1996). These field induced transitions are hot-electrons. By neglecting the off-diagnal terms in the perturbation matrix, as is done in the semiclassical illuminated MIM diode theory, we are neglecting hot-electrons. Readers familiar with the derivation of Fermi's Golden rule will recognize that an opposite approach is taken in that derivation as the on-diagonal elements of the perturbation matrix are neglected instead of the off-diagonal elements. Consequently, the semiclassical illuminated J(V) theory is applicable when an antenna effectively couples the incident electromagnetic field across the oxide. In these situations hot-electron excitations are neglected.

Equation (5.2.25) is used to explain the photon stepping found in SIS (superconductor-insulator-superconductor) diodes in the presence of microwave radiation that was originally observed by Dayem and Martin (Dayem, 1962). The width of the resultant steps are equal to the photon energy and the height of the steps are dependent on the field strength or photon number.

iii. Photon Voltage

We now consider the strength of the electric field due to the incident electromagnetic radiation. The photon voltage V_{ph} in equation (5.2.25) is equal to the electric field produced by the photons times the oxide thickness (the dipole distance).

One method to estimate the electric field strength of the photons is by quantizing the electric field energy. We quantize the energy of the electromagnetic field by equating the energy of a classical electromagnetic wave to that of a harmonic oscillator

$$\frac{1}{2}\int \varepsilon_o \varepsilon_r \left|\vec{E}\right|^2 dVol = (n_{ph} + \tfrac{1}{2})\frac{\hbar\omega}{q} \qquad (5.3.1)$$

where n_{ph} is the photon number (Loudon, 2000). Because we assume the MIM diode is not coupled strongly to the vacuum field we neglect the ½ in equation (5.3.1).

$$\frac{1}{2}\int \varepsilon_o \varepsilon_r \left|\vec{E}\right|^2 dVol = n_{ph}\frac{\hbar\omega}{q} \qquad (5.3.2)$$

We find the photon voltage from equation (5.3.2) by solving for the electric field magnitude and multiplying by the oxide thickness to convert to a voltage.

$$V_{ph} = \sqrt{\frac{2\, n_{ph}\, \hbar\omega\, d_{ox}}{q\, Area\, \varepsilon_r\, \varepsilon_o}} \qquad (5.3.3)$$

The photon voltage is dependent on the number of photons n_{ph}, the dielectric constant of the oxide ε_o, and the photon confinement. We assume the photons are confined to the oxide of the MIM diode. Consequently, the photon voltage depends on the volume of the oxide in the MIM diode.

Calculating the voltage induced on the MIM diode by the electromagnetic field is now reduced to determining the number of photons collected by the antenna and focused upon the oxide.

In the MIM diode literature, which often comes from an RF antenna designer's perspective, the photon voltage is calculated from the power incident P_{in} on the MIM diode and the resistance of the diode R_{MIM}.

$$V_{ph} = \sqrt{2 P_{in} R_{MIM}} \tag{5.3.4}$$

This is reasonable for small photon energies and intensities but when dealing with visible photons it will be incorrect. This is because a range of effective resistances are spanned in the MIM diode J(V) curve. Reducing the range of resistances to a single R_{MIM} value will be incorrect.

Equation (5.3.3) does not rely on a fixed value of the MIM diode resistance to calculate the photon voltage. However, equation (5.3.3) still has its limitations imposed by the semiclassical treatment of the radiation and is best suited for electromagnetic fields composed of a large number of photons. This is due to three reasons. First, for large photon numbers the vacuum field may be neglected. Second, with a large number of photons there is a resemblance between the incident radiation to a classical electromagnetic wave with a determined magnitude and phase. There is an uncertainty relation between the magnitude and phase of the electromagnetic field that is sizeable for low photon numbers. This uncertainty relation is not derived from the orthogonality of measurable physical quantities but from geometric projections (Loudon, 2000). The uncertainty in magnitude and phase becomes negligible for large photon numbers. Third, equation (5.3.3) does not account for the resistance of the MIM diode. The power absorbed in the MIM diode is a function of the MIM diode resistance.

Our application for MIM diodes is solar energy conversion and consequently we wish to determine the value of the photon voltage produced by the sun. The solar spectrum may be approximated by a 5780 K blackbody.

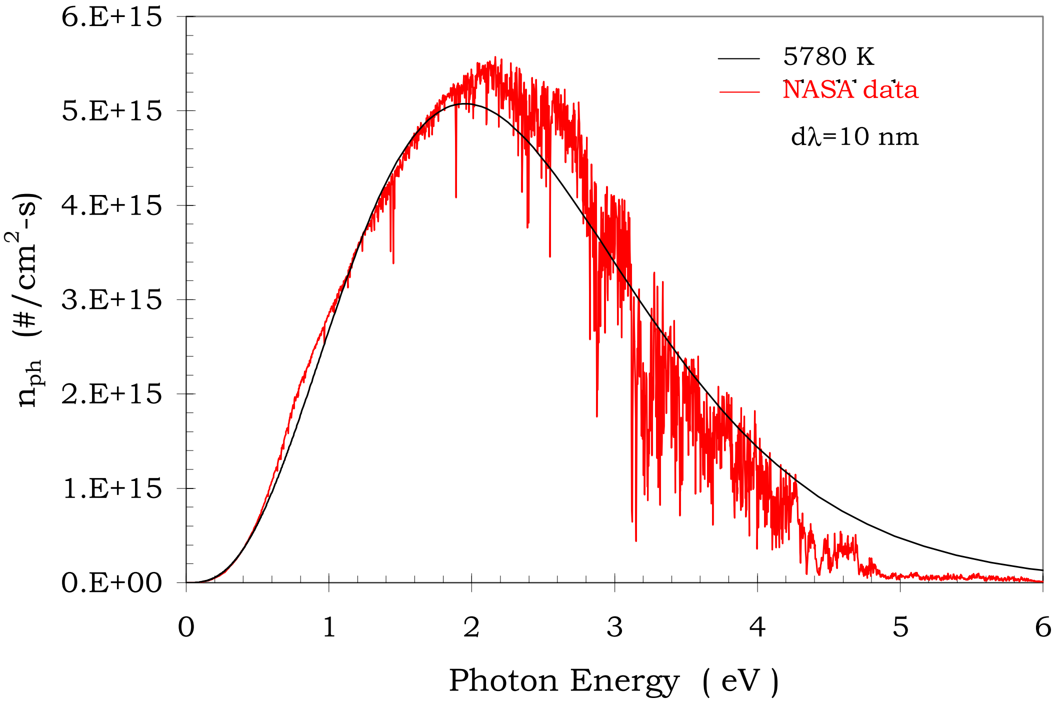

Fig. 5-1. *The number of photons per area per second vs photon energy for the solar spectrum. The smooth black curve is a 5780 K blacbody while the red curve is measured data obtained from NASA (Calahan, 1999).*

The total power delivered from a 5780 K black body representing the sun to the earth is calculated to be approximately 137 mW/cm^2. Due to atmospheric absorption, evident in the red curve in Figure (5-1), the actual power reaching the earth's surface is 100 mW/cm^2.

The relevant area for calculating the number of photons collected is not the area of the MIM diode but the area of the antenna aperture (Johnson, 1993)

$$A_e(\theta,\phi) = \frac{\lambda^2}{4\pi} G(\theta,\phi) \tag{5.3.5}$$

where G is then antenna gain. The antenna gain is a function of the antenna geometry. We shall set the gain equal to 1.64 (appropriate for a dipole antenna).

To determine the photon number n_{ph} in equation (5.3.3) we must specify a time interval. We shall assume the relevant time scale to count the number of incident photons is equal to the photon period. The photon number collected by the antenna may then be calculated.

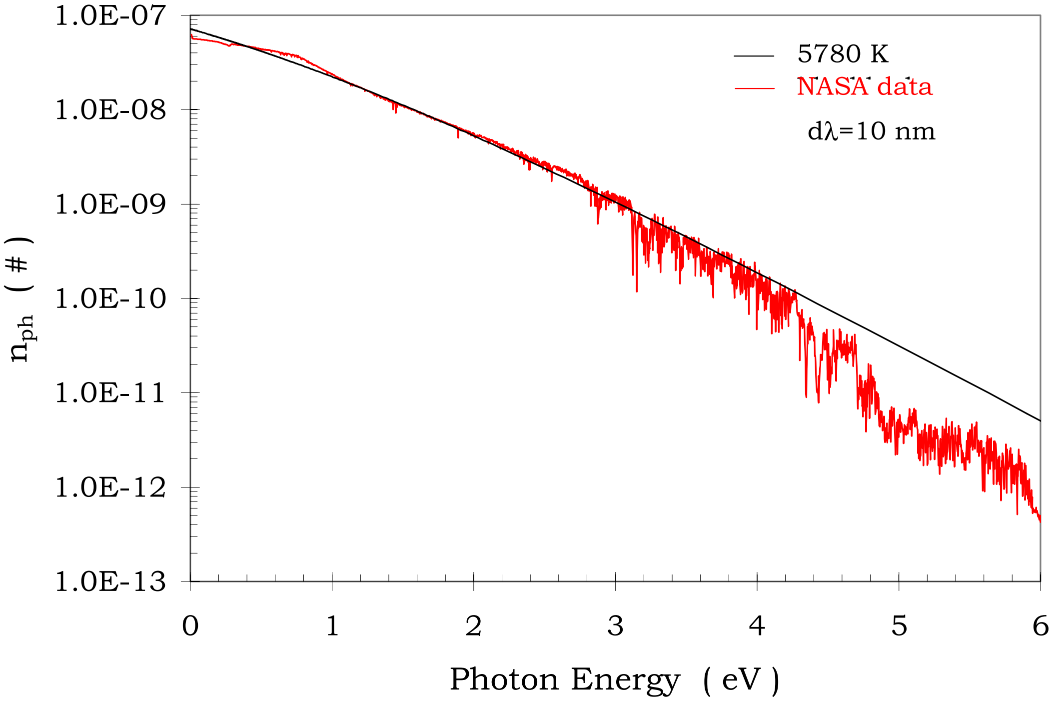

Fig. 5-2. *The number of photons in a 10 nm bandwidth delivered to the MIM diode by an antenna with a gain of 1.64 over a photon period plotted vs photon energy.*

The value of n_{ph} in Figure (5-2), for a bandwidth of 10 nm, is less than one for all photon energies. It is not possible to have a fraction of a photon and as a result we will set $n_{ph}=1$.

To calculate the illuminated J(V) curve we wish to determine the value of the argument of the Bessel function α in Equation (5.2.25), which is equal to $qV_{ph}/\hbar\omega$. A calculation of α as a function of photon energy is shown in Figure (5-3).

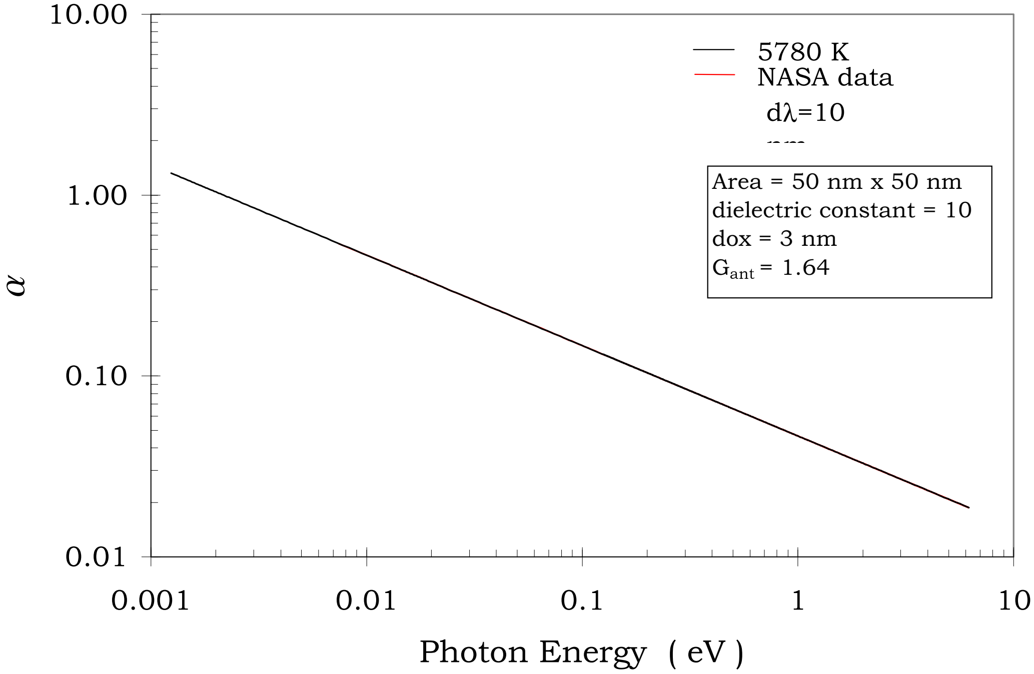

Fig. 5-3. *The value of the field strength α vs photon energy for a single photon.*

The physical significance of small α values is that multi-photon events are unlikely and the higher order terms of the Bessel function may be neglected.

With a photon number of one, treating the incident optical field as a classical wave may be inappropriate since we are not significantly above the vacuum field magnitude and have a sizeable uncertainty in the incident field's magnitude and phase. The expression for the illuminated J(V) curve, Equation (5.2.25), assumes an incident field with a known amplitude and phase. Foden has developed the quantum electrodynamic treatement of photon-assisted tunneling in which the electromagnetic radiation is quantized (Foden, 1998). Quantum electrodynamics includes interactions with the vacuum field and consequently spontaneous emission. The quantum electrodynamic treatment results in a displacement of the electrons energy, a spectrum that is asymmetric about n=0, and sideband amplitudes that are always greater than zero due to spontaneous emission. The spectrum derived by Foden is given by

$$\chi_{QED} = 2\pi \, Exp\left(-\zeta^2\right) \sum_{n=-\infty}^{\infty} \left(\delta(Energy - E_o - n\,E_{ph} + \Delta) \sum_{m=-\infty}^{n} J_m^2\left(2\zeta \sqrt{n_{ph}}\right) \frac{\zeta^{2(n-m)}}{(n-m)!} \right) \tag{5.3.6}$$

where the displacement Δ is given by

$$\Delta = \zeta^2 \, E_{ph} \tag{5.3.7}$$

Foden states that in the limit of a small coupling coefficient the QED result is equivalent to the semiclassical result. Using the dipole approximation we can show that

$$\zeta = \sqrt{\frac{d_{ox}}{2\,\hbar\omega\,\varepsilon_o\,\varepsilon_r\,Area}} \tag{5.3.8}$$

Multiplying the coupling coefficient by 2 sqrt(n_{ph}) we obtain α, the argument from the semiclassical Bessel function. Furthermore, in the limit the coupling coefficient goes to zero the remaining terms containing the coupling coefficient disappear resulting in the semiclassical spectral function.

$$\chi_{SCL} = 2\pi \sum_{n=-\infty}^{\infty} \delta(Energy - E_o - n\,E_{ph})\; J_n^2(\alpha) \tag{5.3.9}$$

Let's consider a specific example for a MIM diode having a oxide thickness of 1.5 nm, a size of 50 nm × 50 nm, and having a dielectric constant of ten. I calculate both the QED and semiclassical spectral functions for 0 through 3 photon excitations, with the arguments of the Dirac delta function equal to zero, and plot the result below for 0 to 10,000 2 eV photons incident upon the device.

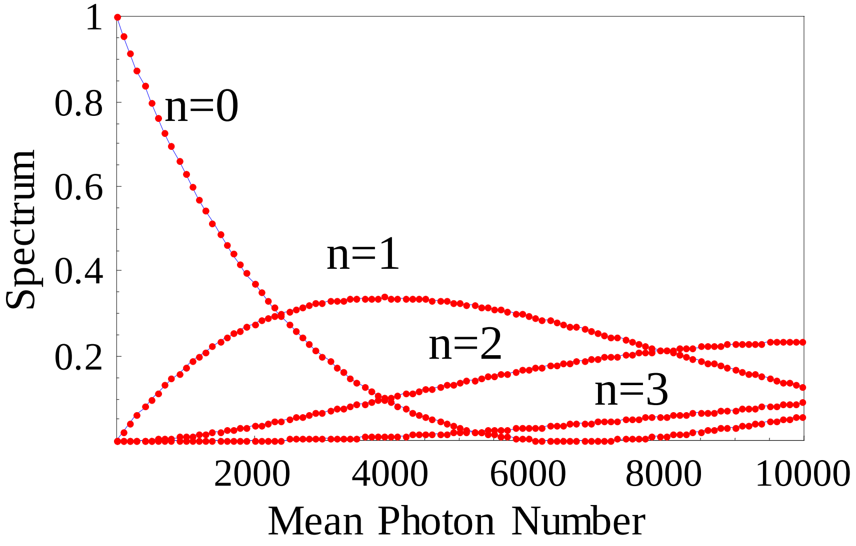

Fig. 5-4. *The semiclassical (red circles) and quantum electrodynamic (blue line) excitation spectra plotted as a function of the mean photon number. For our MIM diodes illuminated even with low intensities the theories are equivalent.*

For the situation depicted in Figure (5-4) the coupling coefficient is equal to 0.015 and the semiclassical case (red) is suitable for the entire range of mean number of photons.

Consequently, use of the simpler semiclassical formulation of photon assisted tunneling is valid for our MIM diodes even with low intensity illumination. If one desired to use the QED result, we could easily write the expression for the current vs voltage curve for an illuminated MIM diode directly from equation (5.3.6)

$$J_{QED}(V_{bias}) = \sum_{n=-\infty}^{n=n_{ph}} \left[J(V_{bias} + n\tfrac{\hbar\omega}{q} - \zeta^2 E_{ph}) \sum_{m=-\infty}^{n} J_m{}^2\left(2\zeta\sqrt{n_{ph}}\right) Exp\left(-\zeta^2\right) \frac{\zeta^{2(n-m)}}{(n-m)!} \right] \quad (5.3.10)$$

iv. Efficiency Estimates

Conversion of the solar spectrum using conventional semiconductor solar cells is limited to around 30 % (Fonash, 1981). This is linked to the fact that semiconductor based solar cells function by the generation of free electron hole pairs. A photon incident upon the solar cell excites an electron across the band gap of the semiconductor. Low energy photons do not possess sufficient energy to excite electrons across the bandgap (and multiphoton events have a low probability) and as a result we are unable to harvest these photons. High energy photons excite the electrons across the bandgap and high into the conduction band. These photoexcited hot-electrons thermalize to the conduction band edge resulting in a loss of the excess energy. As a result, only photons with energies equal to the bandgap of the semiconductor are efficiently harvested.

In MIM diodes that harvest the incident photons by rectification rather than by free carrier generation we have the theoretical possibility for nearly 100 % conversion efficiency.

Consider an illuminated MIM diodes J(V) curve in which photon stepping is evident.

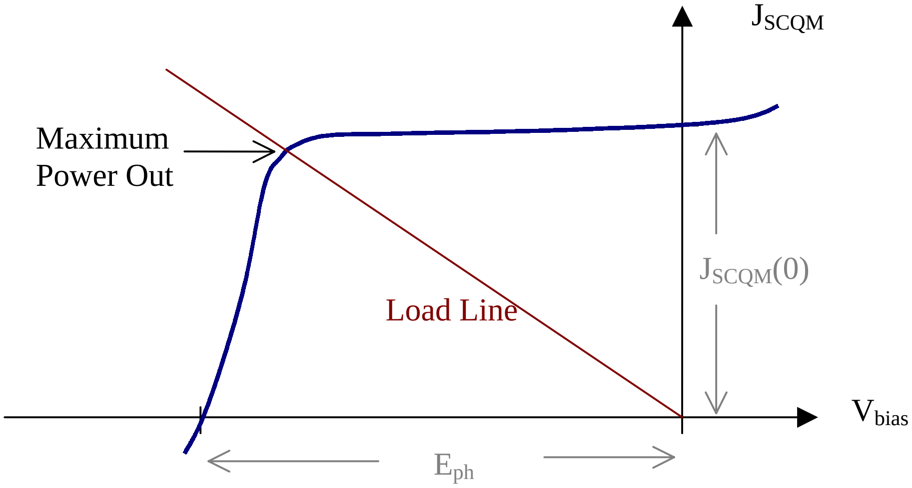

Fig. 5-5. *Second quadrant of an MIM diode J(V) curve illuminated such that a single photon step is. Using a load line the maximum power out of the diode may be calculated.*

The width of the photon step is equal to the photon energy E_{ph} or ħω/q (assuming the forward bias turn-on voltage is much less than $q \cdot E_{ph}$) and the height of the step is proportional to the field strength. I calculate the maximum power extracted from the illuminated MIM diode by using a load line as applied to semiconductor solar cells (Fonash, 1981). With photon stepping the maximum power out of the MIM diode is approximately equal to the photon energy times the current produced at zero volts under illumination.

The responsivity of an MIM diode (usually given in amps per watt) has been shown to be equal to

$$\Re(V) = \frac{\Delta J_{DC-ILLUM}}{\frac{1}{2} V I_{\omega}} = \frac{q}{\hbar\omega}\left[\frac{J(V+\frac{\hbar\omega}{q}) - 2J(V) + J(V-\frac{\hbar\omega}{q})}{J(V+\frac{\hbar\omega}{q}) - J(V-\frac{\hbar\omega}{q})}\right] \tag{5.4.1}$$

where $\Delta J_{DC\text{-}ILLUM}$ is the change in DC current under illumination (Tucker, 1985). For a sufficiently nonlinear MIM diode where $J(V+q \cdot E_{ph}) >> -J(V-q \cdot E_{ph})$ the maximum value is the inverse of the photon energy. The quantum efficiency, equal to the responsivity multiplied by the photon energy, reaches 90 % for an unbiased MIM diode when $J(q \cdot E_{ph})$ is 19 times larger than $-J(-q \cdot E_{ph})$.

We may express the current density $J_{SCQM}(V)$ as a function in terms of the responsivity $\Re(V)$. Consequently, the power out may then be written as

$$P_{out} = E_{ph} \cdot J_{SCQM}(0) \cdot Area = E_{ph}\,\Re(0)\,P_{in} = E_{ph}\frac{1}{E_{ph}}P_{in} = P_{in} \tag{5.4.2}$$

which is to say a sufficiently nonlinear MIM diode may harvest photons over a broad range of photon energies with 100 % efficiency.

Given the motivation to pursue MIM diodes for higher efficiency solar energy conversion it is reasonable to more accurately calculate the power out of an illuminated MIM diode. In doing so, we shall find that there is a minimum current density required to efficiently harvest photons with MIM diodes.

As I have illustrated in Figure (5-5) with photon stepping the maximum power out of the MIM diode is equal to the photon energy times the current magnitude at zero volts

$$P_{out} = E_{ph} \cdot J_{SCQM}(0) \cdot Area \tag{5.4.3}$$

where the photon energy E_{ph} has the units of electron volts and the Area is that of the MIM diode. I have assumed a photon step such that J_{SCQM}(-Eph)=J_{SCQM}(0). The power incident is simply the energy delivered per time. Assuming a single photon that is “rectified” in a single period we obtain

$$P_{in} = \frac{qE_{ph}}{T_{ph}} \tag{5.4.4}$$

where T_{ph} is the time period of the photon. The efficiency, in percent, is the power out divided by the power in.

$$\eta = \frac{P_{out}}{P_{in}} = 100\frac{J_{SCQM}(0) \cdot Area \cdot T_{ph}}{q} \tag{5.4.5}$$

If the argument of the Bessel function in J_{SCQM} is near zero, we need only consider the zero and first order Bessel function terms. By performing a Taylor series expansion of the Bessel function about a zero value argument and retaining only the first terms we approximate the illuminated current.

$$J_{SCQM}(0) \approx \frac{1}{4}\left(\frac{qV_{ph}}{E_{ph}}\right)^2 \left[J_{DARK}(-E_{ph}) + J_{DARK}(+E_{ph})\right] \tag{5.4.6}$$

For J_{SCQM} to have a non-negligible value $J(+E_{ph}) >> J(-E_{ph})$ which is to say the MIM diode is nonlinear over a voltage span equal to two times the photon energy. In an ideal diode, $J(-E_{ph})$ much less than $J(+E_{ph})$ and may be neglected.

$$J_{SCQM}(0) \approx \frac{1}{4}\left(\frac{qV_{ph}}{E_{ph}}\right)^2 \left[J_{DARK}(+E_{ph})\right] \tag{5.4.7}$$

We now estimate the current magnitudes required for high-efficiency direct conversion. We first insert the approximate illuminated current equation (5.4.7) into the efficiency expression (5.4.5).

$$\eta \approx \frac{100}{4q}\left(\frac{qV_{ph}}{E_{ph}}\right)^2 \left[J_{DARK}(+E_{ph}) \cdot Area\right] T_{ph} \tag{5.4.8}$$

We assume 100 % efficiency and solve for the required current density at a bias voltage equal to the energy of a single photon divided by q.

$$J_{DARK}(E_{ph}) \approx \frac{4q}{Area\,T_{ph}}\left(\frac{E_{ph}}{qV_{ph}}\right)^2 \tag{5.4.9}$$

We estimate the photon voltage for a single photon confined to the oxide d_{ox} of the MIM diode using equation (5.4.3). The period of the photon may also be recast in terms of the photon energy (still in eV).

$$T_{ph} = \frac{2\pi\hbar}{q\,E_{ph}} \tag{5.4.10}$$

Inserting the equation (5.4.10) for T_{ph} and equation (5.4.3) for V_{ph} into the minimum current requirement equation (5.4.9) we obtain an estimate of the current magnitude required for high efficiency direct conversion.

$$J_{DARK}(E_{ph}) \approx \frac{q\,\varepsilon_o\varepsilon_r\,E_{ph}{}^{2}}{\hbar\,d_{ox}\,\pi} \tag{5.4.11}$$

We shall assume the following values to obtain a numerical value for the minimum current density required to efficiently harvest the energy of a single photon:

$d_{ox} = 3$ nm $\quad \varepsilon_r = 4.5 \quad E_{ph} = 2.5$ eV ($\lambda = 500$ nm)

These values result in a required dark current density value of $J_{DARK}(2.48)=39.5 \times 10^{12}$ A/m^2 or 39.5×10^{8} A/cm^2. For 1 eV photons and a 2 nm barrier the required current density drops to approximately 10^{8} A/cm^2.

At this point I have established requirements for MIM diodes used for efficiently harvesting photons. To obtain high current densities we need a low resistance diode to efficiently harvest photons. I have assumed efficient coupling between the incident photons to the antenna and between the antenna and the diode. In addition to the current magnitude requirements of the MIM diode, the diode must also be sufficiently nonlinear in order to rectify the incident electromagnetic radiation.

This assumption for the minimum current density relies heavily upon the assumption that the photon energy is delivered over a single period. Alternatively we could estimate the current density requirements from the classical arguments presented in section IV. Assuming that the antenna resistance is 377 ohms we may calculate the required capacitance to ensure that $\omega RC = 1$. From the capacitance, assuming a dielectric constant of 4.5, we may estimate the area of the MIM diode to achieve the required capacitance. I then approximate the MIM diode resistance as the photon voltage divided by the current of the MIM diode produced at the photon voltage (an arguably generous assumption) and set it equal to the antenna resistance. The required current density of the MIM diode may then be calculated. The estimate of the required current density is shown in Figure (5-6) for the case where α is equal to unity.

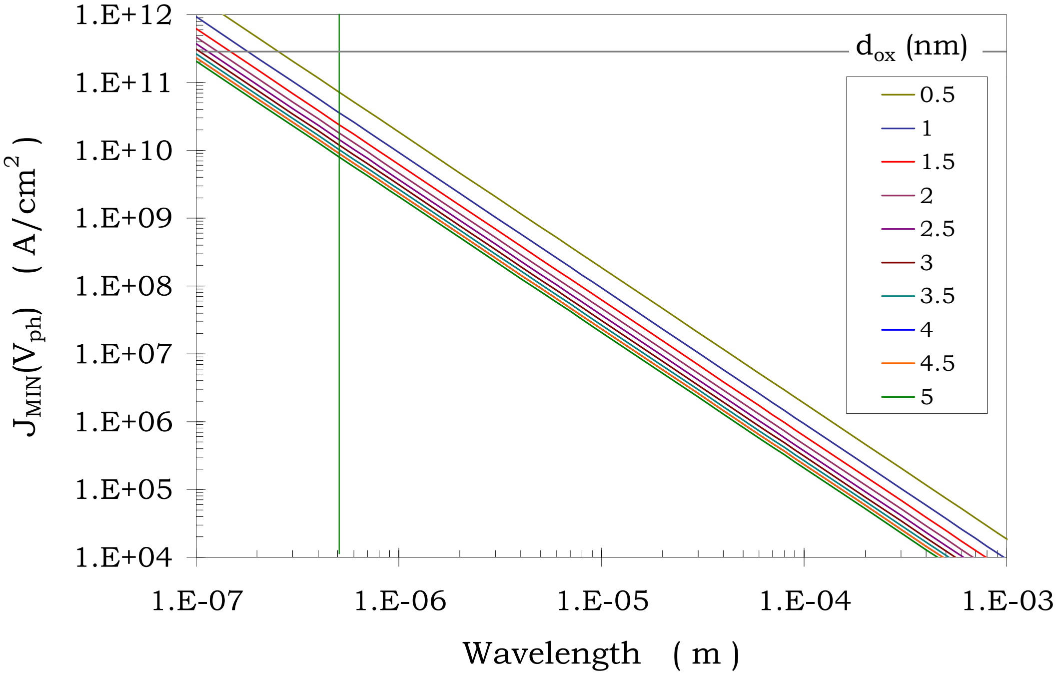

Fig. 5-6. *Estimate of the minimum required current density using RC time constant arguments.*

The minimum current density is even higher then estimated in Equation (5.4.12). The gray line indicates the density of states limit of the maximum current density. The density of states limit is calculated by setting the electron tunneling probability equal to one and using a unity effective mass. Consequently, the estimates of the required current density are for short enough wavelengths beyond what could be achieved with an MIM diode. The required current densities are simply estimates. If the required current density is not achieved the efficiency will suffer. Ultimately, the required current density will depend upon the specific impedance of the antenna.

v. Improved MIM Diode

I have shown that for efficient energy conversion we need an MIM diode with both high current density and high nonlinearity. I will now optimize the MIM diode with these two stipulations in mind. Then, with the improved MIM diode I will calculate the solar energy conversion efficiency. In these calculations I assume the diode is able to keep up with the frequency of the incident radiation and is perfectly matched to the antenna.

For MIM diodes, barrier heights between the metal and oxide are typically less than 2 eV. Consider green photons (2.5 eV) and the energy band diagram of an MIM diode with barrier heights less then 2 eV. This MIM diode, with an equivalent applied bias of positive and negative 2.5 V, enters the Fowler-Nordheim tunneling regime.

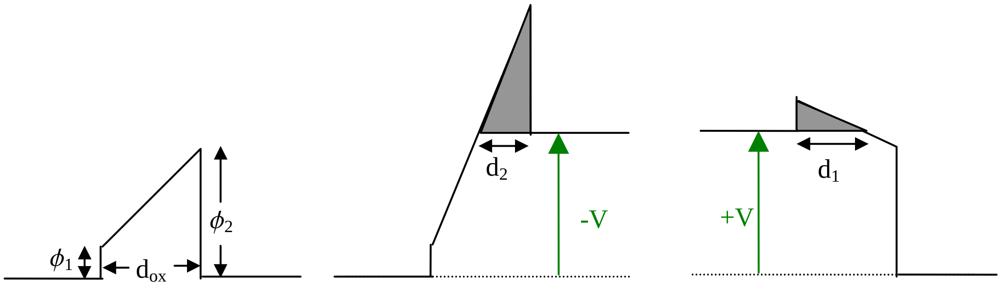

Fig. 5-7. – *Energy band diagrams for an MIM diode. The energy band diagram for the MIM diode on the left is with no applied bias, the center diagram has a large negative applied bias, and the right diagram has a large positive applied bias. The shaded region of the band diagram depicts the region responsible for limiting the electron tunneling probability for electrons located at the Fermi level.*

A majority of the electron flow in MIM diodes occurs near the Fermi level where the electron concentration and tunneling probability are the highest. The asymmetry in the MIM diode, assuming metals with nearly equivalent electron densities, will be due to the difference in tunneling probability. The tunneling probability at high bias voltages has an analytical solution due to the triangular shape of the barrier (shaded region in Figure (5-7))

$$T(E) = \exp\left(-\frac{4d\sqrt{2m_o q\phi}}{3\hbar} \right) \tag{5.5.1}$$

where T is the tunneling probability, E is the energy of the tunneling electron, m_o is the electron mass, ϕ is the barrier height, and d is the distance the electron must tunnel. The quantities in equation (5.4.1) may be related back to the oxide thickness, applied voltage, and barrier heights in the MIM diode through trigonometric considerations.

$$d_1 = d_{ox}\frac{\phi_1}{V+\phi_1-\phi_2} \qquad d_2 = \frac{\phi_2}{V+\phi_2-\phi_1} \tag{5.5.2a,b}$$

I next calculate the ratio of the tunneling probability at a positive applied voltage to the tunneling probability at an equivalent negative applied voltage using equation (5.5.1) in conjunction with equations (5.5.2a,b). The applied voltage V is set equal to the photon energy. Figure (5-8) shows a plot of the results for a 2 eV photon and 2 nm thick oxide.

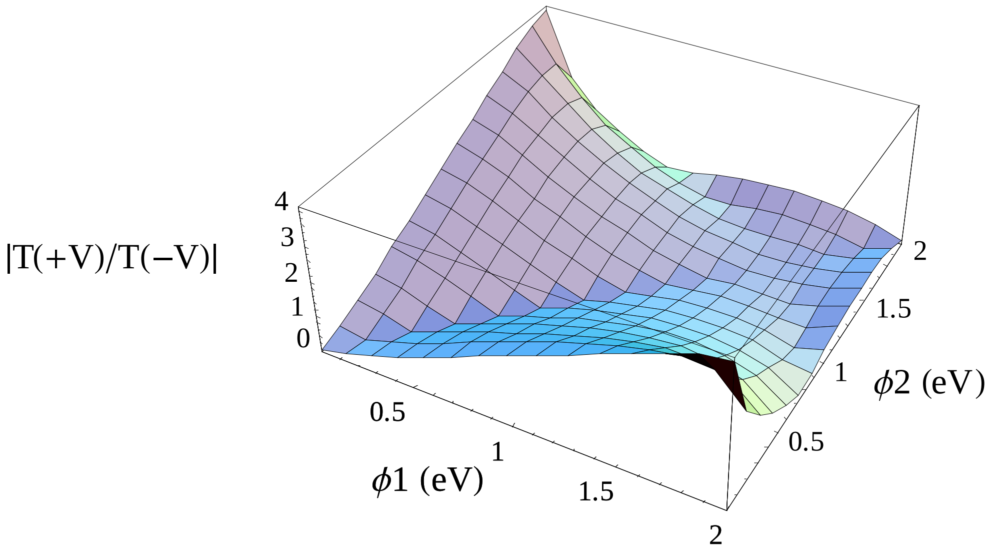

Fig. 5-8. – *A plot of the asymmetry in the electron tunneling probability for a positive applied bias voltage divided by the electron tunneling probability at an equivalent negative applied bias for a 2 eV photon and a 2 nm thick oxide over a range of MIM barrier heights.*

From Figure (5-8) we see that in order to obtain a large asymmetry in tunneling probabilities we should choose one barrier as small as possible and the other barrier as large as possible. This conclusion can be visualized by inspecting the band diagrams in Figure (5-7). The magnitude of the tunneling ratio in Figure (5-8) changes with different oxide thicknesses and photon energies. However, the relation between the two barrier heights remains unchanged.

For MIM diodes, a small barrier is provided by Nb and its native oxide (0.01 eV) so I will choose ϕ_1 as 0.01 eV. I then calculate the asymmetry for various oxide thicknesses and ϕ_2 values shown in Figure (5-9).

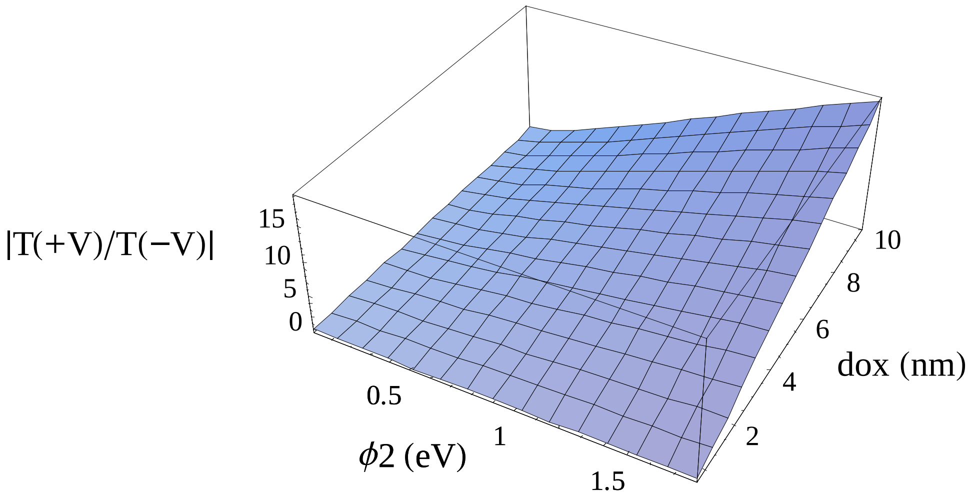

Fig. 5-9. – *A plot of the asymmetry in the electron tunneling probability for positive applied bias voltage divided by the electron tunneling probability at an equivalent negative applied bias for a range of barriers heights between metal 2 and the native oxide and oxide thicknesses. The photons are 2 eV. The barrier between metal 1 and the oxide is chosen as 0.01 eV.*

We find that the largest asymmetry occurs with large ϕ_2 values and a thick oxide. I also calculated the asymmetry for various photon energies and found that the magnitude of the asymmetry increases with larger photon energies but the shape remains the same.

We have reached a tradeoff in MIM optimization. Thick oxides and tall barriers, which increase asymmetry, also result in a decrease in the current magnitude. A low current magnitude will decrease our ability to efficiently rectify the incident photon due to antenna-diode impedance mismatching and the minimum current magnitude estimated for efficient conversion. Consequently, we must find the structure that provides the required current density with as much asymmetry as possible.

To find the optimum structure I set ϕ_1 equal to 0.01 eV. This small barrier will maximize the current density and it will also afford us the largest difference in barrier heights. I then calculated the J(V) curve for MIM diodes with oxide thicknesses of 0.5, 1.0, and 1.5 nm with ϕ_2 ranging from 0.01 to 3.81 eV.

The results for a MIM diode with a 0.5 nm thick oxide is shown in Figure (5-10).

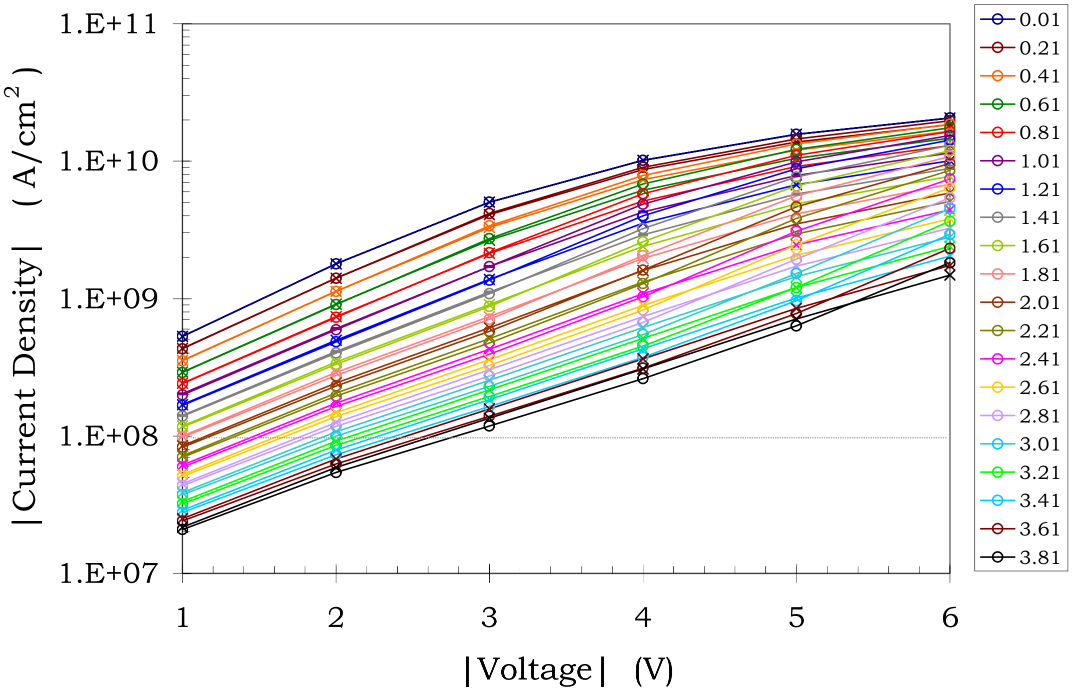

Fig. 5-10. *– The current density vs voltage for an MIM diode with a 0.5 nm thick oxide and a 0.01 eV barrier on the left. The right barrier height is varied from 0.01 to 3.81 eV. The current density needs to be greater than* 10^8 *A/cm*^{2} *for maximum conversion efficiency. The circles are for positive applied bias and the × is for negative applied bias. For small barrier heights the asymmetry is negligible due to direct tunneling and the dash lies below the circle.*

The circles are for positive applied bias, while ×, hidden below the circle for small ϕ_2 values, indicate the negative applied bias trace. We require current densities of at least 10^8 A/cm^2 for efficient solar energy conversion. To obtain the required current densities for photons as small a 1 eV we require a MIM diode that has a 0.5 nm thick barrier to have a ϕ_2 value less that 1.61 eV.

The thin barrier results in significant direct tunneling and as a result little asymmetry between positive and negative applied biases. The calculated asymmetry is plotted in Figure (5-11).

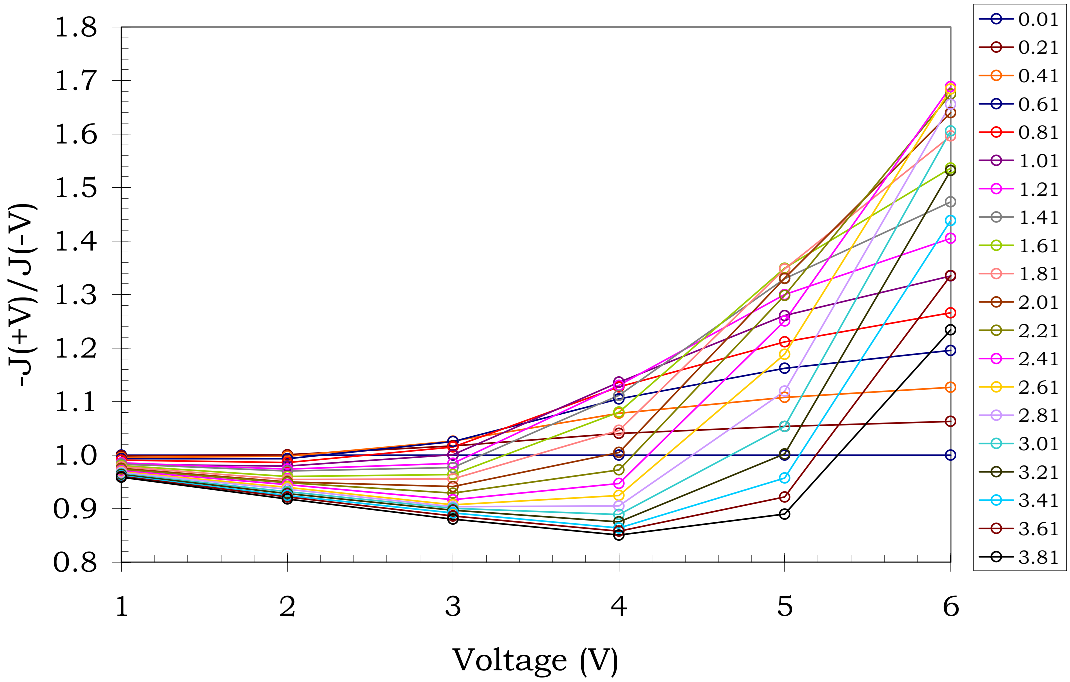

Fig. 5-11. – *The magnitude of the ratio between the current density at +V divided by the current density at -V vs. voltage for a MIM diode with a 0.5 nm thick oxide and a 0.01 eV barrier on the left. The right barrier height is varied from 0.01 to 3.81 eV.*

For the 1.61 eV barrier we have a ratio of 1.02 in current magnitude. Recall from subsection iv that a ratio of 19 is required for 90 % quantum efficiency. The asymmetry for this 0.5 nm thick oxide barrier is less than 2 even for 6 eV photons and a 3.81 eV barrier height.

We will require a thicker oxide to increase the asymmetry. I have repeated the above calculations for a 1 nm barrier and the results are plotted in Figure (5-11) and Figure (5-12).

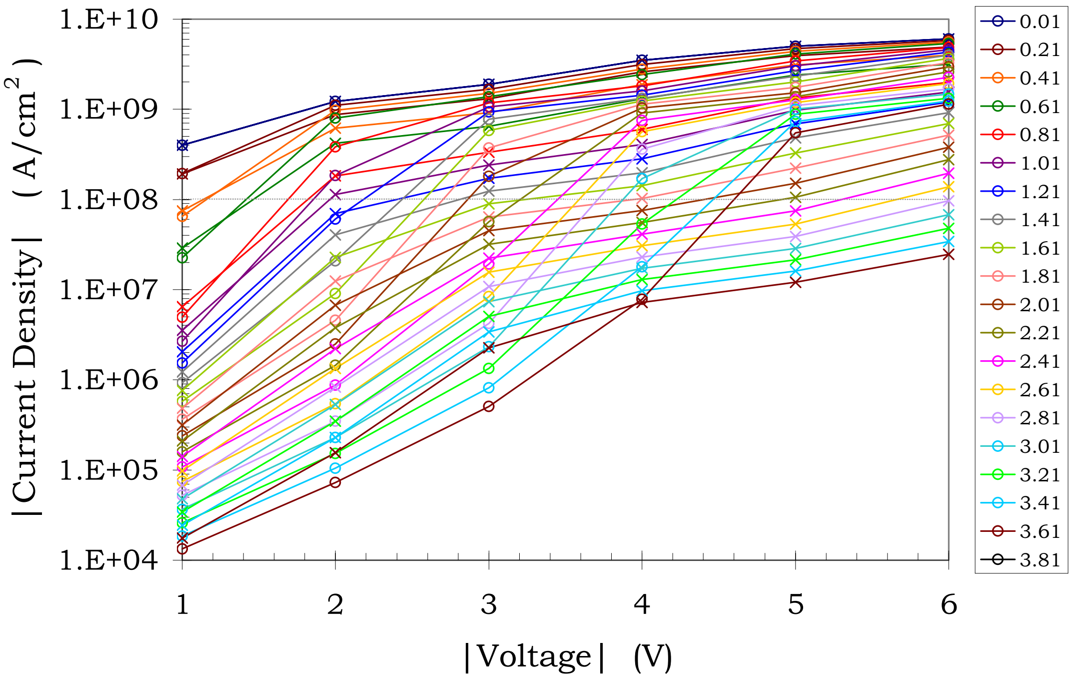

***Fig. 5-12.** - The current density vs voltage for an MIM diode with a 1.0 nm thick oxide and a 0.01 eV barrier on the left. The right barrier height is varied from 0.01 to 3.81 eV. The current density needs to be greater than 10^8 A/cm^2 for maximum conversion efficiency. The circles are for positive applied bias and the × is for negative applied bias. For small barrier heights the asymmetry is negligible due to direct tunneling and the dash lies below the circle.*

The 1.0 nm thick barrier results in a current density over 4 orders of magnitude lower than the 0.5 nm thick barrier for large ϕ_2 values. We see from Figure (5-11) that for the 1 nm thick barrier, harvesting 1 eV photons, the largest value of ϕ_2 we may use is 0.21 eV to obtain a current magnitude of 10^8 A/cm^2.

The ratio of the current magnitude at +V divided by that at –V is plotted in Figure (5-13).

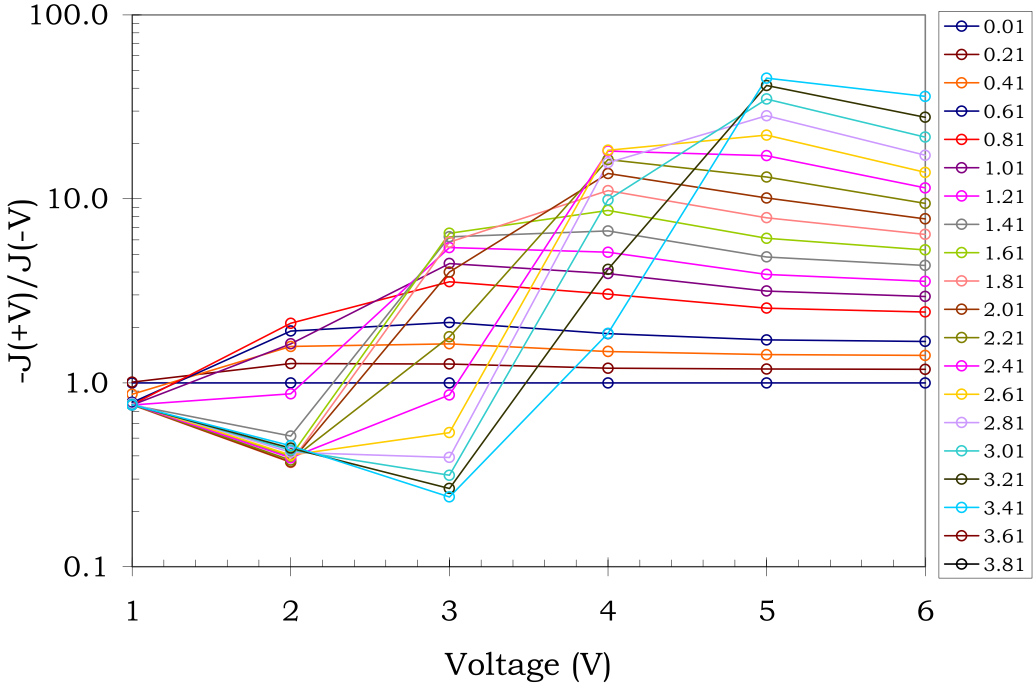

Fig. 5-13. *- The magnitude of the ratio between the current density at +V divided by the current density at -V vs. voltage for a MIM diode with a 1.0 nm thick oxide and a 0.01 eV barrier on the left. The right barrier height is varied from 0.01 to 3.81 eV.*

The current asymmetry does reach an order of magnitude in the MIM diode with a 1 nm barrier. However, for the 0.21 eV barrier height, the ratio is near unity.

Increasing the barrier thickness to 1.5 nm we find the value of ϕ_2 can not be greater than 0.41 eV to prevent the current density from dropping below 10^8 A/cm^2 as shown in Figure (5-14).

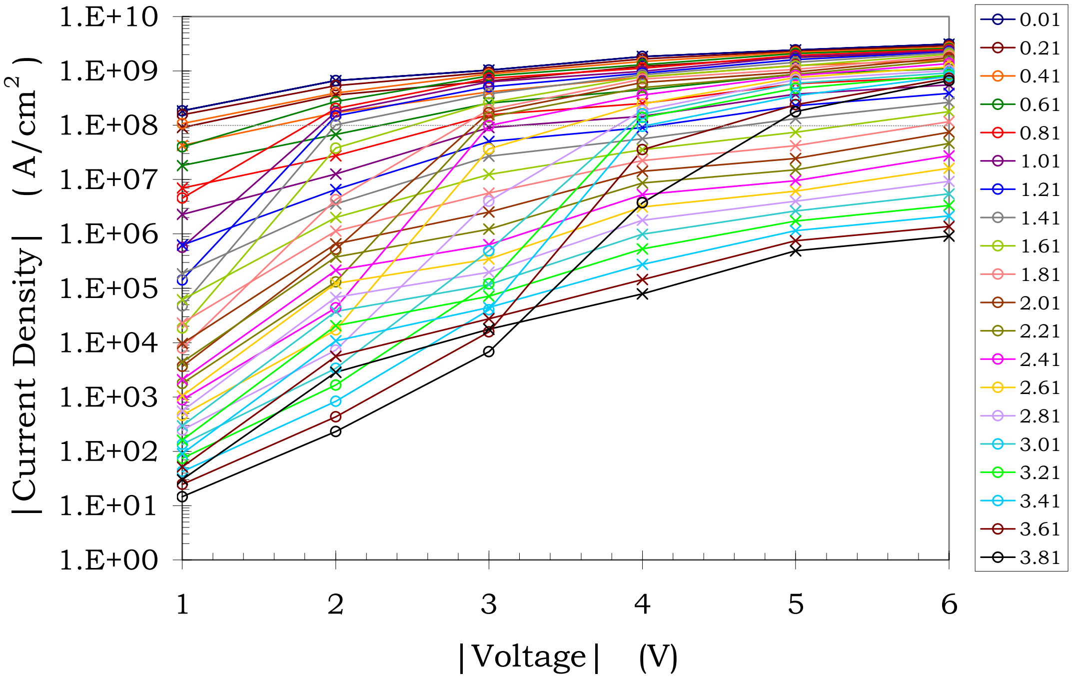

Fig. 5-14. *- The current density vs voltage for an MIM diode with a 1.5 nm thick oxide and a 0.01 eV barrier on the left. The right barrier height is varied from 0.01 to 3.81 eV. The current density needs to be greater than* 10^8 *A/cm*^{2} *for maximum conversion efficiency. The circles are for positive applied bias and the × is for negative applied bias. For small barrier heights the asymmetry is negligible due to direct tunneling and the dash lies below the circle.*

Calculating the asymmetry of the MIM diode with a 1.5 nm thick barrier in Figure (5-15) we find that the asymmetry can reach three orders of magnitude with large ϕ_2 values.

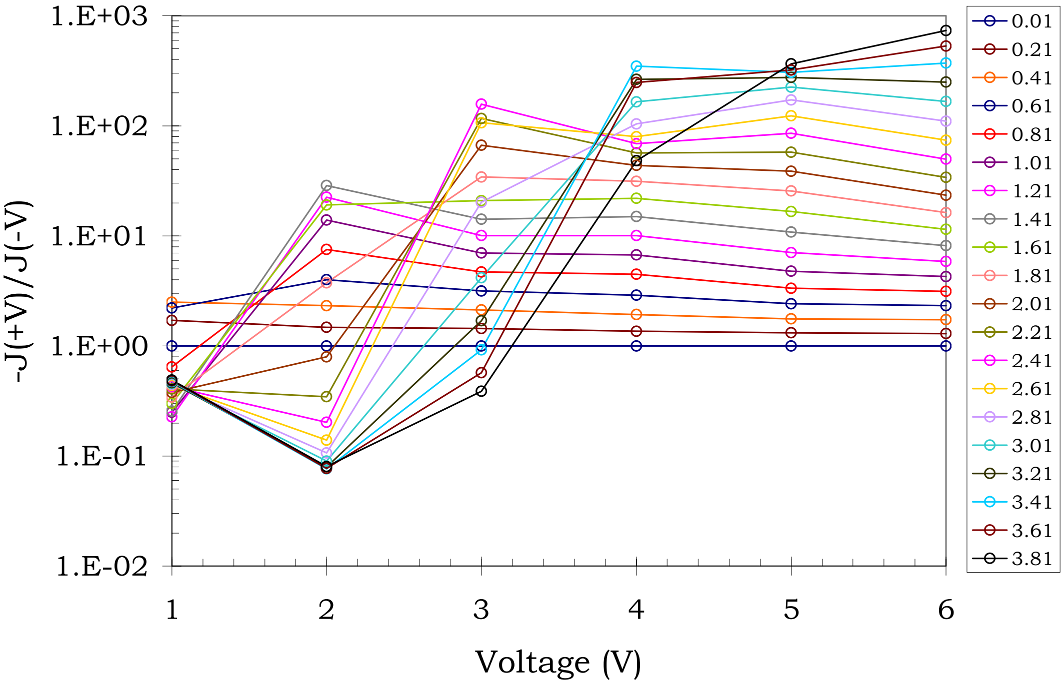

Fig. 5-15. – *The magnitude of the ratio between the current density at +V divided by the current density at -V vs. bias voltage for an MIM diode with a 1.5 nm thick oxide and a 0.01 eV barrier on the left. The right barrier height is varied from 0.01 to 3.81 eV.*

The asymmetry for the MIM diode with ϕ_2 = 0.41 eV is 2.5 and is nearly constant across the solar spectrum.

The MIM diode that has a sufficiently high current density with a non-unity asymmetry has the parameters d_{ox} = 1.5 nm, ϕ_1 = 0.01 eV, and ϕ_2 = 0.41 eV. I subsequently calculated the J(V) curve in voltage increments of 0.01 V on this improved MIM diode structure.

I next calculate the conversion efficiency for this improved MIM diode structure. I assume a diode area of 50 nm x 50 nm with an oxide dielectric constant of 10. The power out is calculated from $J_{SCQM}(V)$ equation (5.2.25) by locating the maximum of $-V\cdot J_{SCQM}(V)$ within the second quadrant. I then repeat the power calculation over a range of field strengths.

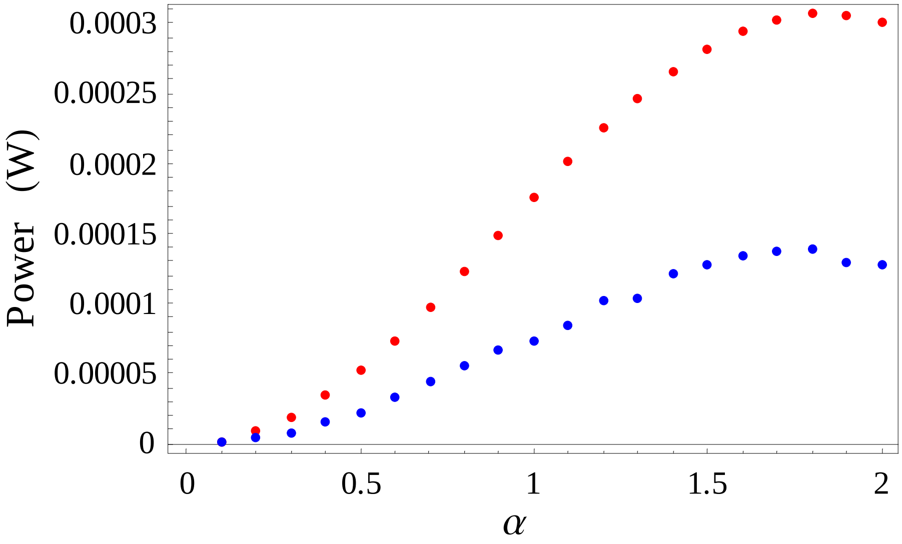

Fig. 5-16. *– The DC power out of the MIM diode as a function of the photon field strength. The lower blue curve includes the self bias imposed on the MIM diode by the field while the upper red curve neglects this effect.*

In Figure (5-16) the red curve neglects the self bias imposed on the MIM diode by the incident radiation (appropriate for a load in parallel with the MIM diode) while the blue curve includes this effect (appropriate for a load in series with the MIM diode). For $\alpha>1$ multiphoton events become increasingly important. The peak in Figure (5-16) is due to neglecting these multiphoton events. The self bias is included by iterating between the DC voltage out of the illuminated diode and the applied bias voltage (set equal to the open circuit voltage) until a self consistent solution is obtained. For a real load, the self-bias voltage will be less than the open circuit voltage and the power will lie between the red and blue curve. We find that the conversion efficiency will be low for low incident field strengths. In an MIM diode solar cell the field intensities are increased by increasing the photon number (large area focusing) or increasing the photon confinement (smaller MIM diode).

I next calculate the conversion efficiency of the MIM diode, on a single photon basis, across the solar spectrum, as shown in Figure (5-17).

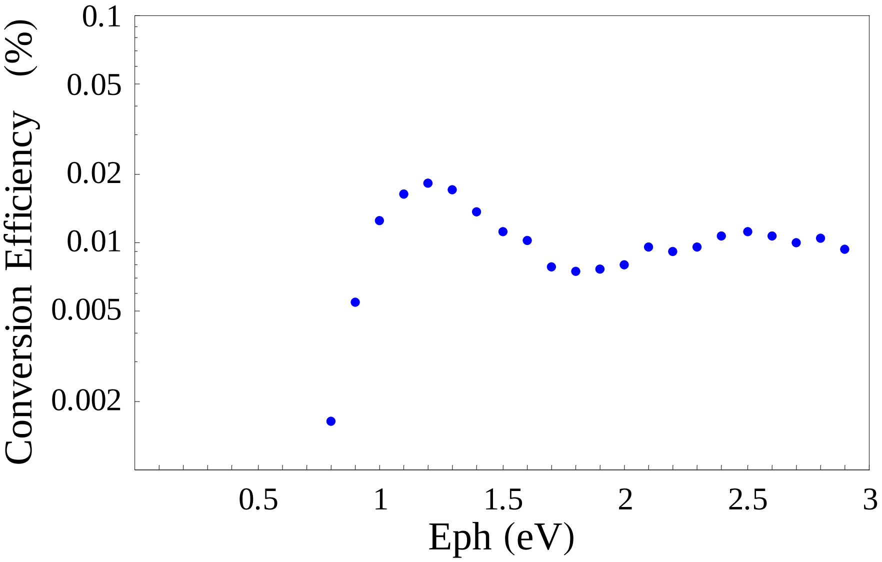

Fig. 5-17. *– The conversion efficiency for the improved MIM diode over a range of incident photon energies. The self-bias imposed on the MIM diode by the incident photon is included.*

The maximum conversion efficiency is around 0.02 % for 1 eV and greater photons.

I then calculate the quantum efficiency, the responsivity times the photon energy, of the MIM diode at zero bias across the solar spectrum. I did not take absolute values of the responsivity in the plot resulting in the negative values of quantum efficiency.

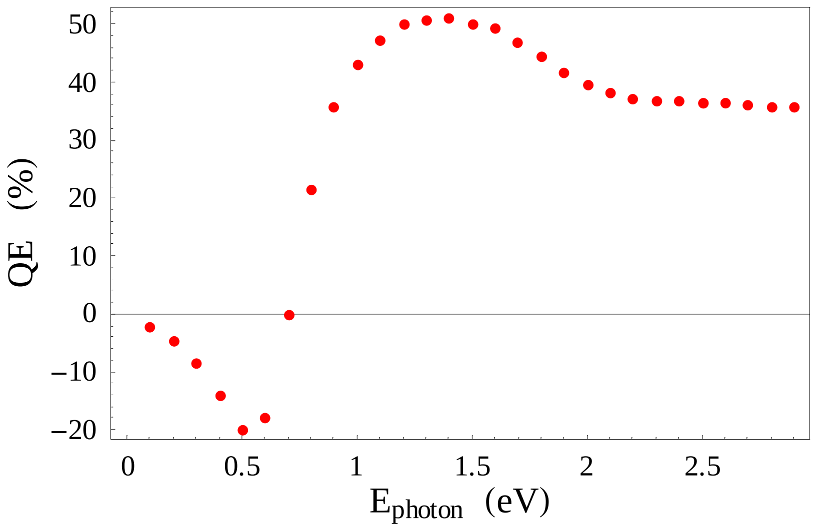

***Fig. 5-18. –** The quantum efficiency of the MIM diode vs photon energy. The negative values represent rectification reversal.*

We find in Figure (5-18) that the quantum efficiency peaks at 50 %, though the overall conversion efficiency is much less than this value. Consequently, the MIM diode is only partially limited by the low asymmetry.

The dominant limitation to high conversion efficiency with MIM diodes is the low field strengths on the MIM diode. We estimate the field strength $\alpha = qV_{ph}/E_{ph}$ as a function of photon energy across the solar spectrum for our improved MIM diode.

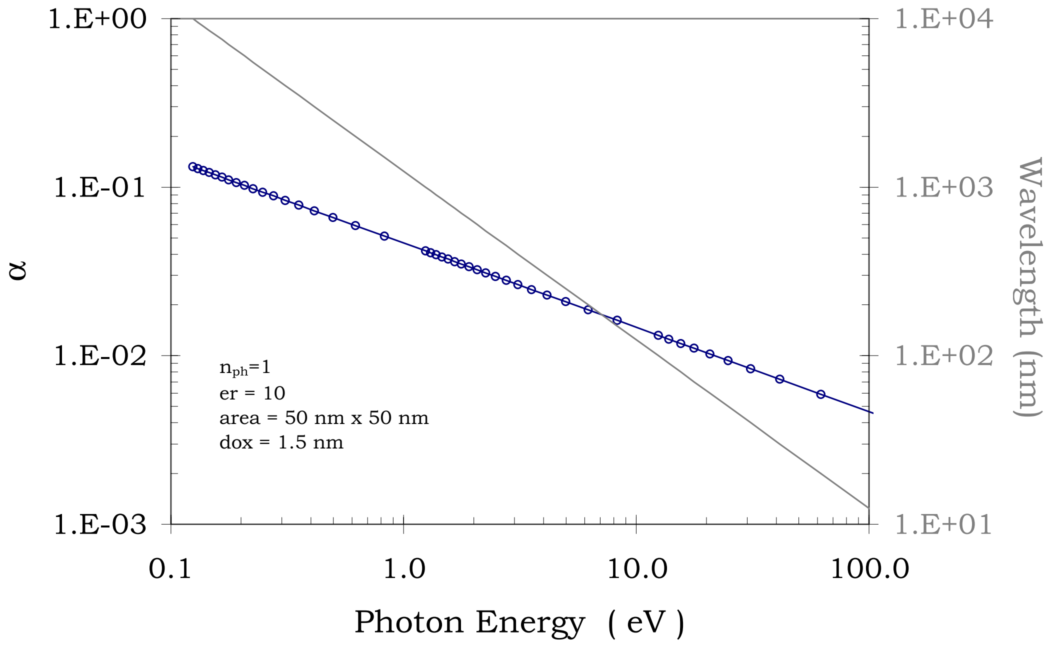

Fig. 5-19. – *Estimate of the field strength* α *vs. photon energy for the improved MIM diode. The plot also includes the conversion between photon energy and wavelength on the right axis.*

In Figure (5-19) we find that α is less than 0.1 for a majority of the solar spectrum. Increasing α by MIM geometry is only marginally effective since α increases as the square root of $d_{ox}/(\text{Area } \epsilon_r)$ where d_{ox} is the oxide thickness, Area is that of the MIM diode and ϵ_r is the dielectric constant of the oxide.

To obtain higher efficiencies the photon number must be increased. Since V_{ph} and consequently α increase with the square root of the photon number (Equation (5.3.3)), we need to increase the photon number focused upon the MIM diode by more than three orders of magnitude to increase α to unity.

However, we may have already overestimated V_{ph} by neglecting the MIM diode resistance and assuming the photon is rectified in a single photon period. A third way to calculate V_{ph} is from the power incident upon the MIM diode by the solar spectrum over some bandwidth. The current dissipated in a MIM diode at the oscillation frequency has been calculated by Werthamer (Werthamer, 1966). From this we may calculate the power absorbed in the MIM diode to be:

$$P_{abs} = \frac{1}{2} V_{ph} \sum_{n=-\infty}^{\infty} J_n\left(\frac{qV_{ph}}{\hbar\omega}\right)\left[J_{n+1}\left(\frac{qV_{ph}}{\hbar\omega}\right) + J_{n-1}\left(\frac{qV_{ph}}{\hbar\omega}\right)\right] I_{DC}\left(V_{bias} + n\frac{\hbar\omega}{q}\right) \quad (5.5.3)$$

We then set the power absorbed in the MIM diode equal to the power delivered by the sun over a 10 nm bandwidth calculated from the 5780 K blackbody approximation to the solar spectrum Figure (5-1). The photon voltage may then be calculated numerically from equation (5.5.3), as shown in Figure (5-20). The photon voltage (and consequently α) is lower than obtained when we quantized the field energy.

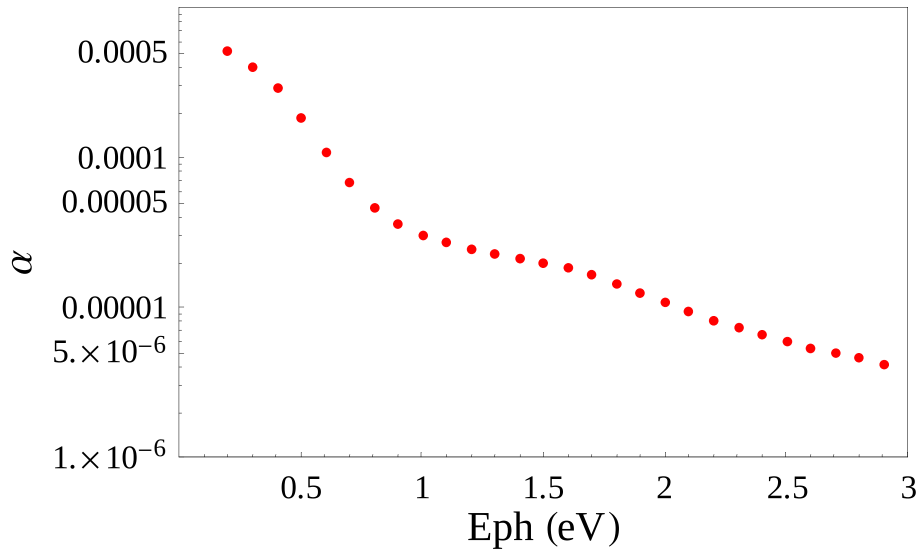

Fig. 5-20. *– The ratio α of photon voltage divided by the photon energy in eV, as a function of photon energy for the solar spectrum. It is assumed that 100 % of the incident power is absorbed in the MIM diode. A bandwidth of 10 nm is used.*

Decreasing α substantially decreases the conversion efficiency.

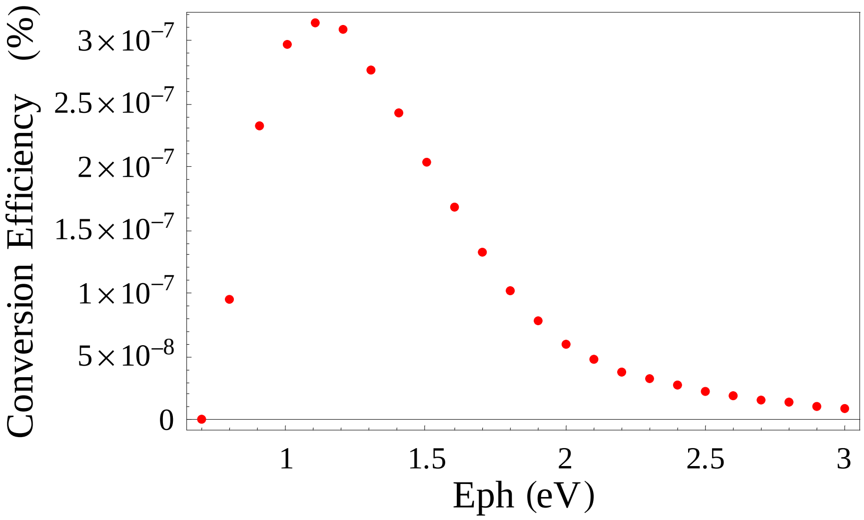

***Fig. 5-21. –** The conversion efficiency as a function of photon energy across the solar spectrum calculated by setting the power absorbed in the MIM diode equal to the incident solar power. A bandwidth of 10 nm is assumed.*

Figure (5-21) assumes that the solar energy is delivered over a one second time period. If the photon is harvested in a shorter time the input power and subsequently V_{ph} increases. The conversion efficiency as a function of alpha is shown in Figure (5-22), and as predicted, higher efficiencies are possible with higher values of α.

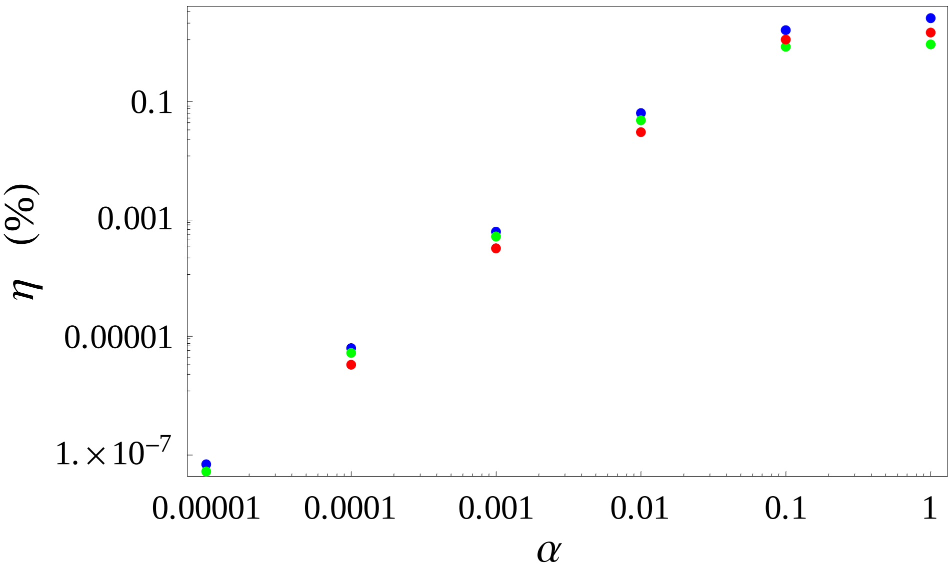

Fig. 5-22. *– The conversion efficiency as a function of α for photon energies of 1 (red), 2 (green) and 3 (blue) eV. The number of photon events was limited to two for the 1 and 2 eV photons and to one for the 3 eV photons.*

The maximum conversion efficiency possible with this improved MIM diode, as calculated from the semiclassical quantum analysis, is approximately 1.4 % even for high intensity illumination and multi-photon events.

Finally, I present the conversion efficiency for an MIM diode with a left barrier of 0.01 eV. In Figure (5-23) I vary both the oxide thickness and the right barrier height and calculate the conversion efficiency for 1 eV photons where α is fixed at one. I have used the WKB approximation to calculate the electron tunneling probability. This is not a realistic situation for solar energy harvesting and neglects the RC time constant limitations but it will tell us the maximum efficiency that could be expected for MIM diodes.

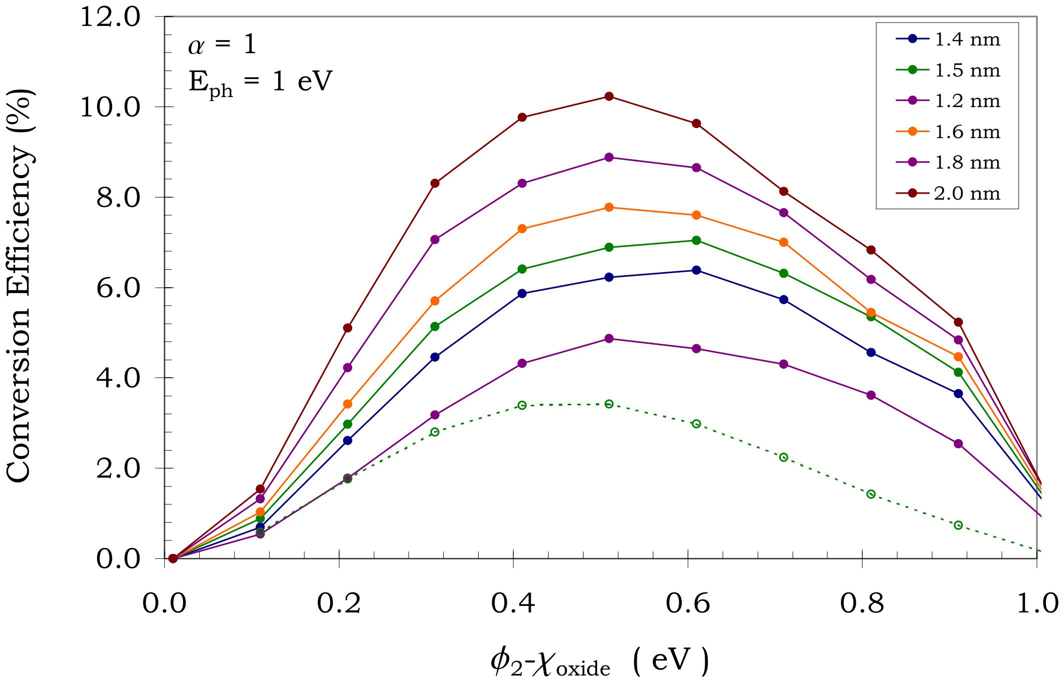

***Fig. 5-23.** – The conversion efficiency as a function oxide thickness and barrier height for 1 eV photons with α equal to 1. Each curve is for a different barrier height. The dashed curve is for a 1.5 nm thick oxide with a 0.1 eV left barrier height.*

The conversion efficiency is equal to zero when the right and left barrier heights are equal and the MIM diode is symmetric. As the difference between the right barrier and left barrier increases so does the conversion efficiency as a result of the increased asymmetry. The asymmetry and conversion efficiency increase further with thicker oxides.

The efficiency peaks and subsequently decreases for right barriers larger than 0.5 eV. This is a consequence of rectification reversal. As the right barrier height increases the location of the reversal occurs at larger voltages (approaching the photon energy in eV). This results in a decrease in the open circuit voltage and consequently a lower conversion efficiency.

The maximum efficiency we can reach with MIM diodes illuminated with 1 eV photons (α=1) is a function of the antenna impedance. A high impedance antenna is desirable since it allows matching to a more efficient thicker oxide MIM diode. We wish to make the left barrier as small as possible. However, we do not want to choose the right barrier as large as possible due to rectification reversal. An optimal right barrier is approximately 0.5 eV. An example material system matching this criterion is Nb and its native oxide with a Cu counter-electrode.

Given the low conversion efficiencies found it is worthwhile to determine what shape of J(V) curve is able to give us high conversion efficiency. Using the solar intensities 100 % efficiency can be attained only if the J(V) curve for the MIM diode has the form of a unit step function with zero current in reverse bias and a sufficiently high current in forward bias.

For a more realistic situation, consider that the MIM diode has a two-resistance J(V) form, with a forward bias resistance of R_F and a reverse bias resistance of R_R. If we require that

$$R_R > \frac{1}{J_1\left(\frac{qV_{ph}}{\hbar\omega}\right)^2} R_F \tag{5.5.4}$$

such that the quantum efficiency is equal to 100 % over the voltage range from 0 to $-q \cdot E_{ph}$ we obtain a maximum conversion efficiency of 25 % with single photon events. This is true regardless of how small we can make R_F (though a large value of R_F will decrease the conversion efficiency).

For this linear diode the efficiency does not increase above 25 % even in the presence of larger field intensities. Only if the current vs voltage curve of the diode saturates, exhibiting a resistance higher than R_F beyond the saturation voltage, can the diode exhibit photon stepping and efficiencies greater than 25 % (approaching 100 %).

In addition to the asymmetry requirements needed to obtain a unity quantum efficiency over a voltage span equal to the photon energy (in eV) the ideal diode must turn on as close to zero as possible. Additionally, it must saturate as quickly as possible. If the turn on and saturation occurs in a voltage span small compared to the photon energy and the incident power is fully absorbed within the MIM diode, high conversion efficiency may be obtained even with low field intensities. These requirements are not simultaneously met with MIM diodes.

In conclusion, I have presented the theoretical calculation of semiclassical rectification and applied it to solar energy conversion with MIM diodes. Broad band high conversion efficiencies are theoretically possible using a device possessing an appropriate J(V) curve having high quantum efficiency, large saturating current magnitudes, a low turn-on voltage, proper impedance matching, and a low capacitance. Rectification reversal decreases efficiency in the semiclassical case and further dictates the maximum barrier height that may be used for optimal conversion efficiency. A thick oxide is desirable to increase asymmetry. The maximum oxide thickness that may be realistically used is dependent upon the antenna resistance. The conversion efficiencies as a function of field strength for MIM diodes are lower than that for conventional silicon solar cells even with large field intensities. From estimates of the expected field strength from the sun it appears that the primary limitation to solar energy conversion by rectification will be the low field strength.

VI. ILLUMINATED MIM DIODE – HOT-ELECTRON THEORY

i. Introduction

In the preceding chapters the incident electromagnetic radiation was coupled across the oxide of the MIM diode by an antenna. Applying an electric field across the oxide of an MIM diode is equivalent to applying a bias voltage to the metal electrodes of the MIM diode. All of the electrons in one electrode are shifted in energy relative to the opposing electrode. The shift in electron energy occurs for all electrons within the electrode an equal amount.

A change in the electric field across the oxide results in a change in the slope of the conduction band edge in the band diagram. The electron tunneling probability as a function of energy then changes. Consequently, the asymmetry of the MIM diode I(V) curve when un-illuminated plays a role when the MIM diode is illuminated.

MIM diodes can exhibit an optical response even when no antenna is used. The optical response in this case is analogous to the photoelectric effect in metals (Fowler, 1931). A photon is incident upon the top metal surface of an MIM diode and couples to a single electron within the metal. The electron is excited up in energy by an amount equal to the photon energy. At this higher energy the electron tunneling probability through the barrier increases. The electron tunneling probability is equal for tunneling in either direction through a barrier so there will be no asymmetry for tunneling electrons excited in one electrode vs the other.

The excitation of a single electron up in energy does not directly produce an electric field across the oxide. Therefore, the band and tunneling probability as a function of energy does not change with illumination. Consequently, the illuminated characteristics produced by hot-electrons will be necessarily different from a MIM diode coupled to the illumination by an antenna.

ii. Theory

The theory of hot-electron excitation in Al-Al_2O_3-Au MIM diodes has been developed by Burshtein and Levinson (Burshtein, 1975). The theory was elaborated upon and verified experimentally by Marshalek (Marshalek, 1983). Marshalek included electron scattering within the electrodes that includes the electrons losing half of their excited energy with every collision.

For a sufficiently thin electrode and narrow bandgap oxide it is possible to excite carriers within the oxide rather than in the metal. This process has a 10% quantum efficiency and has a slow response time (Gustafson, 1983). This is because the excited electrons are subsequently transported in the conduction band of the oxide, and is a slower process than tunneling.

The electrons in the metal within the energy range between the Fermi level and a photon energy below the Fermi level are excited in energy (for simplicity I assume zero degrees Kelvin). The electrons within this energy range are excited with equal probability (Berglund, 1964). The excitation of electrons in a metal may subsequently be represented by modifying the Fermi distribution function within the illuminated metal electrode as shown in Figure (6-1).

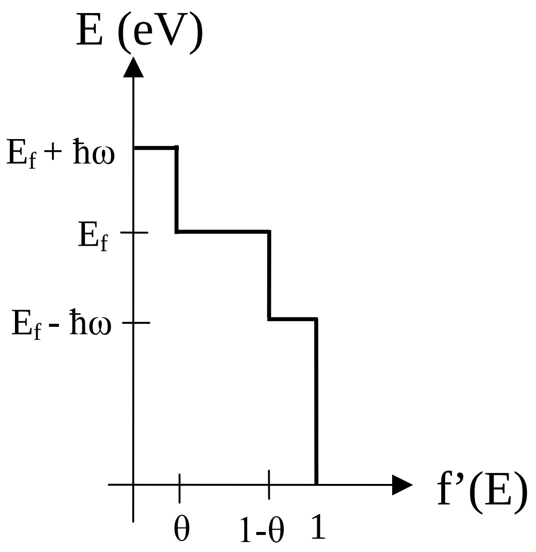

Fig. 6-1. *The modified Fermi distribution function plotted as a function energy for an illuminated metal electrode with hot-electron excitation. The number of excited electrons is a function of the θ factor. The temperature is zero degrees Kelvin.*

The number of electrons excited within the metal is a function of θ. This representation is applicable when the rate of photon arrival is sufficiently high to maintain the excited electron distribution depicted in Figure (6-1). Consequently, for solar intensities this model would only be valid for large area devices.

For solar energy conversion we will want to illuminate the MIM diode on a single side for maximum photocurrent. Assuming metal 1 is illuminated we may express the current density vs voltage for the MIM diode as

$$J_{Hot-Electron}(V) = \frac{4\pi mq}{h^3} \int_0^{\infty} T(E_x) \left[\int_{E_x}^{\infty} f_2(E-V) - f_1'(E)\, dE \right] dE_x \qquad (6.2.1)$$

Equation (6.2.1) is the dark current vs voltage expression from Section III with the modified Fermi distribution function used for metal 1.

This model does not include the multiple photon events that were included in the quantum rectification models. Furthermore, it does not include the possibility of exciting electrons which are located more than a photon's energy below the Fermi level into the vacated states of previously excited electrons. These stipulations should be reasonable for low intensity illumination.

The modified Fermi function of the illuminated metal does not conserve the number of electrons during the excitation process for density of states that varies with energy. Consequently, the density of electrons excited above the Fermi level due to incident photons takes the form

$$n(E) = g(E)\,f(E) + g(E-\hbar\omega)(1-\theta)\,f(E-\hbar\omega) \tag{6.2.2}$$

in the energy range of the Fermi level to a single photon energy above the Fermi level. Conservation of photon to electrons may be obtained by making θ a function of energy in the range of the Fermi level to a single photon energy above the Fermi level.

$$\theta'(E) = \theta\,\frac{g(E-\hbar\omega)}{g(E)} \tag{6.2.3}$$

Equation (6.2.3) is valid for an arbitrary density of states g(E).

The distribution of electrons as a function of energy is nearly equivalent for excitation by hot-electrons and the absorption spectrum in the semiclassical quantum model. The expression for the tunneling probability as a function of energy for the two models is inequivalent due to the shift in the band diagram that occurs with an antenna coupled MIM diode that does not occur for hot-electron excitations in the electrode of an MIM diode. Consequently, the illuminated current density vs voltage curves are not equivalent. This is not surprising since the semiclassical quantum model neglects interactions within the electrodes.

iii. Hot-Electron Solar Cells

For a solar cell operating by hot-electron excitations there will be an equivalent of a bandgap. Only electrons excited above or near the barrier height of the MIM diode are likely to tunnel across. Thus photons with an energy lower than the larger of the two barriers in the MIM diode are not collected efficiently.

Since all electrons within a photon energy below the Fermi level are excited with equal probability only a fraction will have sufficient energy to tunnel through the barrier. For low energy photons almost all of the excited electrons will be unable tunnel through the barrier. Even if an electron is excited there is a chance it relaxes and re-emits the incident photon, or that the energy is lost to heat. Furthermore, the tunneling probability decreases substantially below unity if the electron momentum is not perpendicular to the barrier.

The energy of the photon will not be harvested with 100 % efficiency if the electron thermalizes after tunneling through the oxide. Thermalization of the tunneling electron is likely given that the hot electron distance is approximately 10 nm (Eckertova, 1976). Therefore, electrons excited far above the conduction band of the insulator may have a large probability of tunneling across, but will subsequently thermalize within the second metal before reaching the load and energy will be lost.

In order to use the photon energy fully, for the fraction of electrons which are excited and tunnel through the barrier, we must make the MIM diode small enough that a single tunneling electron is sufficient to change the Fermi level within the receiving electrode. Equating the energy stored in the MIM diode treated as a capacitor to the incident photon energy we have:

$$\hbar\omega = \frac{1}{2} C_{MIM} V_{MIM}{}^{2} \tag{6.2.4}$$

The tunneling of n electrons across a barrier produces a voltage of

$$V_{MIM} = \frac{n \cdot q}{C_{MIM}} \tag{6.2.5}$$

Consequently, by solving for the capacitance C_{MIM} in equation (6.2.5) and substituting into equation (6.2.4) we find that the voltage produced by the MIM diode must be equal to

$$V_{ph} = \frac{2E_{ph}}{q} \tag{6.2.6}$$

This may be accomplished for photons of a single energy by making the capacitance of the MIM diode equal to

$$C_{MIM} = \frac{n \cdot q}{2 \cdot E_{ph}} \tag{6.2.7}$$

Let's assume we have a MIM diode with a 10 nm thick oxide, a dielectric constant of 10, and can harvest 1 eV photons with approximately 100 % quantum efficiency. If we assume that a single photon is incident upon the device and we want this photon to result in the tunneling of an electron which produces a voltage change equal to the photon energy we require that $C_{MIM} = 8 \times 10^{-20}$ F. To obtain this capacitance we must make the diode area 3 nm × 3 nm.

Once we have made the MIM diode this small two additional features play a role. First, we may be limited to the tunneling of a single electron by the coulomb blockade (Koch, 1992). Coulomb blockade is when the tunneling of a single electron produces a potential sufficiently high to prevent the tunneling of further electrons. Given the photon arrival rate from the sun this should not pose a significant problem.

Second, the potential produced by this electron will be lost if the MIM diode does not prevent the electron from tunneling back to the emitting electrode. We must illuminate the MIM diode on the side that minimizes the bounce-back of the tunneling electrode. This depends on the size of the voltage produced and the location of the rectification reversal point. For low voltages we will illuminate on the low-barrier side of the MIM diode, for high voltages we want to illuminate on the high-barrier side of the MIM diode. Since we initially assumed that the photon energy is larger than both of the barriers (or nearly as large), the generated voltage will be nearly as large as the two barriers. A thick barrier will not substantially reduce the tunneling probability of highly excited electrons but will substantially reduce the probability the electron returns to the emitting electrode. Consequently, the photon energy can be dissipated within the load.

We can deduce that a hot-electron MIM solar cell will be less efficient than conventional semiconductor based solar cells. The quantum efficiency for semiconductor solar cells is near unity, which will not be the case in the hot-electron solar cell.

Consider a MIM diode with a 10 nm thick oxide, and a symmetric barrier 0.6 eV in height illuminated by 1 eV photons. The top metal is sufficiently thin such that photoexcited electrons arrive at the metal-oxide interface without suffering a collision. For a 1 eV photon impinging a 0.6 eV barrier the probability of tunneling across is near 100 %. If we assume that the area of the device is approximately 3 nm × 3 nm the voltage generated due to the tunneling electron will be equal to two times the photon energy. The probability the electron tunnels back to the emitting electrode can be calculated to be negligible. Consequently, the energy collection efficiency can be approximately 100 %.

The 100 % efficiency assumes that all incident photons excite a carrier from the Fermi level and the excited carrier moves perpendicular towards the barrier (and does not reflect the incident photon or thermalize prior to tunneling). The tunneling probability decreases for carriers that are not incident perpendicular to the barrier. For a typical situation, we find that the tunneling probability decreases by an order of magnitude for carriers that are approximately 18° off of normal incidence of a 1 nm thick barrier (Waters, 1999). This implies that only 2 % of the carriers will be within the acceptance angle. Consequently, the efficiency drops to less than 2 %.

We must further consider that excitation of carriers deep below the Fermi level occurs with equal probability as exciting carriers near the Fermi level. Assuming only carriers that are within 0.4 eV of the Fermi level are excited with sufficient energy to traverse the barrier then only 40 % of the incident 1 eV photons produce a carrier, further reducing the efficiency to less than 0.8 %. The 40 % may be remedied by employing a quantum well in the emitting electrode to ensure all carriers are excited between a specific set of energy levels.

This efficiency is for a single photon energy. Photon energies much lower than the barrier height will not be collected and those greater than 1 eV will not have the photon energy fully collected. Even for the optimal photon energy we predict less than 0.8 % efficiencies. Although, under certain situations, this hot-electron solar cell may be more efficient than a solar cell comprised of an antenna coupled MIM diode (e.g., when the rectifying MIM diode is not sufficiently nonlinear for the incident photon), the efficiency is substantially lower than conventional silicon solar cells.

VII – RESONANT TUNNELING MIIM DIODES

i. Motivation

MIM diodes show less asymmetry and nonlinearity than desired. The low asymmetry and nonlinearity are partially responsible for the low solar energy conversion efficiency. We would like a diode with increased asymmetry for linear rectification and increased nonlinearity for square-law rectification. Furthermore, to obtain high conversion efficiency we require sufficiently high current magnitudes and low turn-on voltages.

One approach to improve the MIM diode asymmetry is by using two different electrodes, each with a different density of states. By making one of the electrodes a standard metal and the second electrode of a semiconductor, semi-metal, superconductor, superlattice or a quantum well, we can introduce additional asymmetry into the system. The disadvantage of this approach is the lower conductivity of other electrodes. It is preferable to use metals as the electrode material to maintain high conductivity.

An alternative approach to achieve asymmetry is to change the conduction mechanism in forward vs reverse bias. However, we want tunneling to provide the conduction mechanism in-order to maintain fast response times. In addition to the standard Fowler-Nordheim and direct tunneling observed in MIM diodes, a third possibility is resonant tunneling. Increased asymmetry may be achieved by making the electrons traverse the oxide by resonant tunneling under one polarity of bias and standard tunneling under the other polarity. This situation can be realized by using a multilayer structure between the electrodes instead of the single oxide layer. The multilayer structure may be composed of various combinations of insulators, metals, semiconductors, semimetals, superconductors, quantum wells, or superlattices.

Resonant tunneling is not a new phenomenon. Esaki tunnel diodes use resonant tunneling and the negative differential resistance associated with semiconductors (Mizuta, 1995). More recently Yukio has fabricated a triple barrier resonant tunneling diode using the GaInAlAs system and observed the gradual change from classical rectification to photon assisted tunneling (Oguma, 1999). Nobuo, using the same triple barrier structure as Oguma, with an improved antenna, observed the multi-photon process involved with photon assisted tunneling at 3.1 THz (96.8 μm) (Sashinaka, 2000). Di Ventra proposed a theoretical diode out of the InGaAs system that uses two adjacent oxides as opposed to the quantum wells formed with alternating metals and oxides (Di Ventra, 1996). To my knowledge the device proposed by Di Ventra was never realized in practice. A similar InGaAs structure that used a symmetric barrier was later proposed by Korotkov for use in non-volatile memory (Korotkov, 1999).

Resonant tunneling devices fabricated entirely out of metals and insulators are scarce. Watanabe has made double and triple barrier resonant tunneling devices with epitaxially grown single crystalline metals and insulators (Suemasu, 1994). The material system was $CoSi_2$ (metal) and CaF_2 (insulator). The choice of metals and insulators is restricted to those that lattice-match the substrate. With the advent of atomic layer deposition, it is possible to form multilayer structures composed of metals and insulators. We are no longer limited to the native oxides of the base metals but can instead deposit a variety of different oxides by using ALD. Depositing metals with ALD makes it possible to form amorphous equivalents of Suemasu’s multibarrier structures, in addition to superlattices. Furthermore, it becomes feasible to put multiple insulators adjacent to one another.

The device I proposed uses two adjacent oxides in place of the single oxide layer found in MIM diodes. Using atomic layer deposition, a second oxide may be deposited onto the native oxide of the base metal. This device may be easily fabricated using a wider range of materials than possible with epitaxial techniques previously used to fabricate resonant tunneling devices. The remainder of this section presents the metal-insulator-insulator-metal (MIIM) diode.

ii. MIIM Diode Theory

The MIIM diode utilizes two adjacent insulators, sandwiched between the metal electrodes, instead of one. These two insulators have different electron affinities and consequently result in a discontinuity at their interface. The equilibrium band diagram for one such MIIM structure is shown in Figure (7-1).

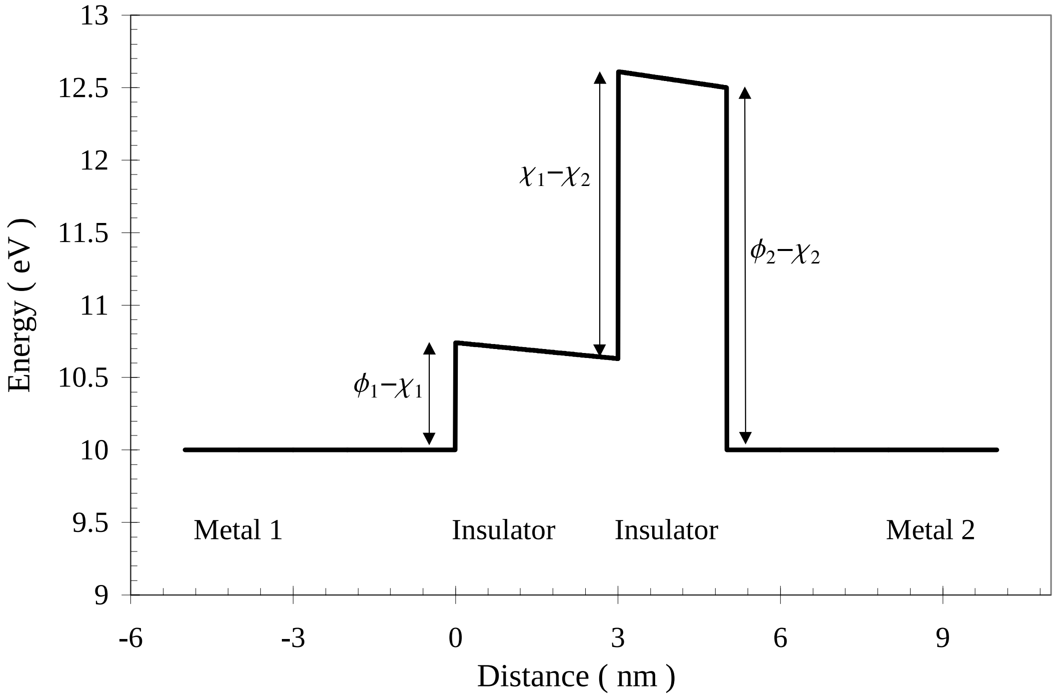

Fig. 7-2. *Energy band diagram for a $Cr/Cr_2O_3/Al_2O_3/Cr$ MIIM diode in equilibrium.*

The barrier heights are determined by the workfunctions ϕ_1 and ϕ_2 of the two metal electrodes and electron affinities χ_1 and χ_2 of the two adjacent insulators.

The energy band diagram under an applied bias is shown in Figure (7-2). With a negative bias voltage applied to metal 2 we encounter a combination of Fowler-Nordheim and direct tunneling. When a positive voltage is applied to metal 2 a quantum well forms at the interface of the two oxides.

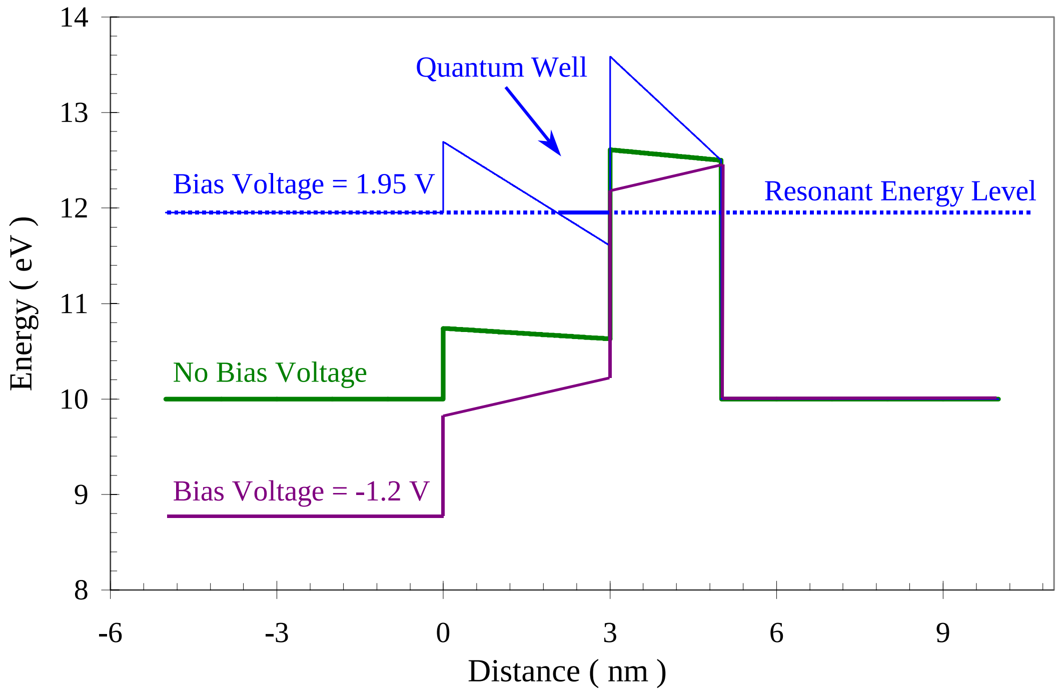

Fig. 7-2. *Energy band diagram for a Cr/Cr_2O_3/Al_2O_3/Cr MIIM diode shown in equilibrium and with both polarities of applied bias. Positive applied biases create a quantum well in the first oxide adjacent to the dual oxide interface.*

Within the quantum well the allowed energy levels are quantized (the lowest quantized energy level within the well is shown with the dashed line). As shown in Figure (7-3), the tunneling probability through these quantized energy levels is higher than the tunneling probability for adjacent energy levels.

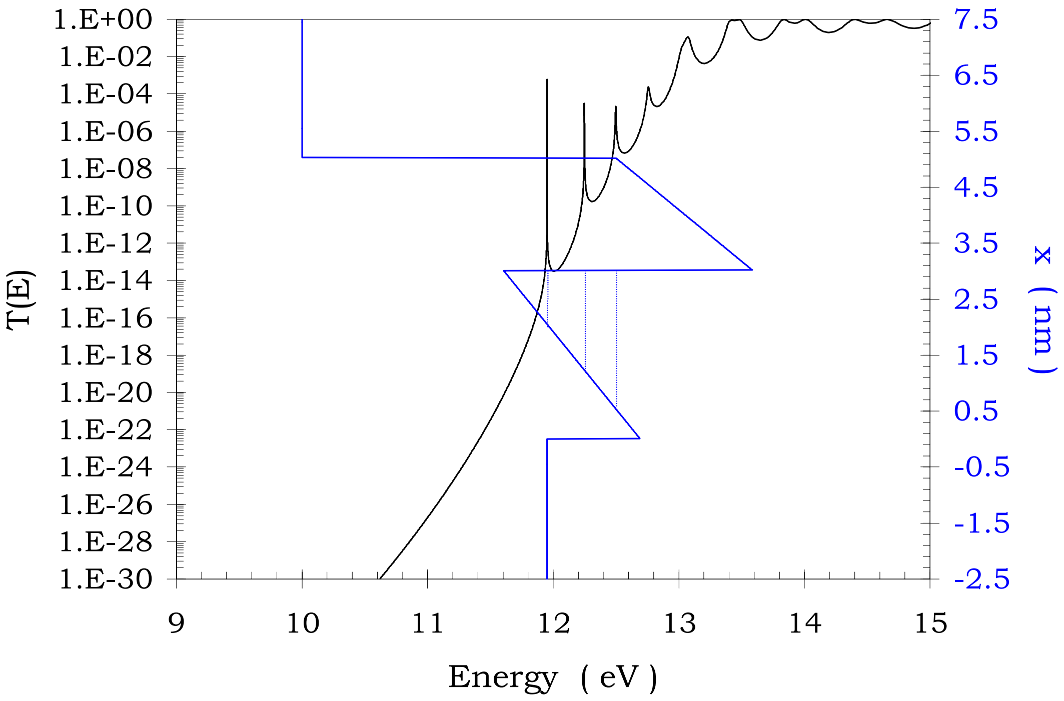

Fig. 7-3. *Electron tunneling probability as a function of energy superimposed upon the band diagram of the MIIM diode. The resonant energy levels formed within the quantum well (shown on the band diagram) produce an increased tunneling probability through the structure.*

As shown in Figure (7-4), the resonant tunneling energy levels introduce a substantial asymmetry into the current vs voltage curve for positive applied voltages compared to negative applied voltages.

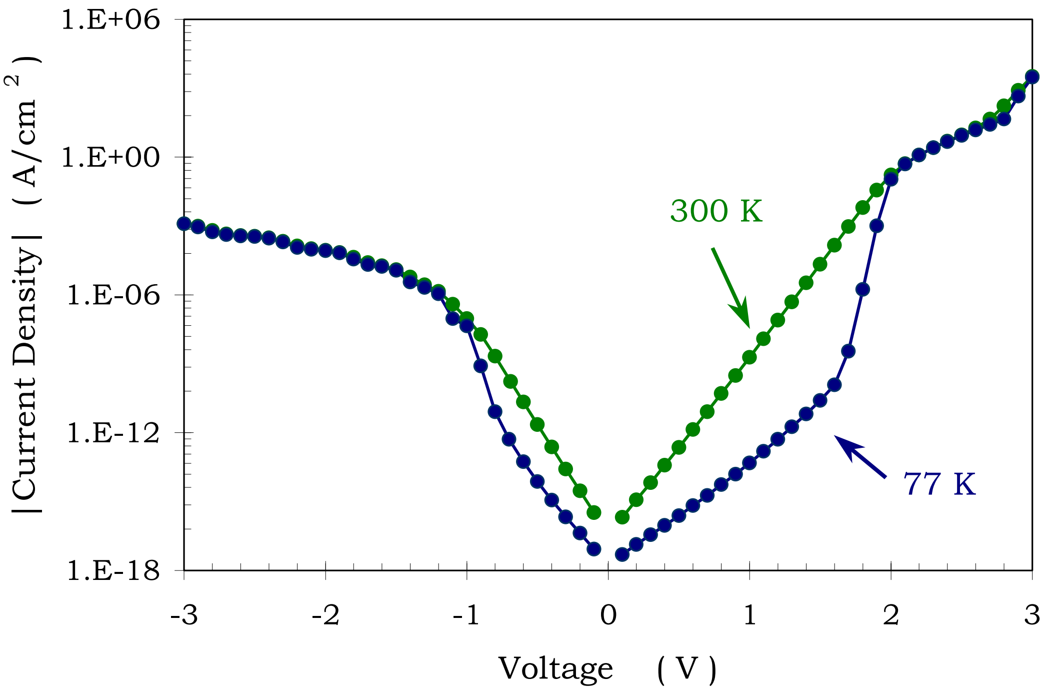

Fig. 7-4. *The calculated current density vs voltage curve for the MIIM diode shown in Figure (7-2). Calculations made at 300 K (green) and 77 K (blue).*

This asymmetry is made vividly clear on a linear current density scale as shown in Figure (7-5).

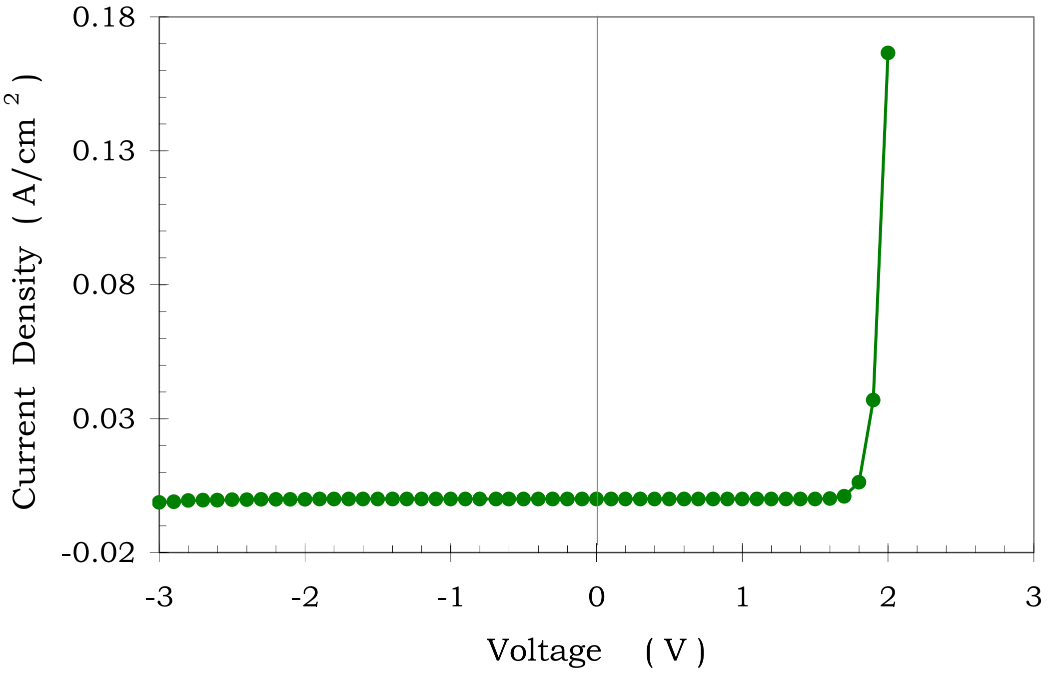

Fig. 7-5. *The calculated current density vs voltage curve for the MIIM diode shown in Figure (7-2) plotted on a linear current density scale.*

For electrodes with a band gap, or variable density of states, resonant tunneling in this dual insulator structure results in a region of substantial negative differential resistance. In the MIIM diode we do not see a negative differential resistance.

iii. Experimental MIIM Diode

I have fabricated several MIIM diodes using atomic layer deposition to form the second insulator. The devices were fabricated using the lithographic MIIM mask presented in Section II. The MIIM diode was fabricated on a silicon substrate with a thermally grown oxide layer. Contact pads were made using 100 nm of Cr covered by 100 nm of Au. The Au metal prevented complete Al_2O_3 coverage and allowed contact to be made to the device after the ALD deposition. The base metal was formed of Cr and allowed to oxidize to form Cr_2O_3. Subsequently 3 nm of Al_2O_3 was deposited by atomic layer deposition. Top contacts were formed of Ag.

The experimental current vs voltage curve for the MIIM diode is shown in Figure (7-6).

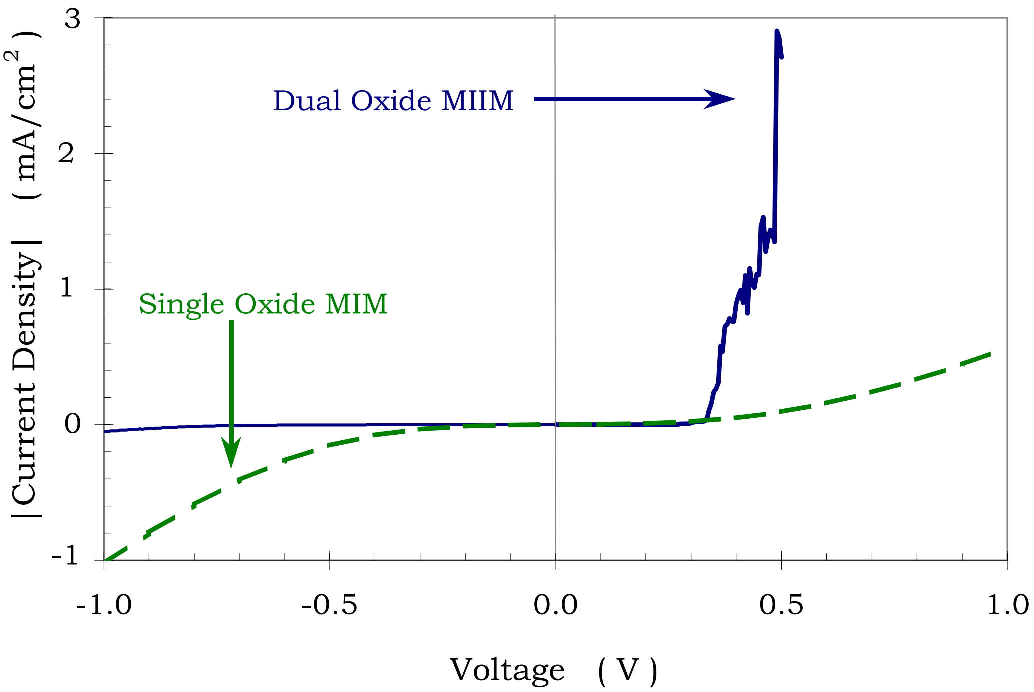

Fig. 7-6. *Experimental data for an MIIM diode and a typical MIM diode. The MIM curve has been multiplied by 10^{-6} to allow the two devices to be plotted on the same linear scale. This comparison is valid for thick oxide layers.*

The current vs voltage curve was stable under reverse bias and repeated itself. The forward bias portion of the curve showed drastic nonlinearity as expected. The forward bias portion of the curve did not repeat itself and the current magnitude fluctuated from one measurement to the next. However, the dramatic nonlinearity was present for each voltage sweep regardless of voltage sweep direction.

The experimental current vs voltage curve agrees with theory only qualitatively. The current magnitudes do not. I suspect the disagreement is due in part to surface states at the interface between the Cr_2O_3/Al_2O_3. The yield on these devices was very low (1/500). The low yield I suspect was due to the poor nucleation of the ALD layer to the native chromium oxide as most devices measured did not have low current magnitudes or a decreased capacitance as would be expected if the ALD layer was present. Recent experiments indicate that the nucleation may be improved by increasing the precursor concentrations.

iv. Solar Energy Conversion Efficiency

The current vs voltage curve in Figure (7-6) shows some of the characteristics required for high conversion efficiency. The asymmetry is larger than the MIM diode in forward vs reverse bias directions and the knee of the curve is located at lower voltages than the MIM diode. However, the solar energy conversion efficiency of the experimental MIIM diode would be uselessly low due to the low current densities.

I use an MIIM diode based upon the improved MIM diode from Section V to estimate the solar energy conversion efficiency of an MIIM diode. For the MIIM diode the left barrier is chosen as 0.01 eV, the right barrier is 0.41 eV, and the oxide interface barrier is 0.4 eV. These values are chosen directly from the improved MIM diode from Section V. The left oxide is 1 nm thick and the second oxide is set to 0.5 nm thick. The J(V) curve for both the improved MIM diode and the MIIM diode are shown in Figure (7-7). The thinner oxide layers and smaller barriers in this theoretical MIIM diode result in higher current magnitudes than the experimental MIIM diode. The MIIM diode shows a slightly larger current magnitude and asymmetry over the MIM diode.

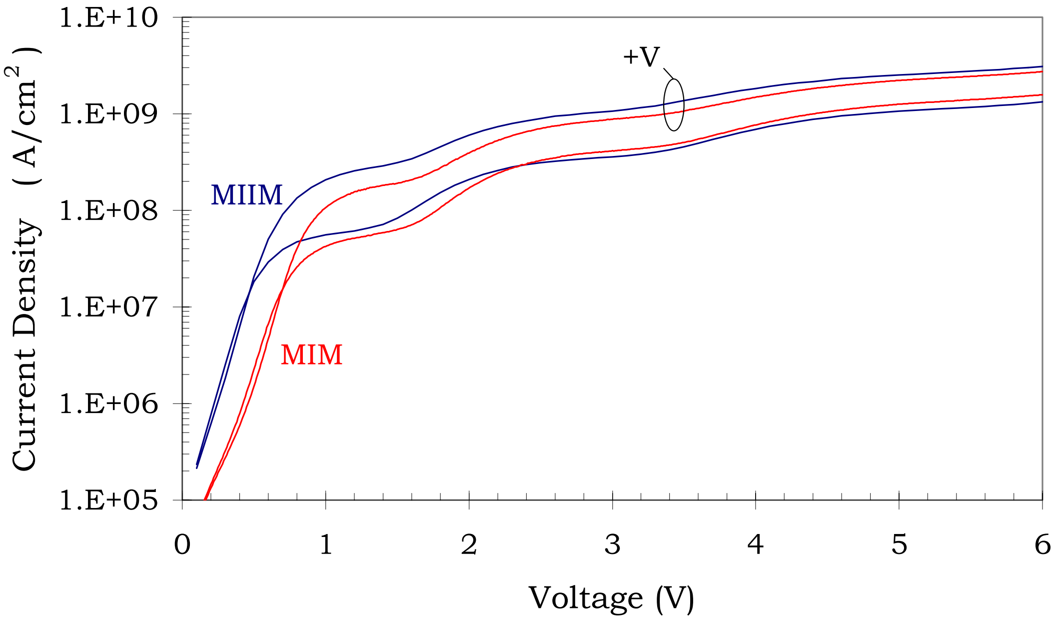

Fig. 7-7. *The current density vs voltage curve for the optimized MIM diode from Section V and an MIIM diode based upon the improved MIM diode.*

I calculated the solar energy conversion efficiency assuming the diode area is 50 nm x 50 nm. The semiclassical quantum mechanical J(V) theory is used to calculate the power out of the MIIM diode. I assumed that the antenna is 100 % efficient at transferring the incident photons electric field across the oxide of the diode and that the diode fully absorbs the incident power.

The photon voltage across the MIIM diode is calculated from the solar spectrum which is approximated by a 5780 K blackbody. The α, the photon voltage divided by the photon energy, is plotted in Figure (7-8).

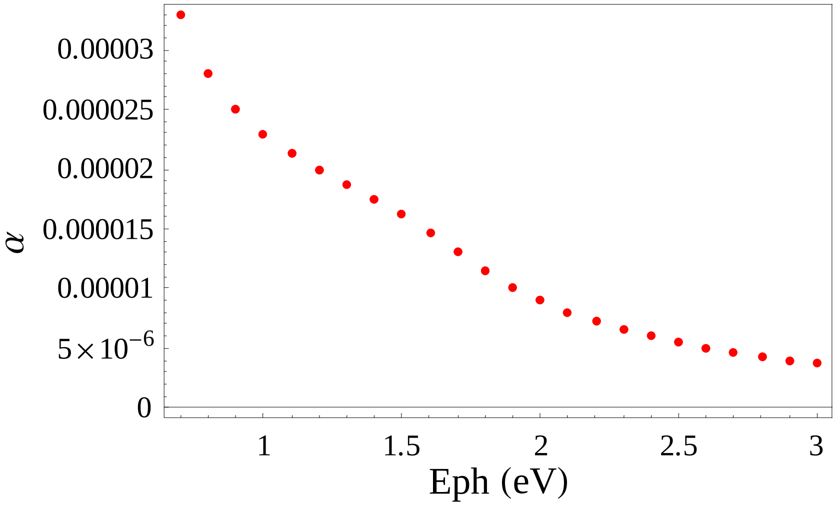

Fig. 7-8. *The α (the photon voltage times the photon energy) as a function of the photon energy on the MIIM structure across the solar spectrum.*

The values of α are approximately an order of magnitude lower than those obtained with the MIM diode due to the lower resistance of the MIIM diode.

The solar energy conversion efficiency vs photon energy across the solar spectrum is shown in Figure (7-9).

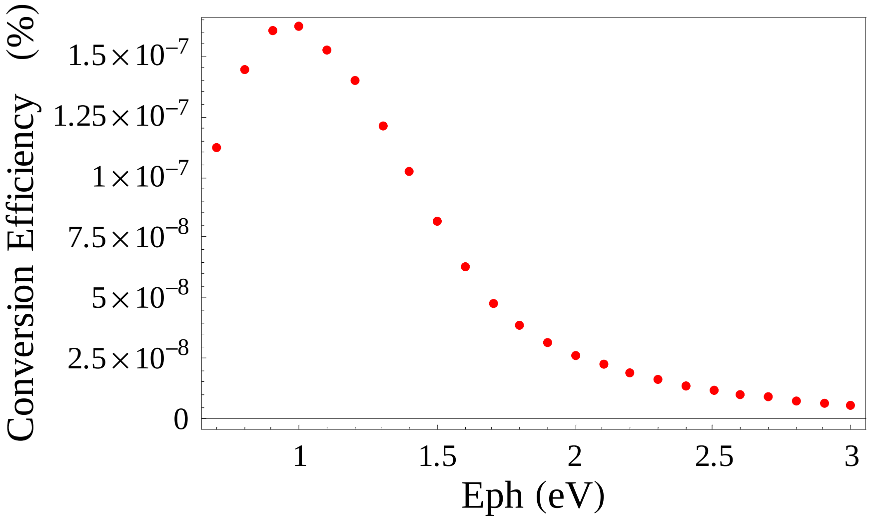

Fig. 7-9. *The conversion efficiency for the MIIM diode over a range of incident photon energies.*

The MIIM diode has a maximum conversion efficiency of approximately 1.6×10^{-7} %. The optimized MIM diode obtained an efficiency of 3.2×10^{-7} %. The decrease in efficiency is due to the lower photon voltage produced across the MIIM diode as opposed to the MIM diode.

A higher power incident on the MIM diode will result in an increase in α. The conversion efficiency as a function of α is shown in Figure (7-10).

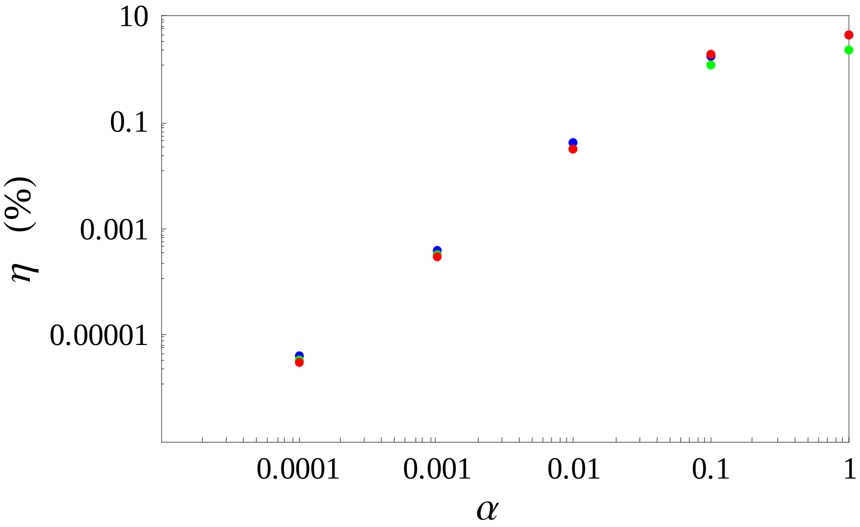

Fig. 7-10. *The conversion efficiency as a function of α for photon energies of 1 eV (red points), 2 eV (green points) and 3 eV (blue points). The number of photon events was limited to two for the 1 eV photons and one for the 2 and 3 eV photons.*

For high field intensities, the MIIM diode produces higher conversion efficiencies than the improved MIM diode from Section V due to the larger current density and greater asymmetry in the MIIM diode current vs voltage curve. The maximum conversion efficiency of this MIIM diode, calculated using the semiclassical quantum approach, is approximately 4 %. The roll-off and maximum efficiency limit is due to the MIIM diode.

Finally, I calculate the quantum efficiency of the MIIM diode at zero bias as a function of photon energy, shown in Figure (7-11).

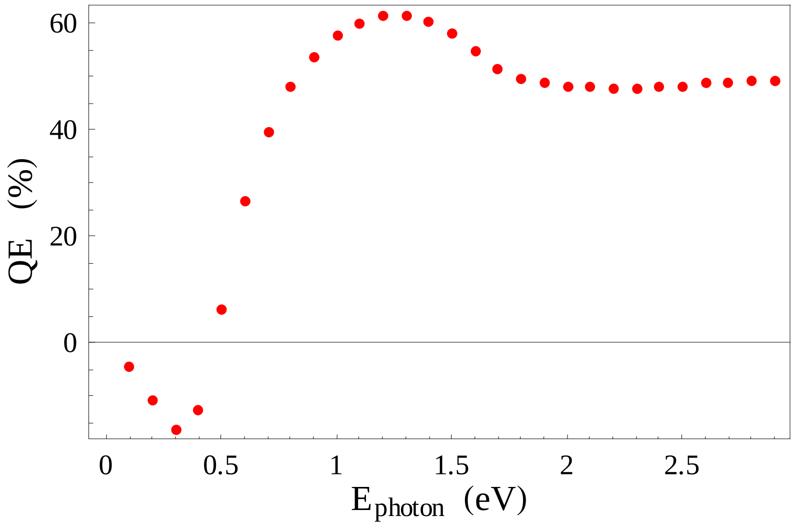

Fig. 7-11. *The quantum efficiency of the MIIM diode.*

The quantum efficiency of the MIIM diode reaches approximately 60 % for 1.2 eV photons. The improved MIM diode produced a maximum quantum efficiency just under 50 %. This improvement can be attributed to the greater asymmetry in the J(V) curve.

In conclusion, although the particular MIIM diode structure presented is an improvement over the single layer MIM diode structure, low efficiencies are still obtained due to the low field intensity.

VIII – CONCLUSIONS AND RAMIFICATIONS

I have explored the possibilities of using MIM diodes for solar energy harvesting assuming an ideal antenna. Actual efficiencies obtained will likely be lower than what I have predicted once a realistic antenna is incorporated.

I have fabricated MIM diodes from Ti, Ni, Cr, Al, and Nb base metals using several different fabrication techniques. The current vs voltage curves of the MIM diodes were measured and calculated from theory. The forward vs reverse bias asymmetry, area scaling, and relative current magnitude shifts could be predicted. The current magnitude and curvature did not match the experimental data when literature values for material parameters were used. To obtain a better fit with theory, without arbitrarily adjusting material parameters, multiple experiments would be necessary to isolate barrier heights and oxide thicknesses (thermal, optical, and destructive).

The processing of the oxide layer played a critical role in MIM diode performance. The oxidation method, conditions, substrate, cleanliness, oxidation time, temperature, ion incorporation, plasma processing, measurement techniques, and metals all affect the MIM diode performance. The processing steps required to fabricate a functional MIM diode are very unforgiving.

The various models applicable to illuminated MIM diodes have been explored for solar energy conversion. Due to the broad frequency range that the MIM diode is subjected to by the sun both classical and quantum models are explored. In the classical regime the current models are limited by the approximations used.

Consequently, I developed a PSpice model applicable to MIM diodes. The PSpice model has the unique ability to incorporate the rectification reversal effect found to occur in MIM diodes. Furthermore, the PSpice model is not limited to MIM diodes but is equally applicable to many other electron devices.

As the frequency increases the size of the incident electromagnetic quanta becomes large on a voltage scale equal to the photon energy (divided by q) these classical models are no longer valid. The quantitative frequency ranges for the various illuminated models presented in Figure (1-3) depend upon the explicit shape of the diodes J(V) curve. For most MIM diodes the nonlinearity over a voltage span equal to the photon energy (times q) of visible light warrant use of the semiclassical models. For example, in Figure (8-1) I plot the responsivity at zero volts for the improved MIM diode as a function of photon energy.

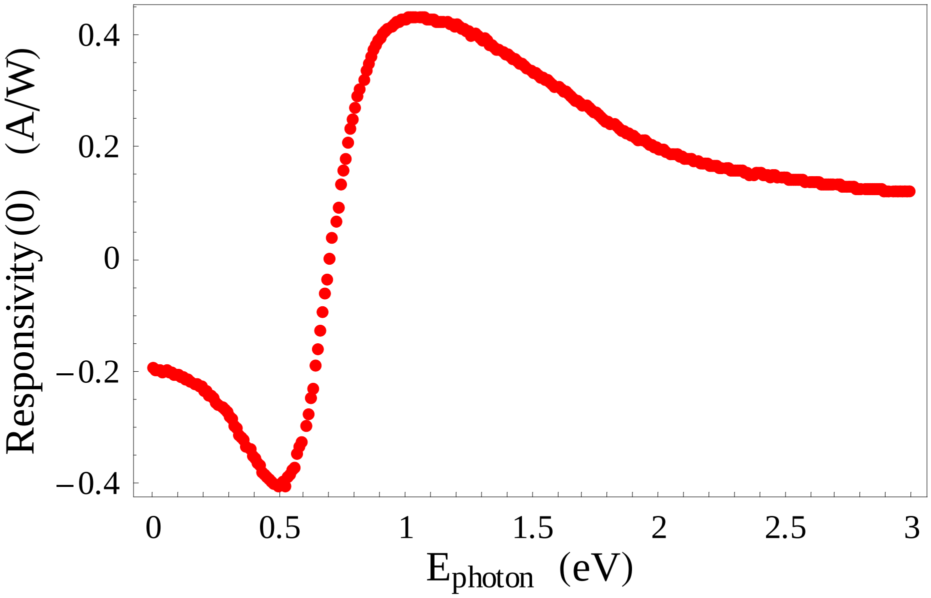

Fig. 8-1. *The responsivity (without taking the absolute value) as a function of photon energy. For the improved MIM diode the classical result is in correct within 10 % for energies less than 0.14 eV (corresponding to a 8.86 μm wavelength). For shorter wavelengths the semiclassical theory must be used.*

The classical theory is correct within 10 % for incident wavelengths longer than 8.86 μm).

Efficiencies greater than 25 % become possible with these quantum models with the aid of photon stepping. I have shown that with a perfect photon step 100 % conversion efficiencies can be obtained. However, the intensity of the solar spectrum and nonlinearity attainable with MIM diodes limit the efficiencies to much lower values.

I calculated the conversion efficiencies as a function of photon energy, field intensity, and the diode structure. Estimates of the field intensity coupled to the insulator of the MIM diode by the sun were made. The limitations of the semiclassical model became evident due to the low photon numbers involved. Despite these limitations, I was able to use the semiclassical theory to predict what is needed in an MIM diode structure to obtain high efficiencies: small capacitance, high current magnitudes, large asymmetries (responsivity) and low turn on voltages. Conversion efficiencies less then 1 % were calculated.

I considered making a hot-electron solar cell where no electric field is imposed across the oxide due to the incident photon. This situation occurs when an antenna is not used. In the semiclassical theories, there is a link between the energy of the incident photon and the voltage induced across the structure and as a result efficient conversion over a range of photon energies is possible. To make an efficient hot-electron solar cell this link must be built into the device. I have shown that for a hot-electron solar cell to be efficient, for a single photon energy, the diode must be made sufficiently small such that the tunneling of a single electron can substantially alter the voltage across the oxide. The voltage change due to the tunneling of a single electron is an effect that should be included in future work on the semiclassical theories as well. The final efficiency is estimated to be less than 1 % for the hot-electron solar cell for a single energy. Although this efficiency may be higher than the MIM diode functioning as a rectifier in conjunction with an antenna, the hot-electron solar cell will be less efficient then conventional semiconductor solar cells. Furthermore, unlike the rectifying MIM diode using photon stepping, the hot-electron solar cell will only collect photons of a single energy efficiently.

Finally, I developed an improved metal-insulator based device based upon an extension of the MIM diode. The MIIM diode produces an enhanced nonlinearity by incorporating two adjacent oxides instead of the single oxide layer of the MIM diode. In the MIIM diode the mode of tunneling under positive applied biases can be made different from that under negative applied biases resulting in improved asymmetry. The improved asymmetry was predicted by an extension of the MIM diode calculations. MIIM diodes were fabricated using atomic layer deposition to deposit the second oxide layer and produced a substantial increase in nonlinearity over the single layer MIM diodes. The MIIM diode incorporates some of the improvements required for efficient energy harvesting.

In closing, obtaining high efficiency over a wide range of photon energies may be accomplished by rectification and the resulting photon steps. The solar energy conversion efficiencies are substantially lower than conventional semiconductor based solar cells. The primary limitation is due to the low field strengths imposed across the MIM diode by the solar intensity. Even if the field intensities are substantially increased, the conversion efficiencies for MIM diodes with acceptable impedances are less than conventional semiconductor solar cells. This is because of rectification reversal and because the MIM diode does not simultaneously attain high quantum efficiencies, low turn-on voltages, high current magnitudes and small capacitance.

BIBLIOGRAPHY

Agilent Technologies, 395 Page Mill Road, P.O. Box 10395, Palo Alto, CA 94306, (650) 752-5000, (2001).

Alessandrini, E.I., Brusic, V., “Effect of Varying Oxidizing and Nitriding Parameters on the Surface of Cr Thin Films”, *Journal of Vacuum Science and Technology*, **9**, 83, (1972).

Anderson, L.M., “Harnessing Surface Plasmons for Solar Energy Conversion”, *SPIE – Integrated Optics III*, **408**, 172, (1983).

Ashcroft, N.W., Mermin, N., *Solid State Physics*, Saunders College, Philadelphia, (1976).

AutoDesk Incorporated, 111 McInnis Parkway, San Rafael, CA 94903, (415) 507-5000, (2001).

Aversa, C., Keay, B.J., “Virtual States and Photon-Assisted Tunneling”, *Physical Review B*, **54**, R2284, (1996).

Baird, K.M., “Frequency Measurement of Optical Radiation”, *Physics Today*, January, 51, (1983).

Bardeen, J., “Surface States and Rectification at a Metal Semi-Conductor Contact”, *Physical Review*, **71**, 717, (1947).

Berglund, C.N., Spicer, W.E., “Photoemission Studies of Copper and Silver : Experiment”, *Physical Review*, **136**, A 1044, (1964)

Borland Software, Inc., 100 Enterprise Way, Scotts Valley, CA 95066-3249, (831) 431-1000, (2001).

Bube, R.H., *Fundamentals of Solar Cells*, Academic Press, New York, (1983).

Burshtein, Z., Levinson, J., “Photo-Induced Tunnel Currents in Al-Al_2O_3-Au Structures”, *Physical Review B*, **12**, 3453, (1975).

Burstein, C., Lundqvist, S., *Tunneling Phenomena in Solids*, Plenum Press, New York, (1969).

Cahalan, R.F., http://climate.gsfc.nasa.gov/~cahalan/Radiation/, NASA-Goddard, 913 Greenbelt, MD 20771 (1999).

Campbell, S.A., *The Science and Engineering of Microelectronic Fabrication*, Oxford University Press, New York, (1996).

Cerac, Inc., 407 N. 13th Street, Milwaukee, WI 53233-2201, (414) 289-9800 (2001).
Climent, F., Capellades, R., "Anodic Oxidation of Titanium at Low Voltages", *Materials Letters*, **18**, 263, (1993).

Champlin, K.S., Eisenstein, G., "Cutoff Frequency of Submillimater Schottky-Barrier Diodes", *IEEE Transactions on Microwave Theory and Techniques*, **MTT-26**, 31, (1978).

Cohen, E.R., Taylor, B.N., "The Fundamental Physical Constants", *Physics Today*, **August**, BG7, (1997).

Dayem, A.H., Martin, R.J., Physical Review Letters, **8**, 246, (1962).

Deeley, P.M., *Electrolytic Capacitors; The Theory, Construction, Characteristics, and Application of All Types*, The Cornell-Dubilier Electric Corporation, New Jersey, (1938).

Diesing, D., Hassel, A.W., Lohrengel, M.M., "Aluminum Oxide Tunnel Junctions: Influence of Preparation Technique, Sample Geometry and Oxide Thickness", *Thin Solid Films*, **342**, 282, (1999).

Di Ventra, M., Papp, G., Coluzza, C., Baldereschi, A., Shulz, P.A., "Indented Barrier Resonant Tunneling Rectifiers", *Journal of Applied Physics*, **80**, 4174, (1996).

Duke, C.B., *Tunneling in Solids*, Academic Press, New York, (1969).

Dunne, P.J., Collins, R.A., "Measurement Techniques in MIM Device Characterization", *International Journal of Electronics*, **68**, 373, (1990).

Eckertova, L., Dvorak, J., Bocek, J., "The Range of Hot Electrons in Thin Metal Films Determined by the Electron Emission from MIM Structures", *Thin Solid Films*, **36**, 171, (1976).

Elchinger, G.M., Sanchez, A., Davis, C.F., Javan, A., "Mechanism of Detection of Radiation in a High-Speed Metal-Metal Oxide-Metal Junction in the Visible Region and at Longer Wavelengths", *Journal of Applied Physics*, **47**, 591, (1976).

Eliasson, B., Moddel, G., "Optically Addressed SLM Incorporating a $CuInGaSe_2$/a-Si:H Heterojunction, Spatial Light Modulators", Technical Digest1999, OSA Technical Digest Snowmass, 97, (1999).

Emery, K., "The Rating of Photovoltaic Performance", *IEEE Transactions on Electron Devices*, **46**, 1928, (1999).

Entegris, Inc., 3500 Lyman Boulevard, Chaska, MN 55318 1-800-394-4083 (2001).

Jennings, D.A., Evenson, K.M., Knight, D.J.E., "Optical Frequency Measurements", *Proceedings of the IEEE*, **74**, 168, (1986).

Fan, J., Sugioka, K., Toyoda, K., "Low-Temperature Growth of Thin Films of Al_2O_3 by Sequential Surface Chemical Reaction of Trimethylaluminum and H_2O_2", *Japanese Journal of Applied Physics*, **30**, L1139, (1991).

Faris, S.M., Gustafson, T.K., Wiesner, J.C., "Detection of Optical and Infrared Radiation with DC-Biased Electron-Tunneling Metal-Barrier-Metal Diodes", *IEEE Journal of Quantum Electronics*, **QE-9**, 737, (1973)

Foden, C.L., Whittaker, D.M., "Quantum Electrodynamic Treatment of Photon-Assisted Tunneling", *Physical Review B*, **15**, 12617, (1998).

Fonash, S.J., *Solar Cell Device Physics*, Academic Press, New York, (1981).

Fowler, R.H., "The Analysis of Photoelectric Sensitivity Curves For Clean Metals at Various Temperatures", **33**, (1931).

Fowler, R.H. , Nordheim, L., "Electron Emission in Intense Electric Fields", *Proceedings of the Royal society of London A.*, **173**, (1928).

Fu, C.Y., Van Duzer, T., "A New Lead Alloy For Josephson Junctions", *IEEE Transactions on Magnetics*, **MAG-17**, 290, (1981).

Fumeaux, Herrman, "Nanometer Thin Film Ni-NiO-Ni Diodes for Detection and Mixing of 30 THz Radiation", *Infrared Physics and Technology*, **39**, (1998)

George, S.M., Dillon, A.C., Ott, A.W., Way, J.D., "Surface Chemistry of Al_2O_3 Deposition Using $Al(CH_3)_3$ and H_2O in a Binary Reaction Sequence", *Surface Science*, **322**, 230, (1995).

Geppert, D.V., "Space-Charge-Limited Tunnel Emission into an Insulating Film", *Journal of Applied Physics*, **33**, 2993, (1962).

Gewinner, G., Peruchetti, J.C., Jaegle, A., Kalt, A., "Photoemission Study of the Chromium (111) Surface Interacting with Oxygen", *Surface Science*, **78**, 439, (1978).

Griffiths, D.J., *Introduction to Quantum Mechanics*, Prentice-Hall, New Jersey, (1995).

Grober, R.D., Schoelkopf, R.J., Prober, D.E., "Optical Antenna: Towards a Unity Efficiency Near-Field Optical Probe", *Applied Physics Letters*, **70**, 1354, (1997).

Gundlach, K.H., “Theory of Metal-Insulator-Metal Tunneling for a Simple Two-Band Model”, *Journal of Applied Physics*, **44**, 5005, (1973).
Gustafson, T.K., “Coherent Conversion of the Sunlight Spectrum Final Report”, NASA Grant NAG 3-88, University of California, Berkeley, (1982).

Hocker, L.O., Sokoloff, D.R., Daneu, V., Szoke, A., Javan, A., “Frequency Mixing in the Infrared and Far-Infrared Using a Metal-To-Metal Point Contact Diode”, *Applied Physics Letters*, **12**, 401, (1968).

Hübers, H.W., Schwaab, G.W., Röser, H.P., “Video Detection and Mixing Performance of GaAs Schottky-Barrier Diodes at 30 THz and Comparison with Metal-Insulator-Metal Diodes”, *Journal of Applied Physics*, **75**, 4243, (1994).

International Products Corporation, P.O. Box 70, Burlington, NJ 08016, (609) 386-8770, (2001).

Iscoff, R., “Wafer Cleaning: Wet Methods Still Lead the Pack”, *Semiconductor International*, **16**, 58, (1993).

Johnson, R.C., *Antenna Engineering Handbook*, 3rd edition, McGraw-Hill, New York, (1993).

J.T. Baker, 222 Red School Lane, Phillipsburg, NJ 08865, 1-800-JTBAKER, (2001).

Kale, M.B., “Electron Tunneling Devices in Optics”, *Optical Engineering*, **24**, 267, (1985).

Kalra, K.C., Singh, K.C., Singh, M., “Formation of Anodic Oxide Films on Titanium in the Presence of Ultraviolet Radiation”, *Indian Journal of Chemistry*, **33A**, 732, (1994).

Kittel, C., *Introduction to Solid State Physics*, 6th edition, John Wiley and Sons, New York, (1986).

Koch, H., Lübbig, H., *Single-electron Tunneling and Mesoscopic Devices*, Springer-Verlog, New York, (1992).

Korotkov, A., Likharev, K., “Resonant Fowler-Nordheim Tunneling Through Layered Tunnel Barriers and its Possible Applications”, International Electron Device Meeting, Technical Digest, Washington DC, (1999).

Kroemer, H., *Quantum Mechanics For Engineering, Materials Science, and Applied Physics*, Prentice Hall, New Jersey, (1994).

Landauer, R., Martin, Th., “Barrier Interaction Time in Tunneling”, *Reviews of Modern Physics*, **66**, 217, (1994).

Levy, “Very Small Tunnel Junctions Sense the Effect of Single Electrons”, *Physics Today*, **41**, 19, (1988).

Lichtenberger, A.W., Lea, D.M., Lloyd, F.L., “Investigation of Etching Techniques for Superconductive Nb/Al-Al_2O_3/Nb Fabrication Processes”, IEEE Transactions on Applied Superconductivity, **3**, 2191, (1993).

Loudon, R., *The Quantum Theory of Light*, 3rd edition, Oxford University Press, Oxford, (2000).

Maissel, L.I., Glang, R., *Handbook of Thin Film Technology*, McGraw-Hill, New York, (1970).

Mathworks, Inc., 3 Apple Hill Drive, Natick, MA 01760-2098, (508) 647-7000, (2001).

Marshalek, R.G., Davidson, F.M., “Photoresponse Characteristics of Thin-Film Nickel-Nickel Oxide-Nickel Tunneling Junctions”, *IEEE Journal of Quantum Electronics*, **QE-19**, 743, (1983).

Martin, S. et al, “Fabrication of 200 to 2700 GHz Multiplier Devices Using GaAs and Metal Membranes”, *IEEE MTT-S Digest*, Phoenix, AZ, (2001).

Microsoft, One Microsoft Way, Redmond, WA 98052-6399, (425) 882-8080, (2001).

Mizuta, H., Tomonori, T., *The Physics and Applications of Resonant Tunnelling Diodes*, Cambridge University Press, New York, (1995).

Neamen, D.A., *Semiconductor Physics and Devices : Basic Principles*, Irwin, Homewood, IL, (1992).

Oguma, Y., Sashinaka, N., Asada, M., “Terahertz Response with Gradual Change from Square-Law Detection to Photon-Assisted Tunneling in Triple-Barrier Resonant Tunneling Diodes”, *Japanese Journal of Applied Physics*, **38**, L717-L719, (1999).

Papp, G., Di Ventra, M., Coluzza, C., Balderschi, Al, Margaritondo, G., Current Rectification Through a Single-Barrier Resonant Tunneling Quantum Structure,” *Superlattices and Microstructures*, **17**, 273, (1995).

Penley, J.C., “Tunneling Through Thin Films with Traps”, *Physical Review*, **128**, 596, (1962).

Pierret, R. F., *Advanced Semiconductor Fundamentals*, Addison-Wesley, Massachusetts, (1989).

Pollack, S.R., Morris, C.E., “Electron Tunneling Through Asymmetric Films of Thermally Grown Al_2O_3”, *Journal of Applied Physics*, **35**, 1503, (1964).

Press, W.H., Teukolsky, S.A., Vetterling, W.T., Flannery, B.P., *Numerical Recipes in C*, Cambridge University Press, New York, (1982).

Ramo, S., Whinnery, J.R., Van Duzer, T., *Fields and Waves in Communication Electronics*, Wiley, New York, (1994).

R.D. Mathis, P.O. Box 92916, Long Beach, CA 90809-2916 (562) 426-7049, (2001).

Rieke, G.H., *Detection of Light*, Cambridge University Press, New York (1996).

Saleh, B.E.A, Teich, M.C., *Fundamentals of Photonics*, Wiley, New York, (1991).

Sanchez, A., Davis, Jr., C.F., Liu, K.C., Javan, A., “The MOM Tunneling Diode: Theoretical Estimate of its Performance at Microwave and Infrared Frequencies”, Journal of Applied Physics, **49**, 10, (1978).

Sashinaka, N., Oguma, Y., Asada, M., “Observation of THz Photon-Assisted Tunneling in Triple-Barrier Resonant Tunneling Diodes Integrated With Patch Antenna”, *Japanese Journal of Applied Physics*, **39**, 4899-4903, (2000).

Scherer, H., Weimann, Th., Hinze, P., Samwer, B.W., Zorin, A.B., Niemeyer, J., “Characterization of all Chromium Tunnel Junctions and Single-Electron Tunneling Devices Fabricated by Direct-Writing Multilayer Technique”, *Journal of Applied Physics*, **12**, 6956, (1999).

Schmidlin, F.W., “Enhanced Tunneling Through Dielectric Films Due to Ionic Defects”, *Journal of Applied Physics*, **37**, 2823, (1966).

Schroder, D.K., *Semiconductor Material and Device Characterization,* 2nd edition, John Wiley and Sons, New York, (1998).

Schiff, L.I., *Quantum Mechanics*, 3rd edition, McGraw-Hill, New York, (1968).

Shibata, T., Zhu, Y.C., “The Effect of Temperature on the Growth of Anodic Oxide Film on Titanium”, *Corrosion Science*, **37**, 133, (1995).

Simmons, J.G., “An Analytical Form of Ku and Ullmans Equations”, *Applied Physics Letters*, **6**, 54, (1963).

Simmons, J.G., “Electric Tunnel Effect between Dissimilar Electrodes Separated by a Thin Insulating Film”, *Journal of Applied Physics*, **34**, 2581, (1963).

Simmons, J.G., “Incorporation of Electric-Field Penetration of the Electrodes in the Theory of Electron Tunnelling Through a Dielectric Layer”, *British Journal of Applied Physics*, **18**, 269, (1967).

Simpson, H.J., “Two Cars In Every Garage and Three Eyes on Every Fish.”, Twentieth Century Fox Home Entertainment, Beverly Hills, (1997).

Snow, E.S., Park, D., Campbell, P.M., “Single-atom Point Contact Devices Fabricated with an Atomic Force Microscope”, *Applied Physics Letters*, **69**, 269, (1996).
Snow, E.S., Campbell, P.M., Rendell, R.W., Buot, F.A., Park, D., Marrian, R.K., Magno, R., “A Metal/Oxide Tunneling Transistor”, *Applied Physics Letters*, **72**, 3071, (1998).

Sordan, N., “Quantum Constriction Rectifier”, *Phys. Rev. B.*, **54**, 10332, (1996).

Stanford Research Systems, 1290-D Reamwood Ave., Sunnyvale, CA 94089, (408) 744-9040, (2001).

Suemasu, T., Wantanabe, M., Suzuki, J., Kohno, Y., Asada, M., Suzuki, N., “Metal ($CoSi_2$)/Insulator (CaF_2) Resonant Tunnelling Diode”, *Japanese Journal of Applied Physics*, **33**, 57, (1994).

Sze, S.M., *Physics of Semiconductor Devices*, 2nd edition, John Wiley and Sons, New York, (1981).

Tien, P.K., Gordon, J.P., “Multiphoton Process Observed in the Interaction of Microwave Fields with the Tunneling between Superconductor Films”, *Physical Review*, **129**, 647, (1963).

Tucker, J.R., Millea, M.F., “Quantum Detection at Millimeter Wavelengths”, *Reviews of Modern Physics*, **57**, 1055, (1985).

Tompkins, H.G., *A Users Guide to Ellipsometry*, Academic Press, Boston, (1993).

Torrey, H.C., Whitmer, C.A., *Crystal Rectifiers*, Boston Technical Publishers, Inc., Lexington, (1964).

Van Duzer, T., *Principles of Superconductive Devices and Circuits*, Prentice Hall, Upper Saddle River, N.J., (1999).

Vogel, E.M., Suehle, J.S., Edelstein, M.D., Wang, B., Chen, Y., Bernstein, J.B., “Reliability of Ultrathin Silicon Dioxide Under Combined Substrate Hot-Electron and Constant Voltage Tunneling Stress”, **47**, 1183, (2000).

Wefers, K., Misra, C., *Oxides and Hydroxides of Aluminum,* Aluminum Company of America (ALCOA), (1987).

Watanabe, M., Iketani, Y., Asada, M., "Epitaxial Growth and Electrical Characteristics of CaF_2/Si/CaF_2 Resonant Tunneling Diode Structures Grown on Si (111) 1° –off Substrate", *Japanese Journal of Applied Physics*, **39**, L964-L967, (2000).

Waters, R.L., *Tunneling Through SiO_2 Thermally Grown on SiC and Si Substrates*, University of Colorado, Boulder, C.O., (1999).

Weinberg, Z.A., Hartstein, A., "On the Nature of the Image Force in Quantum Mechanics with Application to Photon Assisted Tunneling and Photoemission", *Journal of Physics C : Solid State Physics,* **11**, L469, (1978).

Wengler, M.J., "Submillimeter-Wave Detection with Superconducting Tunnel Diodes", *Proceedings of the IEEE,* **80**, 1810, (1992).

Wolfram Rearch, Inc., 100 Trade Center Drive, Champaign, IL 61820-7237, (217) 398-0700, (2001)

Wummer, J., Gustafson, T.K., Thanyavarin, S., "High Speed M-B-M and M-I-S-I-M Detectors for Integrated Optics", *SPIE Proceedings of the 27th International Symposium and Instrument Display*, San Diego, CA, 185, (1983).

Young, D.J., Cohen, M., "Oxidation Behavior of Chromium Between 300 and 600 ˚C", *Journal of the Electrochemical Society,* **124**, 769, (1977).

Zhao, J., Wang, A., Campbell, P., Green, M.A., "A 19.8% Efficient Honeycomb Multicrystalline Solar Cell with Improved Light Trapping", *IEEE Transactions on Electron Devices*, **46**, 1978, (1999).

APPENDIX I – PHYSICAL CONSTANTS

Description	**Symbol**	**Value**	**Unit**
Electron charge	q	$1.60217733 \times 10^{-19}$	C
Speed of Light	co	2.99792458×10^{8}	m/s
Boltzmann Constant	kb	8.617385×10^{-5}	eV
Permittivity of Vacuum	ε_o	$8.854187817 \times 10^{-12}$	F/m
Permeability of Vacuum	μ_o	$4\pi \times 10^{-7}$	N/A^{2}
Planck Constant	h	$6.6260755 \times 10^{-34}$	J•s
Planck Constant by 2π	$\hbar$	$1.05457266 \times 10^{-34}$	J•s
Free electron mass	m_o	$9.1093897 \times 10^{-31}$	kg

(Cohen, 1997)

APPENDIX II – MATERIAL PARAMETERS

Metal	Workfunction (eV)	Oxide Affinity (eV)
Pt	5.65	
Ni	5.15	
Pd	5.12	
Au	5.1	
Mo	4.6	
W	4.55	
Hg	4.52	
Cr	4.5	3.76
Cu	4.4	
Bi	4.4	
Sn	4.38	
Ti	4.33	
Fe	4.31	
Al	4.28	1.78 *(2.7 nat)*
Ag	4.26	
Zn	4.24	
Cd	4.1	
Sb	4.08	
Pb	4	
Nb	3.99	3.89
Ga	3.96	
Be	3.92	
Mn	3.83	
In	3.8	
Tl	3.7	
Mg	3.64	
Ca	2.8	
Ba	2.49	
Li	2.38	
Na	2.35	
Sr	2.35	
K	2.22	
Rb	2.16	
Cs	1.81	

Metals (Neamen, 1992) and (Ashcroft, 1976)
Nb/NbO_x (Snow, 1998)
Al/Al_2O_3 (Pollack, 1964)
Cr/Cr_2O_3 (Scherer, 1999)

APPENDIX III – DIODE FABRICATION TABLE

#	Sub.	Pad	Base	Oxide	Top	Area	Oxidation
1	slide	-	Ti	TiOx -Anodic	Cr	0.02	4V
2	flat	-	Ti	TiOx - Anodic	Cr	0.02	4V
3	slide	-	Ti	TiOx - Anodic	Cr	0.02	4V
4	slide	-	Ti	TiOx - Anodic	Cr	0.02	4V
5	slide	-	Y	SiO -Evaporated	Cr	0.002	2nm
6	slide	-	Ti	SiO - Evaporated	Cr	0.02	2nm
7	slide	-	Ti	SiO - Evaporated	Cr	0.002	2,6nm
8	slide	-	Ti	TiOx - Anodic	Cr	0.002	2V
9	slide	-	Ti	SiO - Evaporated	Cr	0.002	3nm
10	slide	-	Cr	Al2O3 - ALD	Cr	0.02	2nm
11	slide	-	Cr	Al2O3 - ALD	Cr	2.50E-04	1nm
12A	flat	-	Cr	Al2O3 - ALD	Al	2.50E-04	2nm
12B	flat	-	Cr	Al2O3 - ALD	Al	2.50E-04	3nm
12C	flat	-	Cr	Al2O3 - ALD	Al	2.50E-04	4nm
12D	flat	-	Cr	Al2O3 - ALD	Al	1 to 5E-4	10nm
13A	flat	-	Ag	Al2O3 - ALD	-	2.50E-04	2nm
13B	flat	-	Ag	Al2O3 - ALD	-	2.50E-04	3nm
13C	flat	-	Ag	Al2O3 - ALD	-	2.50E-04	4nm
13D	flat	-	Ag	Al2O3 - ALD	-	1 to 5E-4	10nm
14	flat	Ag	Cr	Al2O3 - ALD	Cr		10nm: 450K
15	flat	Ag	Cr	Al2O3 - ALD	Cr		450K, 750K
16	flat	Ag	Cr	Al2O3 - ALD	Cr		640K
17	flat	Au	Al	Al2O3 - thermal	Al		180C, 40days
18	flat	Au	Al	Al2O3 - thermal	Al		180C, 54days
19	flat	Au	Al	Al2O3 - thermal	Ag		180C, 40days
20	flat	Au	Al	Al2O3 - thermal	Ag		180C, 54days
21	flat	Ag	Al	Al2O3 - ALD	Al		10nm: 600K
22	flat	Ag	Al	Al2O3 - ALD	Al		450K, 600K
23	flat	Ag	Al	Al2O3 - ALD	Al		450K, 700K
24	flat	Ag	Al	Al2O3 -ALD	Al		450K, 1000K
25	flat	Ag	Al	Al2O3 - thermal	Ag		450C, 20min
26	flat	Ag	Al	Al2O3 - thermal	Ag		450C, 54min
27	flat	Ag	Al	Al2O3 - thermal	Al		500C, 60min

28	flat	Ag	Al	Al2O3 - thermal	Ag		
29	flat	Ag	Al	Al2O3 - thermal	-		500C, 2hr
30	flat	Ag	Al	Al2O3 - thermal	-		
31	flat	Ag	Al	Al2O3 - thermal	-		
32	flat	Ag	Al	Al2O3 - thermal	Ag		400C, 2hr
33	flat	Ag	Al	Al2O3 - thermal	Ag		450C, 2.5hr
34	flat	Ag	Ti	Al2O3 - thermal	Al		450C, 2hr
35	flat	Ag	Ti	Al2O3 - thermal	-		
36	flat	Ag	Ti	Al2O3 - thermal	-		500C, 2hr
37	flat	Ag	Ti	Al2O3 - thermal	-		450C, 2hr
38	flat	Ag	Ti	Al2O3 - thermal	-		450C, 2hr
39	flat	Ag	Ti	Al2O3 - thermal	-		450C, 2hr
40	flat	Ag	Ti	Al2O3 - thermal	-		
41	flat	Ag	Ti	Al2O3 - thermal	-		
42	Si	Ag	Al	Al2O3 - thermal	-		
43	Si	Ag	Al	Al2O3 - thermal	-		450C, 2hr
44	Si	Ag	Al	Al2O3 - thermal	-		
45	Si	Ag	Al	Al2O3 - thermal	-		
46	Si	Ag	Al	Al2O3 - thermal	-		400C, 2hr
47	Si	Ag	Al	Al2O3 - thermal	-		
48	Si	-	Al	Al2O3 - thermal	-		
49	Si	-	Al	Al2O3 - ambient	Ag		ambient, 7days
50	Si	-	Al	Al2O3 - ambient	-		
51	Si	-	Al	Al2O3 - thermal	-		225C, ambient
52	Si	Ag	Al	Al2O3 - GPO	Ag		
53	Si	-	Al	Al2O3 - GPO	-		
54	Si	-	Al	Al2O3 - GPO	Al		
55	Si	-	Al	Al2O3 - GPO	Ag		16.5hr
56	Si	-	Al	Al2O3 - GPO	Ag		16.5hr
57	Si	-	Al	Al2O3 - GPO	Ag		2hr
58	Si	-	Al	Al2O3 - GPO	Ag		3hr
59	Si	-	Al	Al2O3 - GPO	Ag		24hr
60	Si	-	Al	Al2O3 - GPO	-		2hr
61	Si	Ag	Al	Al2O3 - GPO	Ag		2hr, VA=30
62	Si	Ag	Al	Al2O3 - GPO	Ag		2hr, VA=60
63	Si	Ag	Al	Al2O3 - GPO	Ag		2hr, VA=80
64	Si	Ag	Al	Al2O3 - GPO	Ag		2hr, VA=100
65	Si	Ag	Al	Al2O3 - ambient	Ag		
66	Si	Ag	Al	Al2O3 - GPO	Ag	0.0014	2hr, VA=30
67	Si	Ag	Al	Al2O3 - GPO	Ag	0.006	2hr, VA=50

68	Si	Ag	Al	Al2O3 - GPO	Ag		1.75hr, VA=30
69	Si	Ag	Al	Al2O3 - GPO	Ag		2hr, VA=40
70	Si	Ag	Al	Al2O3 - GPO	Ag		2hr, VA=40
71	Si	Ag	Ni	Al2O3 - GPO	Ag		2hr, VA=50
72	Si	Ag	Al	Al2O3 - GPO	Ag	0.001	2hr, VA=50
73	Si	Ag	Al	Al2O3 - GPO	Ag	2.28E-05	2hr, VA=50
74	Si	Ag	Al	Al2O3 - GPO	Au	2.49E-05	2hr, VA=50
75	Si	Ag	Cr	Cr2O3 - GPO	Au	1.67E-05	24hr
76	Si	Ag	Cr	Cr2O3 - GPO	Ag	1.62E-06	24hr
77	Si	Ag	Cr	Cr2O3 - GPO	Ag		24hr
78	Si	Ag	Cr	Cr2O3 - ambient	Ag		24hr
79	Si	Au	Al	Al2O3 - GPO	Au		2hr
80	Si						
81	Si	-	Al	Al2O3 - GPO	Ag		
82	Si	Ag	Cr	Cr2O3 - ambient	Pt		
83	Si	-	Nb	NbOx - ambient	Ag		
84	Si	-	Nb	NbOx - ambient	Ag		
85	Si	-	Al	Al2O3 - GPO	Au		
86	Si	-	Al	Al2O3 - GPO	Au		
87	Si	-	Nb	NbOx - ambient	Ag		
88	Si	-	Nb	NbOx - ambient	Ag		
89	Si	-	Nb	NbOx - ambient	Ag		
90	Si	Ag	Al	Al2O3 - ambient	Ni	1-400E-8	
91	Si	Ag	Cr	Cr2O3 - ambient	Pt	1-400E-8	
92	Si	Ag	Nb	NbOx - ambient	Ag	1-400E-8	
93	Si	Ag	Nb	NbOx - ambient	Ag	1-400E-8	
94	Si	-	Al	Al2O3 - GPO	Al		
95	Si	Ag	Al	Al2O3 - GPO	Ni		
96	Si	Ag	Ni	NiOx - GPO	Ag		
97	Si	-	Nb	NbOx - ambient	Ag	1-400E-8	
98	Si	-	Nb	NbOx - ambient	Ag	1-400E-8	
99	Si	-	Nb	NbOx - ambient	Ag	1-400E-8	
100	Si	Ag	Cr	Cr2O3 - ambient	Pt	1-400E-8	
101	Si	Ag	Cr	-	-	1-400E-8	
102	Si	Ag	Cr	Cr2O3 - ambient	Pt	1-400E-8	
103	Si	Ag	Cr	Cr2O3 - ambient	Ag	1-400E-8	
104	Si	Ag	Cr	Cr2O3 - ambient	Pt	1-400E-8	

105	Si	Ag	Al	Al2O3 - ambient	Ni		3.5hr, VA=40
106	Si	Ag	Al		Ag		
107	Si	Ag	Ni	NiOx - ambient	Ag	1-400E-8	
108	Si	Ag	Nb	NbOx - ambient	Ag	1-400E-8	
109	Si	Ag	Nb	NbOx - ambient	Ag	1-400E-8	
110	Si	Ag	Nb	NbOx - ambient	Ag	1-400E-8	
111	Si	Ag	Nb	NbOx - ambient	Ag	1-400E-8	
112	Si	Ag	Ag	Al2O3 - GPO	Ag		3nm Al
113	Si	Ag	Ag	Al2O3 - GPO	Ag		10nm Al
114	Si	Ag	Ag	Al2O3 - GPO	Ag		100nm Al
Cr	Si	-	Cr	Cr2O3 - ambient	Pt		
Cr	Si	-	Cr	Cr2O3 - ambient	Pt		
115	Si	Ag	Cr	Cr2O3 - ambient	Pt	1-400E-8	
116	Si	Ag	Cr	Cr2O3 - ambient	Pt	1-400E-8	
117	Si	Ag	Cr	Cr2O3 - ambient	Pt	1-400E-8	
118	Si	Ag	Cr	Cr2O3 - ambient	Ag	1-400E-8	w/3.0nm ALD
119	Si	Ag	Cr	Cr2O3 - ambient	Ag	1-400E-8	
120	Si	Ag	Ag	Cr2O3 - ambient	Pt	1-400E-8	
121	Si	Ag	Cr	Cr2O3 - ambient	Ag	1-400E-8	w/2.0nm ALD
122	Si	Ag	Cr	Cr2O3 - ambient	Ag	1-400E-8	w/2.5nm ALD
123	Si	Ag	Cr	Cr2O3 - ambient	Ag	1-400E-8	
124	Si	Ag	Cr	Cr2O3 - ambient	Ag	1-400E-8	
125	Si	Ti/Ag	Cr	Cr2O3 - ambient	Ag	1-400E-8	w/3.0nm ALD
126	Si	Ti/Ag	Cr	Cr2O3 - ambient	Ag	1-400E-8	w/2.5nm ALD
127	Si	Ti/Ag	Cr	Cr2O3 - ambient	Ag	1-400E-8	w/3.5nm ALD
128	Si	Ti/Ag	Cr	Cr2O3 - ambient	Ag	1-400E-8	w/4.0nm ALD
129	Si	Ti/Ag	Cr	Cr2O3 - ambient	Ag	1-400E-8	
130	Si	Cr/Ag	Cr	Cr2O3 - ambient	-	1-400E-8	
131	Si	Cr/Ag	Cr	Cr2O3 - ambient	-	1-400E-8	
132	Si	Cr/Ag	Cr	Cr2O3 - ambient	-	1-400E-8	
133	Si	Cr/Ag	Cr	Cr2O3 - ambient	-	1-400E-8	
134	Si	Cr/Ag	Cr	Cr2O3 - ambient	-	1-400E-8	
135	Si	Cr/Ag	Cr	Cr2O3 - ambient	Mg/Ag	1-400E-8	
136	Si	Cr/Ag	Cr	Cr2O3 - ambient	Mg/Ag	1-400E-8	
137	Si	Cr/Ag	Cr	Cr2O3 - ambient	Mg/Ag	1-400E-8	
138	Si	Cr/Ag	Cr	Cr2O3 - ambient	Mg/Ag	1-400E-8	
139	Si	Cr/Au	Cr	Cr2O3 - ambient	-	1-400E-8	
140	Si	Cr/Au	Cr	Cr2O3 - ambient	Au	1-400E-8	

141	Si	Cr/Au	Cr	Cr2O3 - ambient	Cr/Au	1-400E-8	
142	Si	Cr/Au	Cr	Cr2O3 - ambient	Al	1-400E-8	w/3.0nm ALD
143	Si	Cr/Au	Cr	Cr2O3 - ambient	Al	1-400E-8	w/3.0nm ALD
144	Si	Cr/Au	Cr	Cr2O3 - ambient	Al	1-400E-8	
145	Si	Cr/Au	Cr	Cr2O3 - ambient	Cr/Au	1-400E-8	
146	Si	Cr/Au	Cr	Cr2O3 - ambient	Cr/Au	1-400E-8	w/3.0nm ALD
147	Si	Cr/Au	Cr	Cr2O3 - ambient	Al	1-400E-8	w/3.0nm ALD
148	Si	Cr/Au	Cr	Cr2O3 - ambient	Al	1-400E-8	
149	Si	Cr/Au	Cr	Cr2O3 - ambient	Mg/Au	1-400E-8	
150	Si	Cr/Au	Cr	Cr2O3 - ambient	-	1-400E-8	
151	Si	Cr/Au	Cr	Cr2O3 - ambient	Mg/Au	1-400E-8	w/3.0nm ALD
152	Si	Cr/Au	Cr	Cr2O3 - ambient	Mg/Au	1-400E-8	
151	Si	Cr/Au	Cr	Cr2O3 - ambient	Mg/Au	1-400E-8	w/3.0nm ALD
152	Si	Cr/Au	Cr	Cr2O3 - ambient	Mg/Au	1-400E-8	
itn	Si	Cr/Au	Cr	Cr2O3 - ambient	Ag	1-400E-8	
152	Si	Cr/Au	Cr	Cr2O3 - ambient	Al/Au	1-400E-8	
153	Si	Cr/Au	Cr	Cr2O3 - ambient	Cr/Au	1-400E-8	
154	Si	Cr/Au	Cr	Cr2O3 - ambient	Pd	1-400E-8	
155	Si	Cr/Au	Cr	Cr2O3 - ambient	Pd		
156	Si	Cr/Au	Cr	Cr2O3 - O2 flow	Au	1-400E-8	5nm/75nm
157	Si	Cr/Au	Cr	Cr2O3 - O2 flow	Au	1-400E-8	10nm/75nm
158	Si	Cr/Au	Cr	Cr2O3 - O2 flow	Cr	1-400E-8	75nm/75nm
159	Si	Cr/Au	Cr	-	-	-	-
160	Si	Cr/Au	-	-	-	-	-
161	Si	Cr/Au	Cr	Cr2O3 - O2 flow	Cr	1-400E-8	
162	Si	Cr/Au	Cr	Cr2O3 - O2 flow	Pd	1-400E-8	
163	Si	Cr/Au	Cr	Cr2O3 - O2 flow	Cr	1-400E-8	
164	Si	Cr/Au	Cr	Cr2O3 - O2 flow	Pd	1-400E-8	w/3.0nm ALD
165	Si	Cr/Au	Cr	Cr2O3 - O2 flow	Al	1-400E-8	
166	Si	Cr/Au	Cr	Cr2O3 - O2 flow	Pd	1-400E-8	
167	Si	Cr/Au	Cr	Cr2O3 - O2 flow	Pd	1-400E-8	
168	Si	Cr/Au	Cr	Cr2O3 - O2 flow	Cr	1-400E-8	Plasma
169	Si	Cr/Au	Cr	Cr2O3 - O2 flow	-	1-400E-8	~~Plasma~~
170	Si	Cr/Au	Cr	Cr2O3 - O2 flow	Al	1-400E-8	Plasma
171	Si	Cr/Au	Cr	Cr2O3 - O2 flow	-	1-400E-8	
172	Si	Cr/Au	Cr	Cr2O3 - O2 flow	Al	1-400E-8	~~Plasma~~
173	Si	Cr/Au	Cr	Cr2O3 - O2 flow	Cr	1-400E-8	~~Plasma~~
174	Si	Cr/Au	Cr	Cr2O3 - O2 flow	Cr	1-400E-8	240C, 1hr anneal

175	Si	Cr/Au	Cr	Cr2O3 - O2 flow	-	-	-
176	Si	Cr/Au	Cr	Cr2O3 - O2 flow	-	1-400E-8	Plasma
177	Si	Cr/Au	Cr	Cr2O3 - O2 flow	Ti	1-400E-8	Plasma
178	Si	Cr/Au	Cr	Cr2O3 - O2 flow	-	1-400E-8	Plasma
179	Si	Cr/Au	Cr	Cr2O3 - O2 flow	Mg	1-400E-8	Plasma
180	Si	Cr/Au	-	-	-		
181	Si	Cr/Au	-	-	-		
182	Si	Cr/Au	Cr	Cr2O3 – O2 flow	Pd	1-400E-8	*Design B*
183	Si	Cr/Au	Cr	Cr2O3 – O2 flow	Ag	1-400E-8	*Design B*
184	Si	Cr/Au	Cr	Cr2O3 - O2 flow	Pd	1-400E-8	w/3nm ALD
185	Si	Cr/Au	Cr	Cr2O3 - O2 flow	Pd	1-400E-8	w/3nm ALD
186	Si	Cr/Au	Cr	Cr2O3 - O2 flow	Pd	1-400E-8	w/3nm ALD
187	Si	Cr/Au	Cr	Cr2O3 - O2 flow	Pd	1-400E-8	w/3nm ALD
188	Si	Cr/Au	Cr	Cr2O3 - O2 flow	Pd	1-400E-8	w/3nm ALD
189	Si	-	-	-	-	-	-
190	Si	Cr/Au	Cr	Cr2O3 - O2 flow	Pd	1-400E-8	w/ALD
191	Si	Cr/Au	Cr	Cr2O3 - O2 flow	Pd	1-400E-8	w/ALD
192	Si	Cr/Au	Cr	Cr2O3 - O2 flow	Pd	1-400E-8	w/ALD
193	Si	Cr/Au	Cr	Cr2O3 - O2 flow	Pd	1-400E-8	*w/184-188*
194	Si	Cr/Au	Cr	Cr2O3 – O2 flow	Cr	1-400E-8	*Design B*
195	Si	Cr/Au	Cr	Cr2O3 – O2 flow	-	1-400E-8	*Design B*
196	Si	Cr/Au	Cr	Cr2O3 – O2 flow	-	1-400E-8	*Design B*
197	Si	Cr/Au	Cr	Cr2O3 – O2 flow	-	1-400E-8	*Design B*
198	Si	Cr/Au	Cr	Cr2O3 – O2 flow		1-400E-8	
199	Si	Cr/Au	Cr	Cr2O3 – O2 flow		1-400E-8	
200	Si	Cr/Au	Cr	Cr2O3 – O2 flow		1-400E-8	
201	Si	Cr/Au	Cr	Cr2O3 – O2 flow		1-400E-8	
202	Si	Cr/Au	Cr	Cr2O3 – O2 flow		1-400E-8	
203	Si	Cr/Au	Cr	Cr2O3 – O2 flow		1-400E-8	
204	Si	Cr/Au	Cr	Cr2O3 – O2 flow		1-400E-8	